APPLIED COMPUTATIONAL ELECTROMAGNETICS SOCIETY JOURNAL

June 2014
Vol. 29 No. 6
ISSN 1054-4887

The ACES Journal is abstracted in INSPEC, in Engineering Index, DTIC, Science Citation Index Expanded, the Research Alert, and to Current Contents/Engineering, Computing & Technology.

The illustrations on the front cover have been obtained from the research groups at the Department of Electrical Engineering, The University of Mississippi.

THE APPLIED COMPUTATIONAL ELECTROMAGNETICS SOCIETY
http://www.aces-society.org

EDITOR-IN-CHIEF

Atef Elsherbeni
Colorado School of Mines, EECS Dept.
Golden, CO 80401, USA

ASSOCIATE EDITORS-IN-CHIEF

Sami Barmada
University of Pisa. EE Dept.
Pisa, Italy, 56126

Yasushi Kanai
Niigata Inst. of Technology
Kashiwazaki, Japan

Ozlem Kilic
Catholic University of America
Washington DC, 20064, USA

Fan Yang
Tsinghua University, EE Dept.
Beijing 100084, China

Mohammed Hadi
Kuwait University, EE Dept.
Safat, Kuwait

Alistair Duffy
De Montfort University
Leicester, UK

Mohamed Bakr
McMaster University, ECE Dept.
Hamilton, ON, L8S 4K1, Canada

Abdul Arkadan
Rafik Hariri University
Chouf 2010, Lebanon

Paolo Mezzanotte
University of Perugia
I-06125 Perugia, Italy

Antonio Musolino
University of Pisa
56126 Pisa, Italy

Marco Arjona López
La Laguna Institute of Technology
Coahuila 27266, Mexico

EDITORIAL ASSISTANTS

Matthew J. Inman
University of Mississippi, EE Dept.
University, MS 38677, USA

Shanell Lopez
Colorado School of Mines, EECS Dept.
Golden, CO 80401, USA

EMERITUS EDITORS-IN-CHIEF

Duncan C. Baker
EE Dept. U. of Pretoria
0002 Pretoria, South Africa

Robert M. Bevensee
Box 812
Alamo, CA 94507-0516, USA

Allen Glisson
University of Mississippi, EE Dept.
University, MS 38677, USA

Ahmed Kishk
University of Mississippi, EE Dept.
University, MS 38677, USA

David E. Stein
USAF Scientific Advisory Board
Washington, DC 20330, USA

EMERITUS ASSOCIATE EDITORS-IN-CHIEF

Mohamed Abouzahra
MIT Lincoln Laboratory
Lexington, MA, USA

Levent Gurel
Bilkent University
Ankara, Turkey

Erdem Topsakal
Mississippi State University, EE Dept.
Mississippi State, MS 39762, USA

Alexander Yakovlev
University of Mississippi, EE Dept.
University, MS 38677, USA

EMERITUS EDITORIAL ASSISTANTS

JUNE 2014 REVIEWERS

THE APPLIED COMPUTATIONAL ELECTROMAGNETICS SOCIETY

JOURNAL

Vol. 29 No. 6 June 2014

TABLE OF CONTENTS

Lowpass Filter Design Based on Microstrip Meander Line with HDGS

Ayman S. Al-Zayed [1], Mekdad B. Asad Allah [2], and Samir F. Mahmoud [3]

[1] Electrical Engineering Department
Kuwait University, P.O. Box 5969, Al-Safat 13060, Kuwait
ayman.alzayed@ku.edu.kw

[2] Electrical Maintenance Division
Kuwait National Petroleum Company, P.O. Box 9202, Mina Al-Ahmadi 61003, Kuwait
m.asadallah@knpc.com

[3] Electrical Engineering Department
Kuwait University, P.O. Box 5969, Al-Safat 13060, Kuwait
And Professor Emeritus at Cairo University, Egypt
samirfm2000@yahoo.com

Abstract – A microstrip meander line with a single H-shaped Defected Ground Structure (HDGS) is employed to design a novel compact lowpass filter with sharp roll off and wide stop band. Two parametric studies were conducted to analyze the sensitivity of the HDGS position and the size effects on the filter response. The design is fabricated to have a 6 GHz cutoff frequency using Rogers TMM 10i substrate, with an area of 7.6 x 6 mm^2. The measured results are in a good agreement with simulation prediction.

Index Terms – Defected ground structures, compact filter, lowpass filter and microstrip meander line.

I. INTRODUCTION

Lowpass filters are widely used in various wireless communication systems; they take important roles in many microwave integrated circuits and monolithic microwave integrated circuits. Lowpass filters with compact design, superior performance and low cost are highly desired to incorporate in innovative microwave systems. There have been several variations to the state-of-art microstrip line structure, such as meandering the transmission line [1-7], defecting the ground plane structure [8-28]; to enhance the behavior of the lowpass filter.

Defecting the ground plane structure of a microstrip line has been popular for more than a decade. A defect etched in the ground plane rejects certain frequency bands by suppressing the surface wave based on its geometry and position. There have been many geometrical Defected Ground Structures (DGS), such as dumbbell [12-15], circular [16], elliptical [17-18], Complementary Slot Ring Resonator (CSRR) [5, 19-21], U-shaped [22-23], H-shaped [24-25]; where each shape has its merits. In designing lowpass filters using DGS shapes, two or more DGS's are used in order to attain good frequency response, such as low insertion loss, sharp cutoff transition and wide stop band.

In this paper, instead of using a straight microstrip line with multiple DGS, a meander microstrip line is used with a single H-shaped Defected Ground Structure (HDGS), to design a compact lowpass filter with a superior performance. The proposed meander line filter

Submitted On: November 19, 2013
Accepted On: July 14, 2014

with a single DGS is compact and is characterized by very low insertion loss in the passband, a steep roll-off transition and a wide stopband. A parametric study of the effects of size and position sensitivity of the HDGS are investigated. The filter is measured and compared with simulation results.

II. CONFIGURATION AND CHARACTERISTICS OF THE LOWPASS FILTER

The proposed lowpass filter is depicted in Fig. 1, where a meandered 50-Ω line is printed on top of the dielectric layer surface and an HDGS etched in the ground plane. It is to be noted that in this design, the center of the HDGS is positioned exactly beneath the center of the meander line (L/2, W/2). The meander line parameters are illustrated in Fig. 1 (a), which are the meander spacing (l_1 and l_2), the meander line length (L) and the meander line width (D). The HDGS parameters are illustrated in the inset of Fig. 1 (b), which are the slot width (a), the slot gap (g) and the side lengths (b_1 and b_2). These parameters have prime influence on the performance of the filter. Therefore, the meander line and the H-defect parameters must be carefully chosen in order to achieve the satisfactory filter performance.

Using Agilent Advanced Design System (ADS) software, the proposed lowpass filter is simulated and results are plotted in Fig. 2. The lowpass filter is designed to operate at a cutoff frequency 6 GHz. It is worth mentioning that the area of the HDGS plays a dominant role in determining the cutoff frequency of the filter. The pass band ripples are less than 0.5 dB; the flatness in the pass band is affected by the dimensions of the slot width (a) and the slot gap (g). The meander line inhabits slow wave effect causing a wide stop band with high attenuation level [1, 7]. The stop band of the simulated S_{21} response maintains its attenuation level below -20 dB from 6.5 GHz to 10.7 GHz and below -10 dB from 6.25 GHz to 22.1 GHz, demonstrating a wide stop band as well as high rejection level, which reaches -68 dB at 10 GHz.

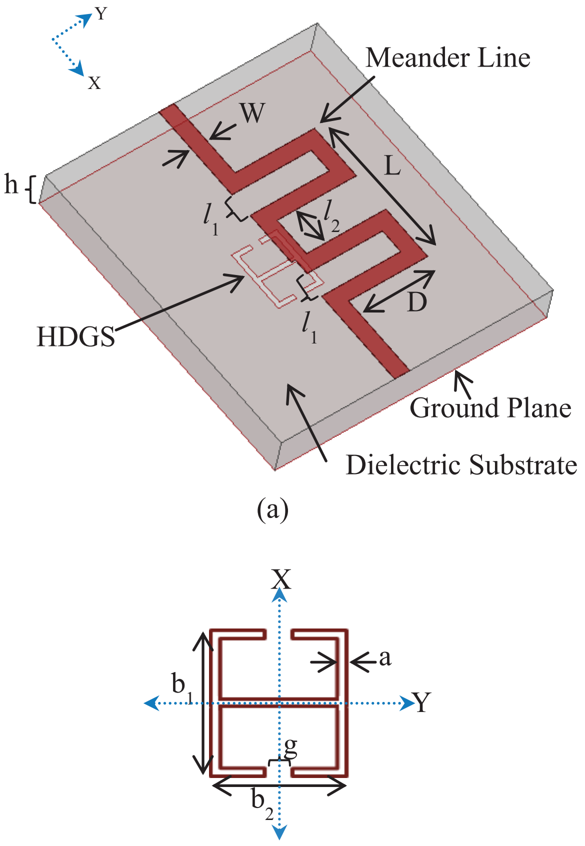

(a)

(b)

Fig. 1. Geometry of the proposed lowpass filter: (a) meander line and (b) HDGS.

The substrate is designed using Rogers TMM 10i™ with dielectric constant ε_r=9.8 and thickness h=0.508 mm. The conductor strip has 50 Ω characteristic impedance given by the width W=0.5 mm. Intensive simulations were conducted to optimize the filter parameters to achieve a superior lowpass filter response in terms of flat pass band, sharp roll-off transition and wide stop band with high attenuation level. The geometric dimensions of the meander line as well as the dimensions of the H-shaped ground defect are tabulated in Table 1. These dimensions bring the filter length to 0.39 of the effective electrical wavelength at the cutoff frequency, which denotes the compactness of the proposed lowpass filter size.

Table 1: The design parameters of the proposed lowpass filter in millimeter

L	l_1	l_2	D	a	b_1	b_2	g
7.6	1.55	2.5	5.5	0.3	4	3	0.6

In the design procedure of the proposed filter, dimensions of the HDGS are first obtained to set the cutoff frequency at 6 GHz. The meander spacing (l_1 and l_2) and the meander line width (D) are then optimized to reach a superior lowpass filter performance.

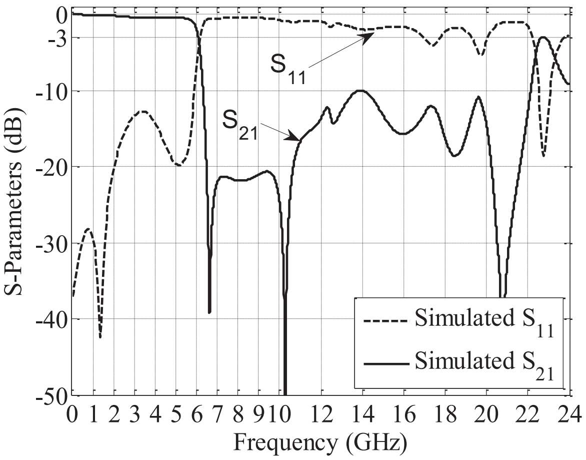

Fig. 2. The response of the proposed lowpass filter; S_{21} (solid line) and S_{11} (dashed line).

Figure 3 illustrates the performance of the meander line LPF, compared with the straight line based filter with one DGS. It is to be observed that the proposed meander line performs better in all aspects with a flat pass band, a steep transition region, a wide stop band and a high attenuation level in the stop band. The superiority of the performance of the proposed filter justifies the replacement of the straight line by meander line. It is worth noting that the straight line design can have better filter response if the number of DGS's are increased to two or more [19-22, 25], but this would be at the expense of more filter size.

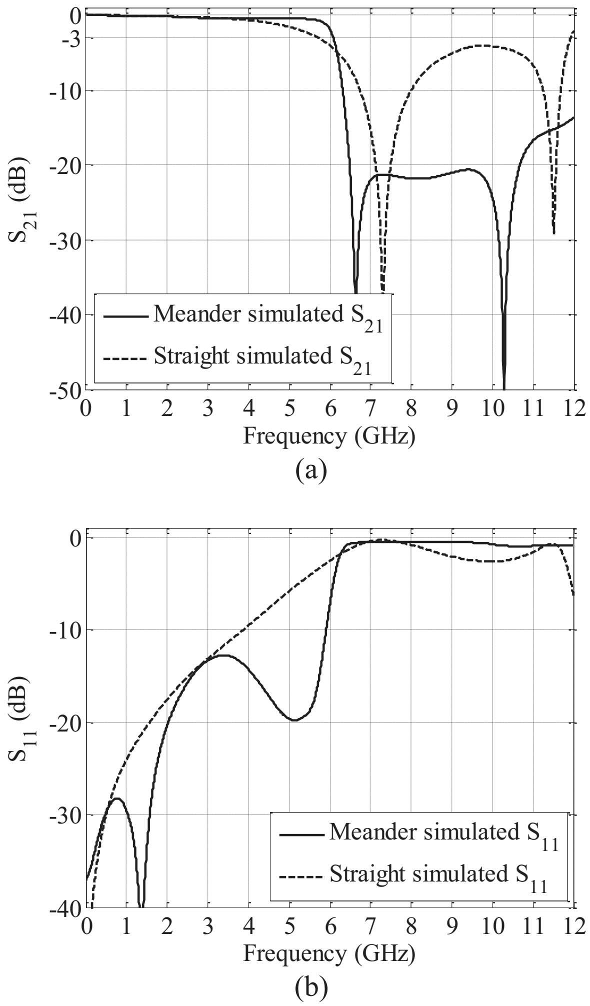

(a)

(b)

Fig. 3. S-parameters simulation comparison between the proposed lowpass filter (solid line) and the straight line design (dashed line): (a) S_{21} and (b) S_{11}.

III. PARAMETERIC STUDY

The performance of the presented lowpass filter underwent two parametric studies. First an investigation is carried out to learn more about how sensitive the positioning of the H-defect in the ground plane relative to the meander structure. This will give a measure of how tolerant the filter design to any miss-alignment in the positioning of the HDGS during fabrication. A second study is conducted to understand the result of having a different-sized HDGS on the filter response.

A. Sensitivity study

To verify the role of positioning the HDGS relative to the meander line, this test is performed. The study is based on shifting the HDGS position relative to the meander line, in other words keeping all parameters fixed except the position of the HDGS relative to the meander line. The study results are then compared to the original design. This study consists of six tests, where in each test the HDGS is displaced from the original design position, where the center of the HDGS is positioned exactly beneath the center of the meander line (L/2, W/2) by a specified amount in a specified direction.

Six tests have been carried out by shifting the HDGS 0.5 mm in the +x-direction, 0.5 mm in the ±y-direction, 1.0 mm in the +x-direction and 1.0 mm in the ±y-direction. The simulated S_{21} of each test is compared with the original proposed design as shown in Fig. 4. It is observed that the attenuation level and the width of the stop band are affected by the position of the HDGS relative to the meander line structure. Also, the cutoff frequency of the filter is shifted to higher values compared to the proposed operating cutoff frequency.

In case of any miss-alignment in fabrication, it can be argued that the filter performance is satisfactory with shift up to 1.0 mm in the +y-direction (33.3% of b_2), 0.5 mm in the –y-direction (16.7% of b_2), and 0.5 mm in the + or – x-direction (12.5% of b_1).

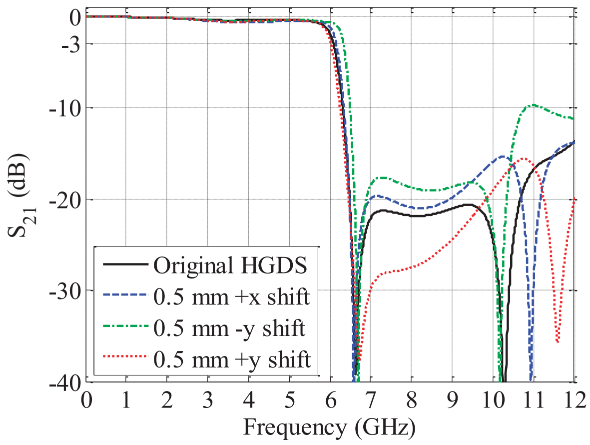

(a)

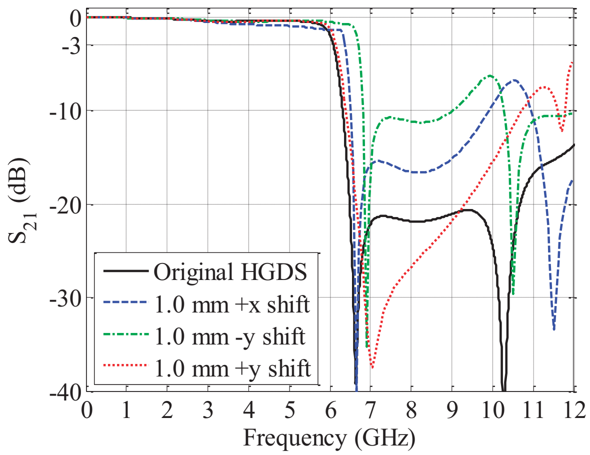

(b)

Fig. 4. Comparison of simulated S_{21} between the original proposed low-pass filter design (solid line) and spatial sensitivity test cases: (a) 0.5-mm displacements in HGDS designs and (b) 1.0-mm displacements in HGDS designs.

B. Scaling study

To underline the significance of the size of the HDGS etched in the ground plane, a scaling study is carried out. The study is based on re-simulating the proposed design, keeping all parameters fixed except for the size of the HDGS. This study consists of four tests, where in each test the HDGS is scaled by a specified factor. These four tests are scaling the H-shaped defect by 0.8, 0.9, 1.1 and 1.2. All simulation responses are compared to the original proposed design.

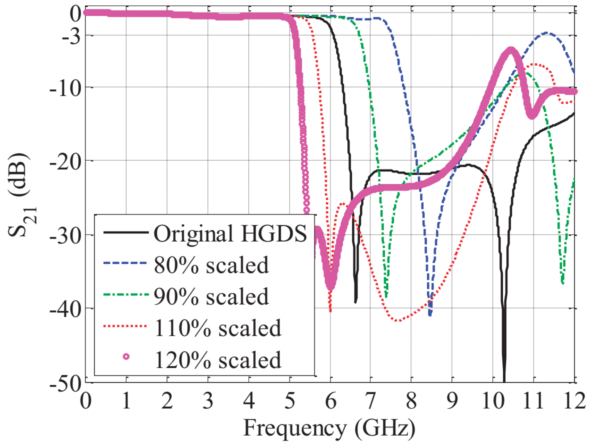

Fig. 5. The S_{21} simulations of the original proposed design (solid line) and all 4 cases of the scaling study.

Figure 5 shows the result of the study, where it is deduced that the cutoff frequency of the lowpass filter is affected by the size of the HDGS. It is realized that the larger the HDGS is, the lower the cutoff frequency is and vice versa. It is important to mention that the conducted tests did not include optimizing of the filter parameters for each case; it was merely scaling of the HDGS.

IV. EXPERIMENTAL RESULTS

The lowpass filter presented in this paper is fabricated, where the meander line structure is implemented on a Rogers TMM 10i substrate with dielectric constant ε_r=9.8 and thickness h=0.508 mm. These are the same design parameters used in all of the simulations in this paper. Figure 6 (a) and (b) illustrate photographs of the top layer and the HDGS layer of the fabricated filter, respectively. The miniature size of the meander structure is evident as well as the HDGS size.

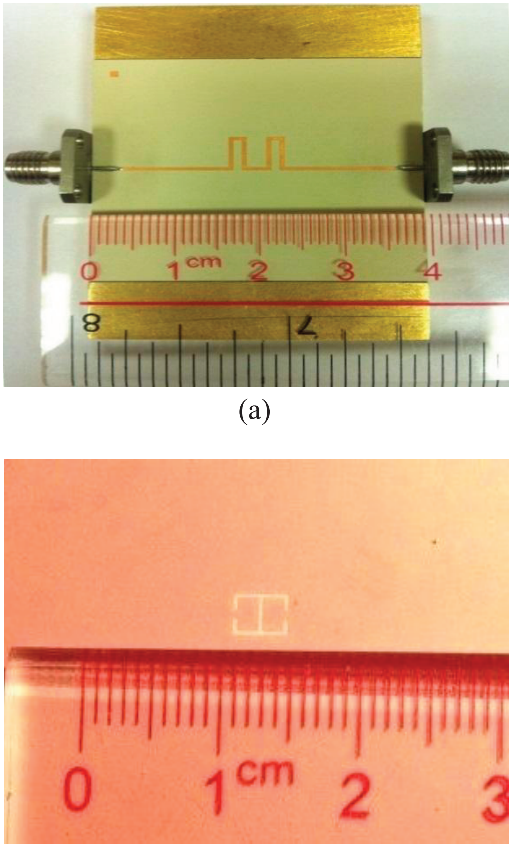

(a)

(b)

Fig. 6. Photographs of the measured low-pass filter: (a) the top layer and (b) the HDGS layer.

The manufactured lowpass filter response was measured by a vector network analyzer and results of the measurements are compared with the simulation predictions as shown in Fig. 7. These measurements show a good agreement with simulation results.

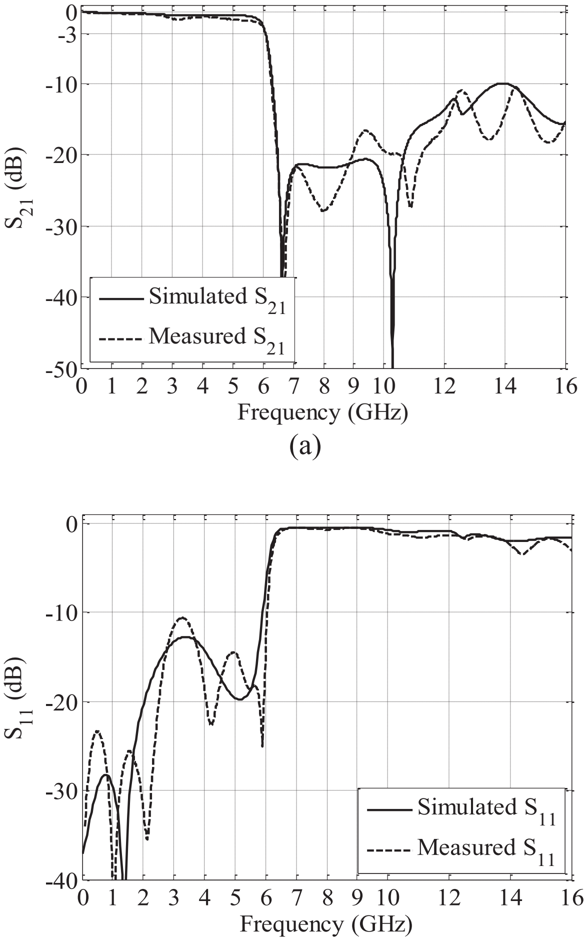

(a)

(b)

Fig. 7. S-parameters comparison between the simulated design (solid line) and the fabricated filter (dashed line): (a) S_{21} and (b) S_{11}.

V. CONCLUSION

In this paper, we present a compact superior lowpass filter comprising a meander line structure on top of a 0.508-mm Rogers TMM 10i substrate and a single H-shaped defect etched in the ground plane. The effect of the proposed meander line is compared with the straight line design. The comparison proves the superiority of the proposed design in terms of the filter criteria, such as a flat response in the pass band, a steep roll-off in the transition region and a wide stop band with high attenuation level staying below -10 dB from 6.25 GHz to 22.1 GHz. The operating cutoff frequency of the lowpass filter at 6 GHz is affected by the position and size of the HDGS. Two parametric studies were administered to investigate the effects of the position sensitivity of the HDGS relative to the meander line, as well as the size of the HDGS. The position sensitivity study shows that the proposed design can tolerate miss-alignment of the HDGS position up to 1.0 mm in the +y-direction (33.3% of b_2), 0.5 mm in the –y-direction (16.7% of b_2) and 0.5 mm in the + or – x-direction (12.5% of b_1). The scaling study presented the general relationship between the size of the HDGS and the filter cutoff frequency as inversely proportional. Scaling of the HDGS also affects the stop band response, and hence, further optimization is required to obtain satisfactory results. The presented lowpass filter design is simulated, fabricated and measured, where measurements show a good agreement with simulation results.

REFERENCES

[1] C. K. Wu, H. S. Wu, and C. K. C. Tzuang, "Electric-magnetic-electric slow-wave microstrip line and bandpass filter of compressed size," *IEEE Microwave Theory and Techniques*, vol. 50, no. 8, 1996-2004, August 2002.

[2] P. Vincent, J. Culver, and S. Eason, "Meandered line microstrip filter with suppression of harmonic passband response," *Microwave Symposium Digest, IEEE MTT-S International*, vol. 3, 1905-1908, 2003.

[3] G. Y. Su, C. N. Chan, U. L. Tam, and K. W. Tam, "Compact microstrip lowpass filter using a meander-line structure," *Microwave and Optical Technology Letters*, vol. 48, no. 7, 1339-1341, 2006.

[4] H. Liu, R. H. Knoechel, and K. F. Schuenemann, "Miniaturized bandstop filter using meander spurline and capacitively loaded stubs," *ETRI Journal*, vol. 29, n. 5, 614-618, 2007.

[5] G. L. Wu, W. Mu, X. W. Dai, and Y. C. Jiao, "Design of novel dual-band bandpass filter with microstrip meander-loop resonator and CSRR DGS," *Progress In Electromagnetics Research, PIER 78*, 17-24, 2008.

[6] M. Naser-Moghadasi, M. Alamolhoda, and B. Rahmati, "Spurious response suppression in hairpin filter using DMS integrated in filter structure," *Progress In Electromagnetics Research C*, vol. 18, 221-229, 2011.

[7] E. Metlevskis and R. Martavicius, "Computer models of meander slow-wave system with additional shields," *Electronics and Electrical Engineering*, vol. 119, no. 3, 2012.

[8] C. Kim, J. Park, D. Ahn, and J. Lim, "A novel 1-D periodic defected ground structure for planar circuits," *IEEE Microwave and Guided Wave Letters*, vol. 10, no. 4, 2000.

[9] L. H. Weng, Y. C. Guo, X. W. Shi, and X. Q. Chen, "An overview on defected ground structure," *Progress In Electromagnetics Research B*, vol. 7, 173-189, 2008.

[10] J. Xiao, S. Ma, and Y. Li, "A novel h-shaped microstrip resonator and its design to filter using defected ground structure," *High Density Microsystem Design and Packaging and Component Failure Analysis, Conference, 2005.*

[11] H. Liu, Z. Li, and X. Sun, "Compact defected ground structure in microstrip technology," *Electronics Letters*, vol. 41, 132-134, 2005.

[12] H. Liu, Z. Li, X. Sun, and J. Mao, "Harmonic suppression with photonic bandgap and defected ground structure for a microstrip patch antenna," *IEEE Microwave and Wireless Components Letters*, vol. 15, 55-56, 2005.

[13] M. Salehi, A. Motevasselian, A. Tavakoli, and T. Heidari, "Mutual coupling reduction of microstrip antennas using defected ground structure," *10th IEEE International Conference on Communication Systems*, 1-5, 2006.

[14] S. H. Zainud-Deen, M. E. S. Badr, E. El-Deen, K. H. Awadalla, and H. A. Sharshar, "Microstrip antenna with defected ground plane structure as a sensor for landmines detection," *Progress In Electromagnetics Research B*, vol. 4, 27-39, 2008.

[15] F. Y. Zulkifli, E. T. Rahardjo, and D. Hartanto, "Radiation properties enhancement of triangular patch microstrip antenna array using hexagonal defected ground structure," *Progress In Electromagnetic Research M*, vol. 5, 101-109, 2008.

[16] B. T. Tan, S. T. Chew, M. S. Leong, and B. L. Ooi, "A modified micrstrip circular patch resonator filter," *IEEE Microwave and Wireless Components Letters*, vol. 12, no. 7, 252-254, 2002.

[17] R. Dehdasht-Heydari and M. Naser-Moghadasi, "Introduction of a novel technique for the reduction of cross polarization of rectangular microstrip patch antenna with elliptical DGS," *Journal of Electromagnetic Waves and Applications*, vol. 22,

no. 8-9, 1214-1222, 2008.

[18] X. Q. Chen, L. X. Wang, L. H. Weng, and X. W. Shi, "Compact low pass filter using novel elliptic shape DGS," *Microwave and Optical Technology Letters*, vol. 51, no. 4, 1088-1091, 2009.

[19] J. Zhang, B. Cui, S. Lin, and X. W. Sun, "Sharp-rejection low-pass filter with controllable transmission zero using complementary split ring resonators (CSRRS)," *Progress In Electromagnetic Research, PIER 69*, 219-226, 2007.

[20] S. S. Karthikeyan and R. S. Kshetrimauim, "Compact wideband bandpass filter using open slot split ring resonator and CMRC," *Progress In Electromagntics Research Letters*, vol. 10, 39-48, 2009.

[21] G. E. Al-Omair, S. F. Moahmoud, and A. S. Al-Zayed, "Lowpass and bandpass filter design based on DGS with complementary split ring resonators," *Applied Computational Electromagnetics Society Journal*, vol. 26, no. 11, 907-914, 2011.

[22] S. W. Ting and K. W. Tam, "Miniaturized microstrip lowpass filter with wide stopband using double equilateral u-shaped defected ground structure," *Microwave and Wireless Components Letters*, vol. 16, no. 5, 240-242, 2006.

[23] D. H. Bi and Z. Y. Yu, "Study of dual stopbands UWB antenna with u-slot and v-slot DGS," *Journal of Electromagnetic Waves and Applications*, vol. 22, no. 17-18, 2335-2346, 2008.

[24] H. W. Lui, "Design of a miniaturized HTS mictrostrip resonator with slotted ground plane," *J. of Active and Passive Electronic Devices*, vol. 4, 257-280, 2009.

[25] A. Boutejdar, S. Amari, A. Elsherbini, A. S. Omar, "A novel lowpass filter with ultra-wide stopband and improved q-factor performance using h-defected ground structure (DGS)," *IEEE Antennas and Propagation Society International Symposium*, 1545-1548, 2007.

[26] L. Maloratsky, "Using modified microstrip lines to improve circuit performance," *High Frequency Electronics*, March 2011.

[27] A. Boutejdar, A. Sherbini, W. Ali, S. Fouad, L. Ahmed, and A. Omar, "Design of compact microstrip lowpass filters using coupled half-circle defected ground structures," *IEEE Antennas and Propagation Society International Symposium*, 2008.

[28] M. H. Al Sharkawy, D. A. El-Aziz, and E. G. Mahmoud, "A miniaturized lowpass/bandpass filter using double arrow head defected ground structure with centered etched ellipse," *Progress In Electromagnetics Research Letters*, vol. 24, 99-107, 2011.

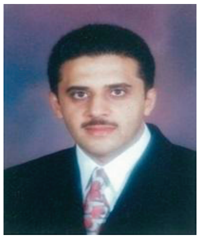

Ayman S. Al-Zayed received his B.Eng. (Honours) degree in Communication and Electronic Engineering from the University of Northumbria at Newcastle in 1995. In 2000, he obtained his M.S. degree in Electrical Engineering from the University of Hawaii at Manoa. In 2004, he earned his Ph.D. degree in Electrical Engineering from North Carolina State University. In February 2004, he joined the Department of Electrical Engineering at Kuwait University as an Assistant Professor, where he was promoted to Associate Professor in March 2012. His research interests include microwave and millimeter-wave active and passive devices, power combining, quasi-optical devices, antennas, phased arrays and radars.

Mekdad Asad Allah graduated from the University of Texas-Austin, in 2008 receiving his B.Sc. in Electrical Engineering and the B.Sc. in Pure Mathematics. He earned his M.Sc. in Electrical Engineering from Purdue University in 2010. He currently works at Kuwait National Petroleum Company as a Power Electrical Maintenance Engineer. He worked as a full-time Teaching Assistant at Kuwait University during the academic year 2012-2013. His research interests are in the areas of numerical electromagnetics, microwave and RF design and antenna.

Samir F. Mahmoud graduated from Cairo University, Egypt, in 1964 and received his M.Sc. and Ph.D. degrees in Electrical Engineering from Queens University, Kingston, ON, Canada, in 1970 and 1973. During the academic year 1973-1974, he was a Visiting Research Fellow at the Cooperative Institute for Research in Environmental Sciences (CIRES), Boulder, CO, doing research on communication in tunnels. He spent two sabbatical years, 1980 to 1982, between Queen Mary College, London, U.K. and the British Aerospace, Stevenage, U.K., where he was involved in design of antennas for satellite communication. Currently, he is a Full Professor in the Electrical Engineering Department, Kuwait University. Recently, he visited several universities and centres including Interuniversity Micro-Electronics Centre (IMEC), Leuven, Belgium and spent a sabbatical leave at Queens University and the Royal Military College, Kingston, ON, Canada in 2001 to 2002. His research activities have been in the areas of antennas, geophysics, tunnel communication, EM wave interaction with composite materials and Microwave integrated circuits. Mahmoud is a Fellow of the Institution of Engineering and Technology (IET), London, U.K. and was co-recipient of the 2003 Best Paper Award of IEEE Transactions on Microwave Theory and TECHNIQUES.

Finite-Difference Time-Domain Modeling of Ultra-High Frequency Antennas on and Inside the Carbon Fiber Body of a Solar-Powered Electric Vehicle

Katherine Han [1], Paul Freeman [2], Hai-Yue Han [3], Jacob Hamar [4], and James F. Stack, Jr. [5]

[1] School of Chemical, Biological, and Environmental Engineering
Oregon State University, Corvallis, OR 97331, USA
vanwormk@onid.orst.edu

[2] School of Electrical Engineering and Computer Science
Oregon State University, Corvallis, OR 97331, USA
freemapa@onid.orst.edu

[3] Inspired Light, LLC.
Corvallis, OR 97330, USA
haiyuehan@gmail.com

[4] School of Mechanical, Industrial, and Manufacturing Engineering
Oregon State University, Corvallis, OR 97331, USA
jchamar@gmail.com

[5] Remcom, Inc.
315 S. Allen St., Suite #416, State College, PA 16801, USA
jim.stack@remcom.com

Abstract **─** Finite-difference time-domain simulations are performed on a 900 MHz band antenna inside and outside the carbon fiber body of a solar-powered electric vehicle. Data is analyzed to determine the optimal antenna placement for transmission to a receiving antenna located toward the rear of the solar vehicle. Modeling data is compared to experimental results. Computational fluid dynamics are used to determine acceptability of external antenna placement. It is found that the ideal antenna would be inside the vehicle's body and oriented vertically, but that the portion of the body surrounding the antenna must be constructed of a non-conductive material.

Index Terms **─** Antenna CFD, FDTD and vehicle antenna modeling.

I. INTRODUCTION

Since the first World Solar Challenge in 1987, student groups and others from around the world have been designing, building and racing solar-powered electric vehicles. These vehicles, primarily one-person, three-wheeled vehicles are designed to travel during the daylight hours for one to two weeks across 1200 to 2400 miles, while only charging their batteries from their solar array. During this race, the solar vehicle is flanked in front and back by lead and chase vehicles in order to protect the solar vehicle.

Radio communication, both audio and telemetry data, is required between these vehicles to enhance safety and racing strategy. The telemetry receiving antenna is usually located behind the solar vehicle in the chase vehicle.

Over the last two decades, radio and cell

Submitted On: June 21, 2013
Accepted On: March 8, 2014

phone communication in passenger vehicles has been studied by several types of modeling and experimentation [1]. Applications from modeling and experimentation include installing miniature printed magnetic phonic crystal antennas into vehicular platforms and studying the effects of signal bounce and attenuation on vehicles in urban environments [2, 3]. Modeling methods have included Method of Moments (MoM) [4-8], Geometric Theory of Diffraction (GTD) [9], Finite-Integration (FI) [10, 11] and Finite-Difference Time-Domain (FDTD) [12]. All of these methods require significant computer resources to solve and report the field strength or gain patterns and polarization information of antenna signals within or around a vehicle. FDTD is a simple and accurate approach to a differential numerical solution of Maxwell's curl equations [13]. The FDTD method allows simulation of complex geometric shapes, uses no linear algebra, is accurate and robust, treats impulsive or nonlinear behavior naturally, is a systematic approach to modeling and is becoming increasingly powerful as computing resources improve [13].

The FDTD method was first described in 1966 by Yee [14]. This research proposed what is now known as the Yee cell, a method of gridding a physical model in order to solve alternately for the electric and magnetic fields in the modeling space as the simulation steps through time. This method is a numerical solution to Maxwell's curl equations, which describe the behavior of the electric and magnetic fields of EM radiation in one, two, or three dimensions. Until recently, most three dimensional simulation methods including FDTD, were too computationally demanding to simulate large models. However, advances in personal computing technology have enabled highly accurate modeling of complicated structures in three dimensions.

This study uses Remcom's XF 7.3.0 software to simulate the electromagnetic fields around the 2012 Oregon State University solar vehicle, resulting from a 900 MHz band antenna. Antenna placement is explored. The goal of the investigation is to determine the optimal antenna placement for data transfer to the chase vehicle during the solar vehicle competitions. To determine effects of antenna location on vehicle efficiency, all simulations with external antenna locations are also analyzed for aerodynamic effects using computational fluid dynamics.

II. METHODS

FDTD simulations were carried out using Remcom's XF 7.3.0 software. A PEC monopole antenna with a center frequency of 915 MHz was modeled to represent the antenna of the FLC910E Ethernet radio from Data-Linc Group. The solar vehicle body, titanium frame and human driver were modeled in XF, with the vehicle body modeled as a thin carbon fiber shell with a conductivity of $2\text{x}10^5$ S/m [15]. The antenna was fed with a 50 ohm voltage source excited at 915 MHz. Outer boundary conditions were all set to Perfectly Matched Layer (PML) conditions with seven absorbing layers. Far field sensors were used to detect realized gain. Realized gain is the gain of the antenna reduced by impedance mismatch losses. This allows for a consistent, qualitative comparison of system performance between potential antenna locations. Solidworks Flow Simulation 2013 was used to perform the Computational Fluid Dynamics (CFD) for 50 mph air flow. A computational domain that is 80 meters long, 20 meters wide and 6 meters tall was setup with a velocity opening in the front of the vehicle, a ground plane with moving air below the vehicle and environment (1 atmosphere at STP) pressure openings on the remaining sides of the car. The vehicle was located 30 meters from the front of the opening, centered width wise and was placed 6 inches above ground for ground clearance.

Experimental results were obtained by recording signals around the frequencies of interest (900-912 MHz) for five seconds of data, using a Terratec T Stick software defined radio. The software defined radio antenna was oriented vertically for all vertical antenna positions and horizontally for all horizontal positions. Measurements were taken at twelve evenly spaced locations around the car, fifteen feet from the center of the vehicle. The vehicle and all antennas were in the center of a field away from any other buildings or significant metal objects. Normalized average power was computed for each data point by:

$$P = 10log\left(\left[\frac{A}{N}\right]^2\right), \quad (1)$$

where P is the normalized average power at a particular XY point and antenna position, A is the amplitude of the FFT under those conditions and N is the normalization factor, or the average amplitude of the FFT of all twelve XY points for the top vertical antenna position.

III. RESULTS

Six different antenna positions were analyzed for their gain patterns (see Fig. 1). The "inside back" position is the location of the antenna during the 2012 American Solar Challenge. "Inside front" is a proposed internal position for improving gain toward the receiver. The "top" and "back" positions are proposed external positions that are likely to improve the gain but could potentially increase aerodynamic drag. Both horizontal and vertical orientations are analyzed at these external locations. Vertically polarized realized gain plots were analyzed for each antenna location in the XY, YZ and XZ planes (Figs. 2, 3 and 4). Special attention was paid to transmission toward the rear of the vehicle, as that is the location of the receiving antenna in the chase vehicle during highway races. To address concerns of increased aerodynamic drag due to antenna placement outside the vehicle, Computational Fluid Dynamics (CFD) was performed on the vehicle with and without external antennas. For EM safety analysis, SAR data is considered for each antenna position.

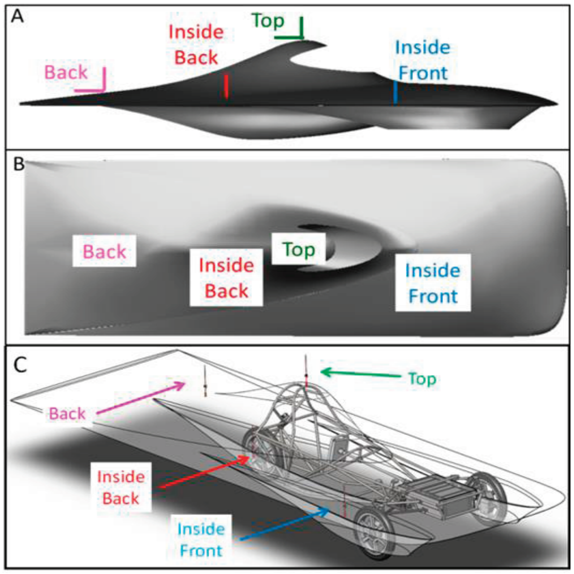

Fig. 1. Locations of antenna in and on the solar vehicle body. Positions "inside back" and "inside front" are inside the body and are both vertical antennas. Positions "top" and "back" are outside and are analyzed for both vertical and horizontal antennas. Colors of the numbers in this figure correlate to the colors of the lines in Figs. 2, 3 and 4.

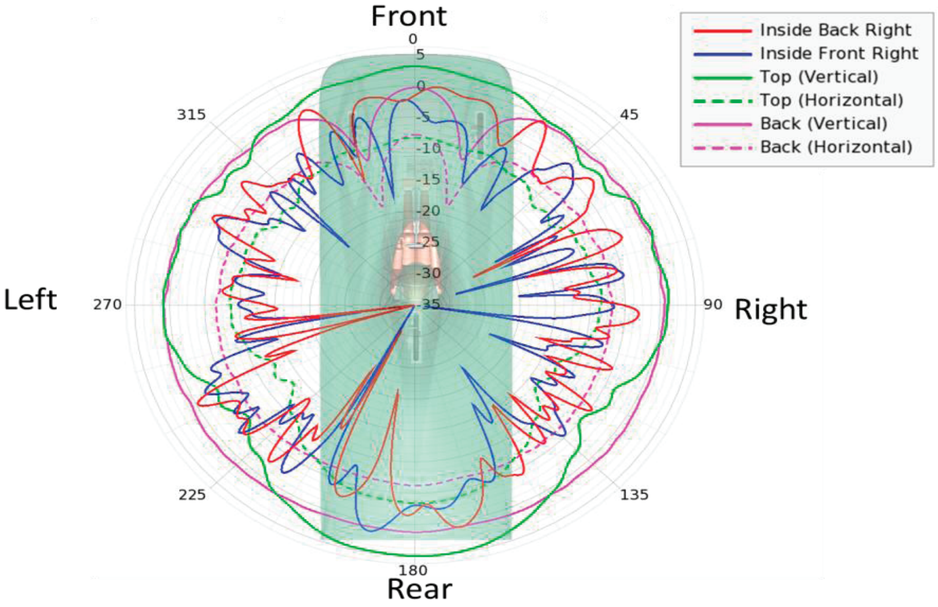

Fig. 2. XY cut of a theta-polarized realized gain plot for six antenna positions.

Realized gain was analyzed for antennas located inside the solar vehicle's body. "Inside back" is the antenna placement during the 2012 American Solar Challenge and "inside front" is a proposed improved antenna location that is closer to the windshield (see Fig. 1); both modeled in a vertical orientation. It was found that for both internal antenna locations, the signal strength toward the rear of the vehicle was significantly attenuated when observing both the XY and YZ realized gain plots, compared to external antenna locations (see red and blue lines in Figs. 2 and 4, respectively). In the XZ gain plot the inside back antenna displays a null at 270 degrees (toward the right of the vehicle; see Fig. 4), which may explain some of the communication difficulty when the car is racing on a track and the receiver is stationary. Transmission in all directions of the XY plane is important during track races. The internal antennas were both found to have relatively high gains toward the top of the vehicle (see Figs. 3 and 4).

In an attempt to increase signal strength toward the rear of the vehicle, vertically-oriented antennas were modeled at the top of the vehicle and the center back of the vehicle (see Fig. 1). These vertical external antennas both showed significantly increased gain toward the right and left of the vehicle, with the top antenna being the strongest transmitter (see the solid green line in Figs. 2 and 3).

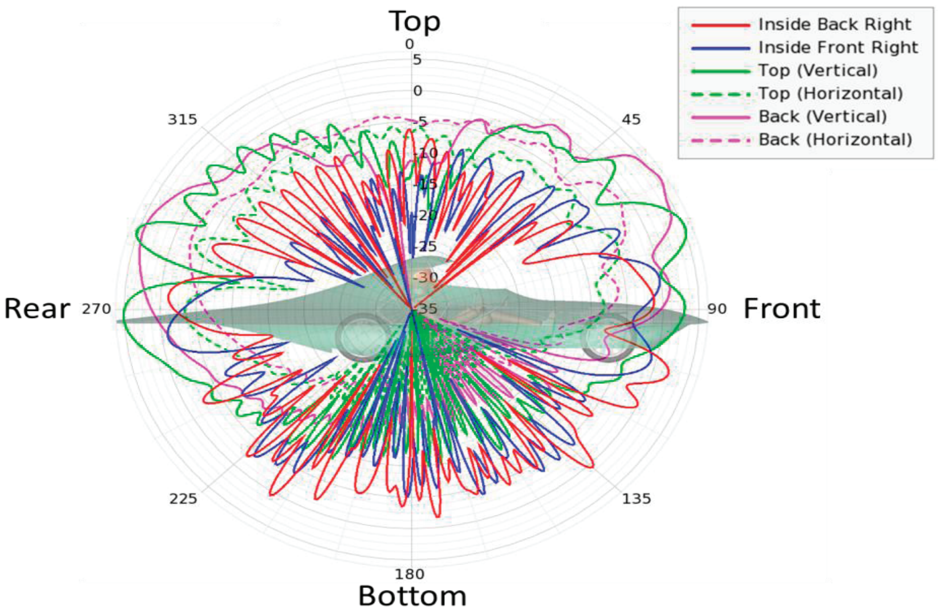

Fig. 3. YZ slice of theta-polarized realized gain plot for the six antenna positions.

With the prediction that they would cause less aerodynamic drag than vertical antennas, horizontal antennas in these two external locations were modeled for their signal gain and aerodynamics. Computational Fluid Dynamics (CFD) modeling was performed on the bare solar vehicle body as well as the body with each of the four externally located antenna positions. It was found that all antenna positions had negligible drag impact on the car at 50 mph, as determined by CFD. Also, as seen in the dotted lines of Fig. 2, the signal gain in the XY direction for a horizontally polarized antenna is not as strong as for the vertically polarized antennas, making horizontal antennas doubly undesirable.

SAR data was analyzed to determine the energy absorbed by a 147 lb human phantom in the driver's seat for each antenna position. All external antenna locations resulted in no energy absorbed. The inside front and inside back positions produced peak absorption of 4 and 2 mW/kg, respectively (both averaging about 2 mW/kg). If the carbon fiber backing on the seat is removed, the energy absorbed from the antenna located in the inside back location increases to a peak 1 g average SAR of 170 mW/kg.

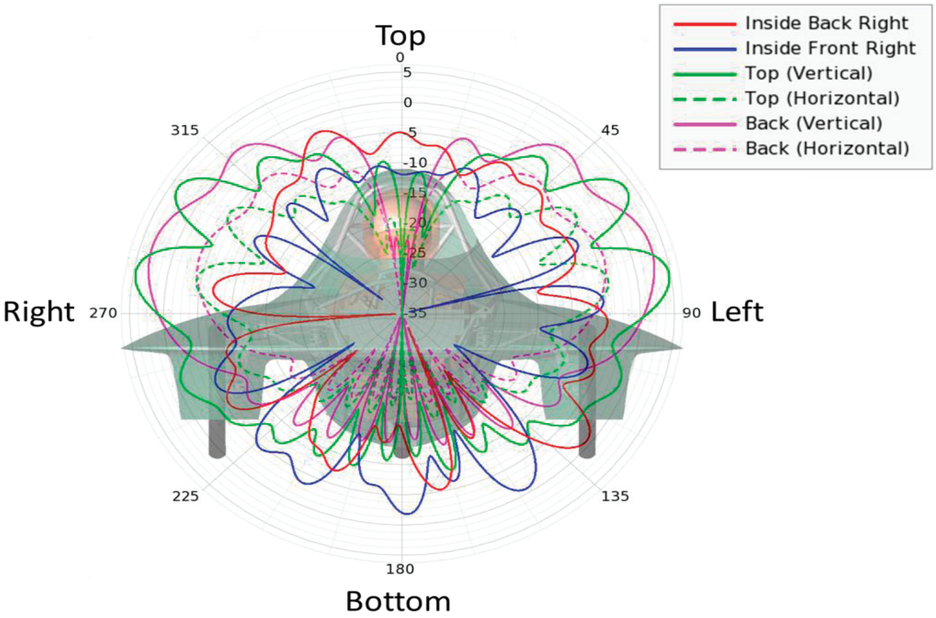

Fig. 4. XZ slice of theta-polarized realized gain plot for the six antenna positions.

Experimental results were obtained using a software-defined radio. To make the modeling results more comparable to the experimental results, modeling results were reported for the polarization that matches the transmitting antenna orientation; theta polarized data are reported for vertical antenna positions and phi results are reported for horizontal antenna positions (see Fig. 5 (a)). Experimental results were obtained with the receiving antenna in the same orientation as the transmitting antenna in or on the car. As seen with the modeling results, external vertical antenna positions were by far the strongest locations, with the overall strongest transmitting position being the top vertical (see Fig. 5 (b)). Although we had expected that the inside antenna positions would be least powerful, we found that the positions with the lowest transmission were the inside front and outside back horizontal. The top horizontal antenna position performed better than expected. The location of the antenna during the 2012 American Solar Challenge, the inside back was found to be a mediocre position, a stronger performer at all measured locations in the XY plane than the inside front, but generally weaker than external vertical antennas.

IV. DISCUSSION

The telemetry antenna modeled in this study is required to transmit data between the solar vehicle and its chase vehicle, which is located toward the solar vehicle's rear during cross country races and anywhere in the XY plane during track races. Six antenna positions were studied to assess their signal strength and aerodynamic drag for purposes of choosing the best antenna position and orientation for racing conditions. The optimal antenna position would be one where the signal strength is high toward mainly the rear, but also the sides and front of the vehicle and the aerodynamic drag is not significantly increased.

It was found that although externally placed, vertical antennas are most effective at transmitting signal toward the rear of the vehicle. The body of the solar vehicle is designed to hold the solar array, contain the driver and electronics and have as little aerodynamic drag as possible. This is done by minimizing both the frontal cross sectional area and low pressure regions on the back side of any structures in the vehicle. The antenna modeled here does not appear to contribute a detectable amount of drag by Solidworks 2013 Flow Simulation. Experimental studies have shown that vehicle antennas typically produce approximately 1 N of drag force, which would be approximately 23 W of power loss [16]. Although this is a significant amount of drag in solar car racing (23 W of drag could decrease average speed by 0.5 or 1 mph), it is not accurately detectable using CFD.

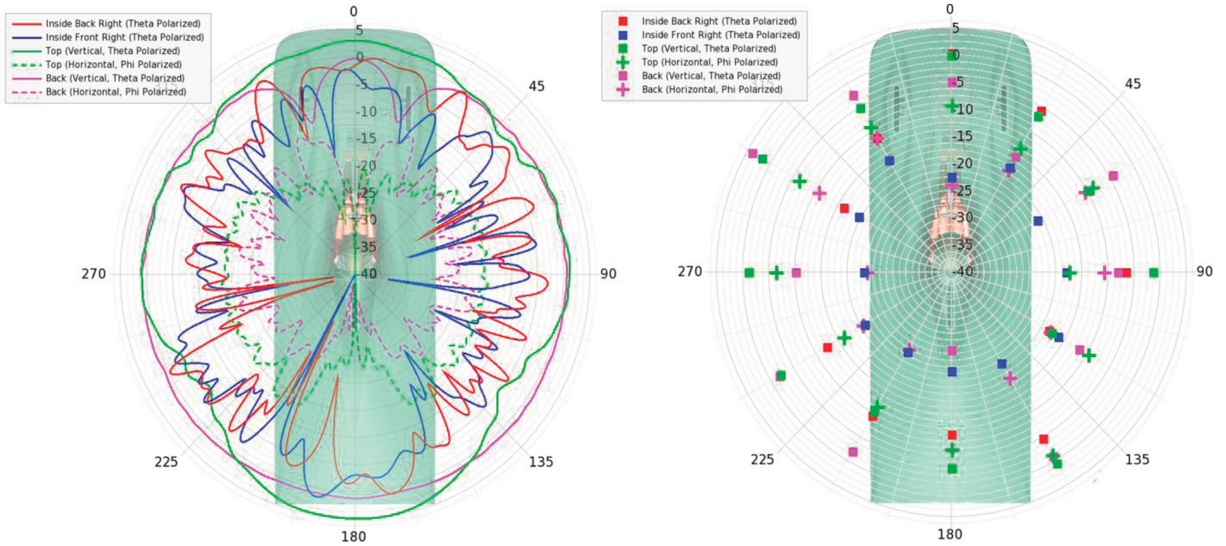

(a) (b)

Fig. 5. (a) XY slice of realized gain from modeling and (b) normalized average power from experimental measurements.

Modeling and experimental results suggest that the proposed internal antenna position, “internal front,” was not any better for transmission in the XY plane than was the original “internal back” position. Experimental results confirmed that in fact, the “internal front” position was a worse location for the transmitting antenna than “internal back.”

Simulations suggest that horizontal positioning of the antenna on the outside of the vehicle was found to improve neither the aerodynamics nor the signal transmission in the XY plane, which is the plane of interest to receivers at ground level. The signal transmission of a horizontal antenna is expected to be reduced in the horizontal direction. The two horizontal antenna positions modeled did show a higher gain toward the +z axis (above the vehicle), but this information is only useful if one were interested in detecting the signal from the space above the vehicle. Experimental results in the XY plane indicate that horizontal orientation of the antenna in the back of the vehicle is highly discouraged, while a horizontal antenna on the top of the vehicle produced higher than expected signal strength.

Discrepancies between modeled and simulated results could come from several factors. In the simulation the car was modeled in free space without ground underneath, while during experiments the car was in a field. The simulation did not include every component currently on the car, there are several electronic and some small mechanical systems that were not practical to simulate.

SAR data indicate that all antenna locations are very much below the FCC safety limit of 1600 mW/kg peak 1 g averaged SAR (80 mW/kg whole body average SAR). The carbon fiber seat back had a significant effect on energy absorbed by the driver. Removal of the seat back increased the peak energy by more than 40x, resulting in an energy absorption that is about 10% of the FCC limit. Thus, the internal configuration of the vehicle could affect the safety of the antenna, especially if multiple antennas are to be considered.

It is concluded that two of the proposed antenna positions will satisfy both of the design constraints of increased XY transmission and low aerodynamic drag, compared to the original placement used in the 2012 American Solar Challenge. Future improvements of the vehicle would include incorporating a vertical antenna inside the body of the vehicle, but in an area that is free of conductive carbon fiber. Other solutions to explore are antennas incorporated into the composite structure of the car's body surrounded by non-conductive materials. The simulation and modeling data are found to be in enough agreement to help the designers engineer better communications in future revisions of the vehicle.

ACKNOWLEDGEMENT

Special thanks to Remcom, Inc. for their support of the Oregon State University Solar Vehicle Team and their assistance with this paper.

REFERENCES

[1] Y. Yamagucki, T. Abe, and T. Sekigucki, "Radio wave propagation loss in the VHF to microwave region due to vehicles in tunnels," *IEEE Transactions on Electromagnetic Compatibility*, vol. 31, pp. 87-91, 1989.

[2] E. Irci, K. Sertel, and J. L. Volakis, "Miniature printed magnetic photonic crystal antennas embedded into vehicular platforms," *Applied Computational Electromagnetics Society Journal*, vol. 26, pp. 109-114, February 2011.

[3] Y. H. Wang, X. Xing, and Y. Zhang, "Characterization of packet-level measurements for vehicular wireless networks," *Applied Computational Electromagnetics Society Journal*, vol. 27, pp. 532-540, June 2012.

[4] E. K. Walton, R. Abou-Jaoude, and M. E. Pekar, "Annular slot windshield antenna," *IEEE Transactions on Vehicular Technology*, vol. 47, pp. 766-773, 1998.

[5] R. Abou-Jaoude and E. K. Walton, "Numerical modeling of on-glass conformal automobile antennas," *IEEE Transactions on Antennas and Propagation*, vol. 46, pp. 845-852, 1998.

[6] H. Nagatomo, Y. Yamada, K. Tabira, T. Itagaki, and S. Yuminaga, "Radiation from multiple reflected waves emitted by a cabin antenna in a car," *Ieice Transactions on Fundamentals of Electronics Communications and Computer Sciences*, vol. E85A, pp. 1585-1593, July 2002.

[7] S. Horiuchi, K. Yamada, S. Tanaka, Y. Yamada, and N. Michishita, "Comparisons of simulated and measured electric field distributions in a cabin of a simplified scale car model," *Ieice Transactions on Communications*, vol. E90B, pp. 2408-2415, September 2007.

[8] J. C. Batchelor, R. J. Langley, and H. Endo, "On-glass mobile antenna performance modelling," *Iee Proceedings-Microwaves Antennas and Propagation*, vol. 148, pp. 233-238, August 2001.

[9] K. Nishikawa and Y. Asano, "Vertical radiation-patterns of trunk mount antennas for mobile radio-communications," *Ieice Transactions on Communications Electronics Information and Systems*, vol. 74, pp. 3227-3232, October 1991.

[10] L. Low, R. Langley, and J. Batchelor, "Modelling and performance of conformal automotive antennas," *Iet Microwaves Antennas & Propagation*, vol. 1, pp. 973-979, October 2007.

[11] R. Ehmann, B. Wagner, and T. Weiland, "Farfield calculations for car antennas at different locations," *IEEE Transactions on Magnetics*, vol. 33, pp. 1508-1511, 1997.

[12] Y. Tarusawa, S. Nishiki, and T. Nojima, "Fine positioning three-dimensional electric-field measurements in automotive environments," *Ieee Transactions on Vehicular Technology*, vol. 56, pp. 1295-1306, May 2007.

[13] A. Taflove and S. C. Hagness, "Computational electrodynamics: the finite-difference time-domain method," 3rd ed., *Artech House, Inc.*, Norwood, MA, 2005.

[14] K. S. Yee, "Numerical solution of initial boundary value problems involving Maxwell's equations in isotropic media," *IEEE Trans. Antennas Propagat.*, vol. 14, pp. 302-307, 1966.

[15] V. Safarova and J. Gregr, "Electrical conductivity measurement of fibers and yarns," *7th International Conference-TEXSCI*, 2010.

[16] F. Alam, H. Chowdhury, H. Moria, and S. Watkins, "Effects of vehicle add-ons on aerodynamic performance," *In Proceedings of the 13th Asian Congress of Fluid Mechanics*, Dhaka, Bangladesh, 2010.

Katherine Han is currently a Ph.D. student in the School of Chemical, Biological, and Environmental Engineering at Oregon State University. She is a co-founder of the OSU Solar Vehicle Team and has served as Graduate Student President in her department. Han is currently the Lab Manager for the Oregon Process Innovation Center.

Paul Freeman is a senior in Computer Science at Oregon State University. His education emphasizes cognitive science, artificial intelligence, computer ethics and goal-directed computation. He is a member of American Mensa, the Upsilon Pi Epsilon honor society for Computing and Information Disciplines and the OSU Solar Vehicle Team. He has worked as a software engineering intern for Intel and Garmin AT. While attending classes, Freeman works as a Teaching Assistant for freshman level computer science students. In addition to his computer science background, Freeman earned an Associates of Applied Arts in Graphic Design at Portland Community College.

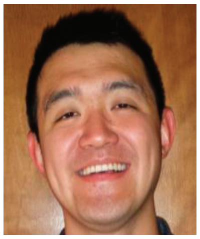

Hai-Yue Han received his Ph.D. in Electrical Engineering at Oregon State University. He is a co-founder of the Oregon State University Solar Vehicle Team and has built three solar powered cars at OSU. He currently works as the lead balance of systems engineer at Inspired Light.

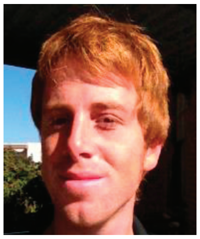

Jacob Hamar is currently a junior of Mechanical Engineering at Oregon State University. He is working as a Controls Engineer at Daimler Trucking North America and is co-captain of the Oregon State University Solar Vehicle Team. Hamar's interests include water desalination, aerospace and energy technology.

James F. Stack, Jr. received his B.S. degree in Electrical Engineering from the Pennsylvania State University in 2001 and his M.E. degree in Systems Engineering from the Pennsylvania State University in 2010. He has worked for Remcom, Inc. since 2000, where he currently manages the Applications Engineering Department. His research interests include high performance computing (SSE/AVX vectorization, GPGPU, MPI and threading) and using optimization techniques to achieve novel RF structures.

Ultra-Wideband Antenna with Variable Notch Band Function by Defected Ground Structure and Shorting Pin

Mohammad Akbari [1,2], Reza Movahedinia [2], and Abdelrazik Sebak [2]

[1] Young Researchers and Elite Club
Islamic Azad University, Central Tehran Branch, Tehran, Iran

[2] Electrical and Computer Department
Concordia University, Quebec H3G 1M8, Canada

akbari.telecom@gmail.com

Abstract **─** In this paper, a simple miniaturized printed antenna for ultra-wideband applications with variable band-notch function is proposed. The presented antenna consists of a square radiating patch and a ground plane with inverted T-shaped slot, which increases the bandwidth of 2.3-11 GHz. Frequency band-stop performance is created by two techniques: Defected Ground Structure (DGS) and shorting pins. The designed antenna has a small size of 17×21×1 mm^3, while showing the band rejection performance in the frequency bands of 3.2 to 3.8 and 5.1 to 5.85 GHz, respectively.

Index Terms **─** antenna, DGS (Defected Ground Structure), notch band and shorting pin.

I. INTRODUCTION

Commercial Ultra-Wideband (UWB) systems require compact, cheap antennas with omni-directional radiation patterns and extended bandwidth [1]. It is a renowned fact that monopole antennas present really appealing physical features, such as simple structure, small size and low cost. Due to all these fascinating characteristics, planar monopoles are quite appealing to be used in emerging UWB applications and growing research activity is being focused on them. In UWB communication systems, one of major subjects is the design of a small antenna while providing wideband characteristic over the total operating frequency band. Consequently, a big number of microstrip antennas with various structure have been experimentally characterized [2-6]. The frequency range for UWB systems between 3.1 and 10.6 GHz will cause interference to the existing wireless communication systems; as an example the Wireless Local Area Network (WLAN) for IEEE 802.11a operating in 5.15-5.35 GHz and 5.725-5.825 GHz bands, so the UWB antenna with a band-stop performance is needed. To create frequency band-notch function, modified planar monopoles have recently been proposed [7-15]. In [7], novel shape of the slot (folded trapezoid) is used to obtain the appropriated band notched characteristics. Single and multiple half-wavelength U-shaped slots are embedded in the radiation patch, to generate single and multiple band-notched [8] functions. In [9], a band-notch function is achieved by using a T-shaped coupled-parasitic element in the ground plane. In this paper, a novel band-notched printed monopole antenna is proposed. The notched bands covering the 3.2 to 3.8 and 5.1 to 5.85 GHz, is provided by using two techniques: Defected Ground Structure (DGS) and shorting pins. Also, by inserting an inverted T-shaped slot on the ground plane, wider impedance bandwidth can be obtained. Measured and simulated results of the constructed miniaturized prototype are presented and discussed.

II. ANTENNA DESIGN

The square monopole antenna is exhibited in Fig. 1, which is printed on a 1 mm thick FR4

Submitted On: June 10, 2013
Accepted On: July 14, 2014

substrate with relative permittivity of 4.4. The width Wf of the microstrip feedline is fixed at 1.9 mm. The basic antenna structure consists of a square patch, a feedline and a ground plane. The square patch has a width Wp. As illustrated in Fig. 1, the patch is connected to a feed line of width Wf and length Lf. On the other side of the substrate, a conducting ground plane of width Wsub and length Lgnd is placed. The proposed antenna is connected to a 50-Ω SMA connector for signal transmission. The ground plane with an inverted T shape is playing an important role in the broadband characteristics of this antenna, because they can adjust the electromagnetic coupling effects between the patch and the ground plane and improves its impedance bandwidth without any cost of size or expense [2]. To obtain two notched bands, two different techniques has been used, the former DGS (Defected Ground Structure) and the latter shorting pin, that will be more examined below.

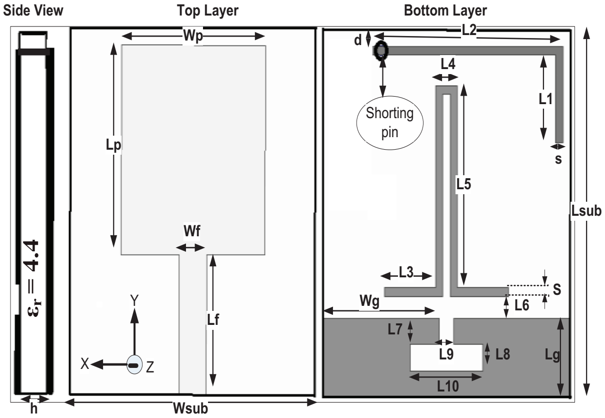

Fig. 1. Geometry of proposed antenna: Wsub=17, Lsub=21, Lp=12, Wp=10, Wf=1.9, Lf=8, Wg=8, Lg=4.5, d=1, L1=3, L2=13, L3=3.5, L4=1.5, L5=11.5, L6=1.25, L7=1.5, L8=1.5, L9=1, L10=5, S=0.5, h=1 and εr=4.4.

III. ANTENNA PERFORMANCE AND DISCUSSION

The performance analysis of the proposed antenna is carried out in both frequency and time-domain.

A. Frequency-domain analysis

In this part, the square monopole antenna with different design parameters were constructed and the numerical and experimental results of the input impedance and radiation characteristics are presented and discussed. The parameters of this proposed antenna are studied by changing one parameter at a time and fixing the others. The simulated results are obtained using the Ansoft simulation software high-frequency structure simulator [16]. Figure 2 depicts the structure of the different square antennas. As illustrated in Fig. 3, bandwidth is increased dramatically and the third resonance has been excited by cutting an inverted T-shaped notch on the ground. The upper frequency limit of the bandwidth is affected by using the pair of L-shaped arms on the back in a way that the L-shaped arms causes to create a resonance at 11 GHz, that extends the bandwidth. However, the main purpose for using a pair of L-shape arms was to obtain a notch.

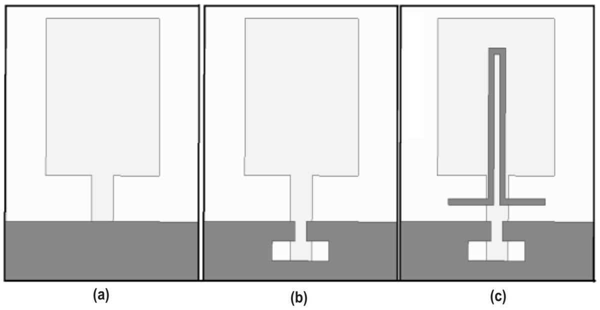

Fig. 2. (a) The ordinary square antenna, (b) the antenna with an inverted T-shape notch on the ground plane and (c) the antenna with a pair of L-shaped arms on the back (DGS technique).

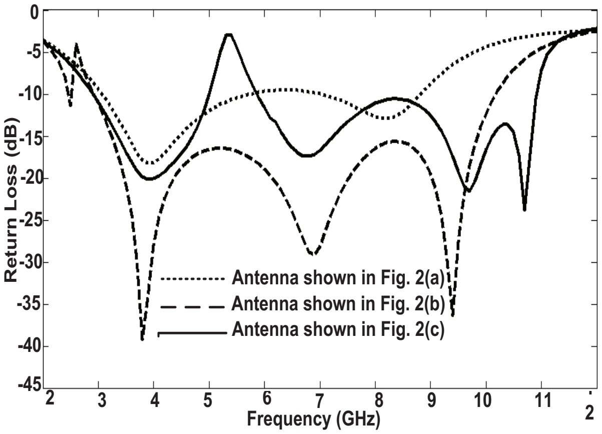

Fig. 3. Simulated return loss characteristics for the various square monopole antenna structures, as shown in Fig. 2.

In this work, through new technique of DGS and by a pair of L-shape arms, a band-stop performance at frequency 5.5 GHz is produced that has an acceptable bandwidth. The central frequency of notch can easily be shifted by some key parameters, like L1. Figure 4 exhibits the different structures of the antenna showing major elements of generating a stop-band, namely a pair of L-shaped arms and shorting pin. Figure 5 demonstrates the Voltage Standing Wave Ratio (VSWR) for the three cases shown in Fig. 4. It is quite apparent that the pair of L-shaped arms has effect on notched band at center frequency 5.5 GHz, while shorting pin produces a stop band at center frequency 3.5 GHz, to filter WLAN and WiMAX bands, respectively.

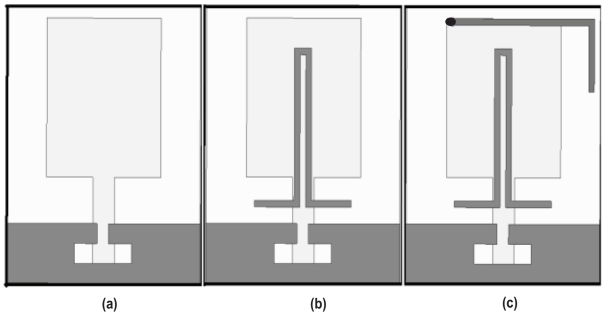

Fig. 4. (a) The square antenna with an inverted T-shaped slot, (b) the square antenna with a pair of L-shaped arms and (c) proposed antenna.

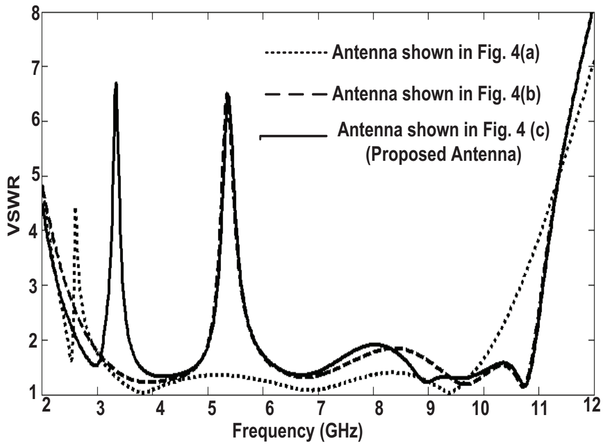

Fig. 5. Simulated VSWR characteristics for antennas shown in Fig. 4.

Meanwhile, it is found out that both notches are autonomous; i.e., they have no effect on each other. As illustrated in Fig. 6, parameter L5 has a considerable influence on frequency shifting. Increasing the length of L5 results in decreasing the center frequency, while the rejection magnitude is nearly constant. A best value L5 for covering 5.15 to 5.825 GHz band, corresponds to 11.5 mm. In this study, to generate the band-stop performance on WiMAX band with center frequency 3.5 GHz, we used an arm with length L1+L2 that has been connected to a shorting pin. The simulated VSWR curves with different values of L1 are plotted in Fig. 7. As shown in Fig. 7, when L1 increases from 1 to 7 mm, the center frequency of the notched band is fallen from 3.8 to 2.8 GHz. Therefore, the optimized L1 is 3 mm. From these results, we can conclude that the notch frequencies are controllable by changing L1 and L5. To understand the behavior of the proposed antenna, Fig. 8 shows simulated current distributions on the radiating patch and a pair of L-shape arms on the back. It can be observed from Fig. 8 (a), that the current is concentrated on the arms and patch using an arm ended up with shorting pin. It can be noticed that the current direction on the patch is opposed (180 degree phase difference) with the current on arm. On the other hand, Fig. 8 (b) depicts the current distribution at 3.5 GHz.

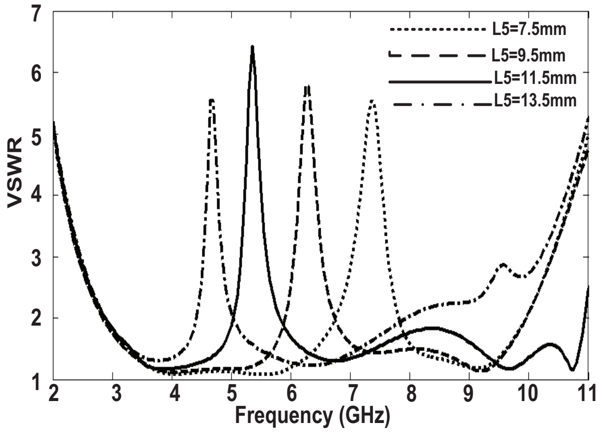

Fig. 6. Simulated VSWR characteristics of the antenna with a pair of L-shaped arms with different values of L5.

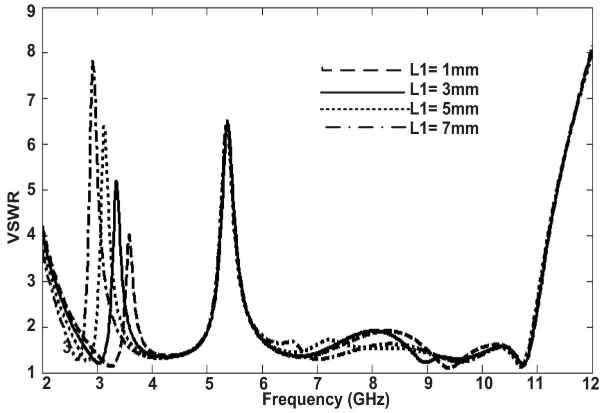

Fig. 7. Simulated VSWR characteristics of the antenna with an arm ended up shorting pin with different values of L1.

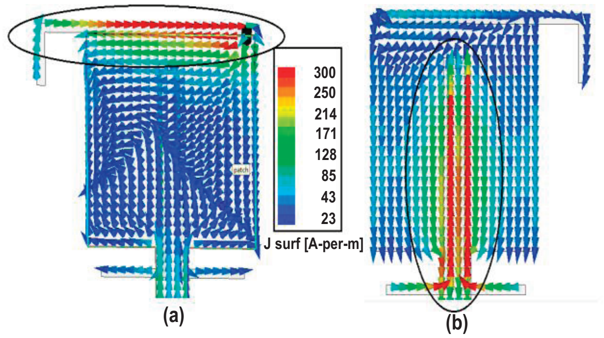

Fig. 8. Simulated surface current distributions on radiating patch: (a) on L-shaped arm ended up shorting pin at 5.5 GHz (bottom view) and (b) on a pair of L-shaped arms at 3.5 GHz (top view).

It is clear that most of the current is seen on the pair of L-shaped arms, with the current directions on the arms are in opposite direction with the current on the patch. The proposed antenna with optimal design, as shown in Fig. 9, was fabricated and tested in the Antenna Measurement Laboratory at Iran Telecommunication Research Center. Figure 10 exhibits the measured and simulated VSWR characteristics of the proposed antenna. The fabricated antenna has the frequency band of 2.3 to over 11 GHz. The designed antenna has a small size of 21×17 mm^2, while showing the band rejection performance in the frequency bands of 3.2 to 3.8 and 5.1 to 5.85 GHz, respectively. The measured and simulated VSWR by both software HFSS [16] and CST [17], are shown in Fig. 10. As shown in Fig. 10, there exists a discrepancy between measured data and the simulated results, and this could be due to the effect of the SMA port.

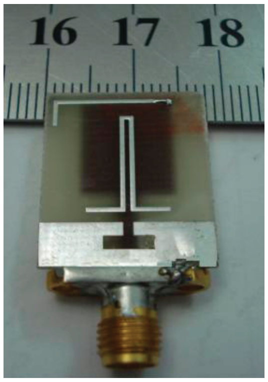

Fig. 9. Photograph of the realized antenna.

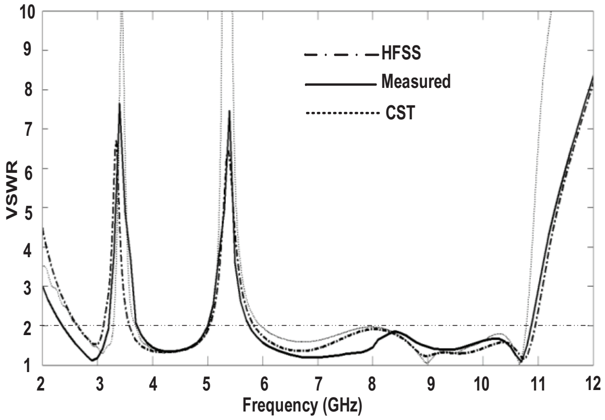

Fig. 10. Measured and simulated VSWR characteristics for the antenna.

Figure 11 illustrates the measured maximum gain of the proposed antenna with and without stop band. A sharp decrease of maximum gain in the notched frequencies band at 3.5 and 5.5 GHz is shown. For other frequencies outside the notched frequency band, the antenna gain with the slot is similar to those without it. Figure 12 shows the measured radiation patterns including the co-polarization and cross-polarization in the H-plane (x-z plane) and E-plane (y-z plane). It can be seen that the radiation patterns in x-z plane are nearly omni-directional for the two frequencies, while radiation pattern in y-z plane are approximately directional.

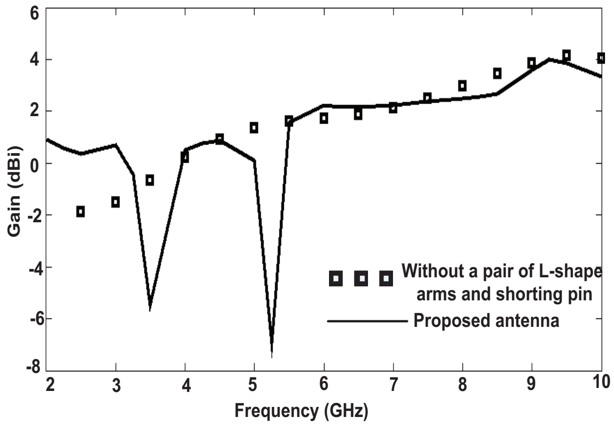

Fig. 11. Measured gain of the antenna with and without stop bands.

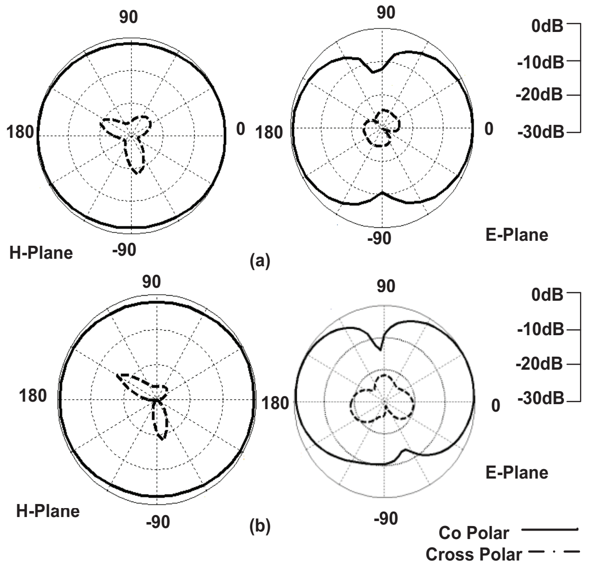

Fig. 12. Measured radiation patterns of the antenna at: (a) 4 and (b) 8 GHz.

B. Time-domain analysis

Computation of the dispersion that happens when the antenna radiates a pulse signal is an important issue in UWB systems. The transmit transfer functions of the antennas were utilized to calculate the radiated pulse in various directions when a reference signal was used at the antenna input. The signal should present an UWB spectrum masking the antenna bandwidth and specially the FCC mask (3.1 up to 10.6 GHz). A pulse of Gaussian seventh derivative is shown in Fig. 13 that is an acceptable approximation to a FCC mask compliant pulse. This pulse is represented in the time domain by:

$$G(t) = A.\exp\left(\frac{-t^2}{2\delta^2}\right), \tag{1}$$

$$G^n(t) = \frac{d^nG}{dt^n} = (-1)^n \frac{1}{(\sqrt{2}\delta)^2} . H_n\left(\frac{t}{\sqrt{2}\delta}\right) . G(t), \tag{2}$$

where for n=7,

$$H_7(t) = 128t^7 - 1344t^5 + 3360t^3 - 1680t. \tag{3}$$

Both signal and spectrum are depicted in Fig. 13. The pulse bandwidth fits very well into the desired mask. Fortunately, after drawing various Gaussian pulses from the first to eighth derivative, it was found that the best pulse to cover the FCC mask is the seventh derivative. Furthermore, with a few tolerance, the sixth and eighth derivative can be acceptable. The correlation between the transmitted (TX) and received (RX) signals in telecommunications systems is evaluated using the fidelity factor (4):

$$F = \max_\tau \left| \frac{\int_{-\infty}^{+\infty} S(t) r(t-\tau) dt}{\sqrt{\int_{-\infty}^{+\infty} S(t)^2 \cdot \int_{-\infty}^{+\infty} r(t)^2 dt}} \right|. \tag{4}$$

In which, S(t) and r(t) are the TX and RX signals, respectively. For impulse radio in UWB communications, it is needful to have a high degree of correlation between the TX and RX signals to avoid losing the modulated information. Although, for most other telecommunication systems, the fidelity parameter is not that relevant. In order to evaluate the pulse transmission characteristics of the antenna without notch, two configurations (side-by-side and face-to-face orientations) were chosen. The transmitting and receiving antennas were placed in a d=25 cm distance from each other [18]. As shown in Figs. 14, the received pulses in each of the two orientations are broadened, a relatively good similarity exists between the RX and TX pulses. Using (4), the fidelity factor for the face-to-face and side-by-side configurations was earned equal to 0.95 and 0.96, respectively. These values for the fidelity factor demonstrate which the antenna imposes negligible effects on the transmitted pulses. The pulse transmission results are obtained using CST [17].

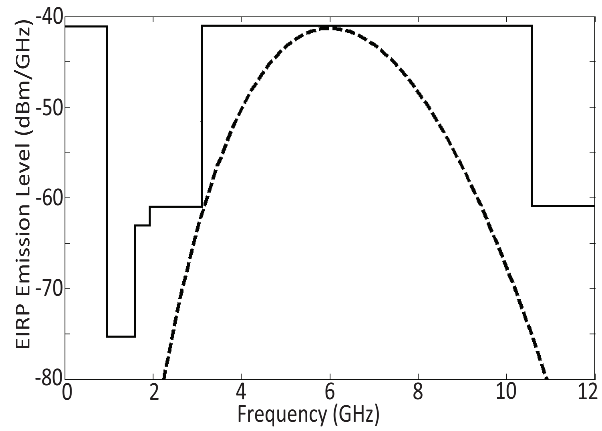

Fig. 13. Power Spectrum Density compared to FCC mask.

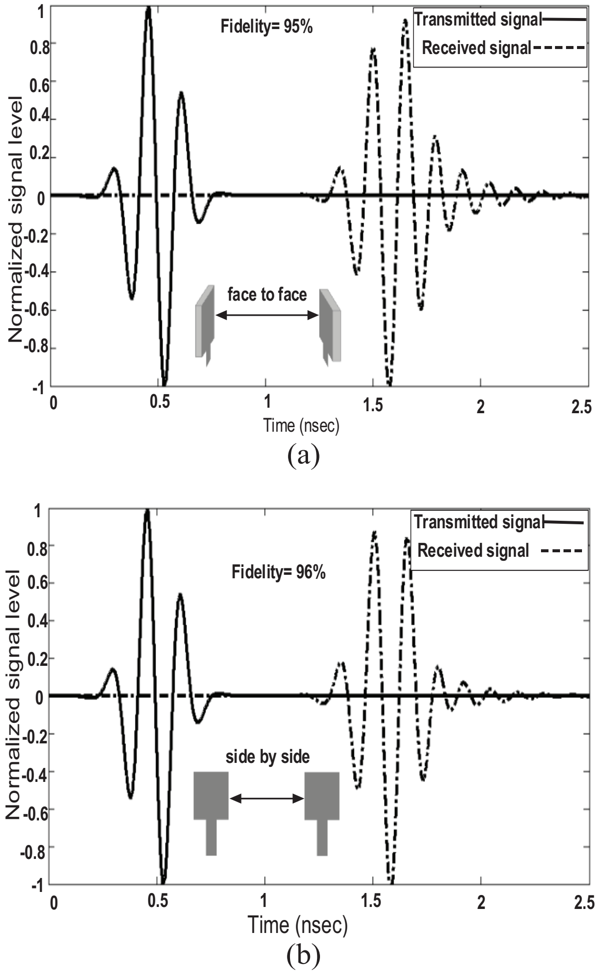

(a)

(b)

Fig. 14. Transmitted and received pulses in time domain for a UWB link with identical antennas without notches in: (a) face-to-face and (b) side by side orientations.

IV. CONCLUSION

In this paper, a novel microstrip antenna with extended bandwidth capability for UWB applications was presented. In this design, the proposed antenna can operate from 2.3 to 11 GHz with VSWR<2 and displays a good omni-directional radiation pattern, even at higher frequencies. The designed antenna has a small size of 17×21 mm^2, while showing a band rejection performance in the frequency bands of 3.2 to 3.8 and 5.1 to 5.85 GHz, respectively. Good return loss and radiation pattern characteristics are obtained in the frequency band of interest. Simulated and experimental results exhibits that the antenna could be a good candidate for UWB application.

REFERENCES

[1] H. Schantz, “The art and science of ultra wideband antennas,” *Artech House*, Norwood, MA, 2005.

[2] M. Akbari, M. Koohestani, C. Ghobadi, and J. Nourinia, “Compact CPW-fed printed monopole antenna with super wideband performance,” *Microwave Opt. Technol. Lett.*, 53, 1481-1483, July 2011.

[3] M. Akbari, M. Koohestani, C. Ghobadi, and J. Nourinia, “A new compact planar UWB monopole antenna,” *International Journal of RF and Microwave Computer-Aided Engineering*, 21, 216-220, 2011.

[4] M. Mighani, M. Akbari, and N. Felegari, “Design of a small rhombic monopole antenna with parasitic rectangle into slot of the feed line for SWB application,” *The Applied Computational Electromagnetics Society*, 27, 74-79, 2012.

[5] M. Mighani, M. Akbari, and N. Felegari, “A CPW dual band notched UWB antenna,” *The Applied Computational Electromagnetics Society (ACES)*, vol. 27, no. 4, 352-359, 2012.

[6] A. A. Eldek, “Numerical analysis of a small ultra wideband microstrip-fed tap monopole antenna,” *Prog. Electromagn. Res. PIER*, 65, 59-69, 2006.

[7] M. Ojaroudi, “Printed monopole antenna with a novel band-notched folded trapezoid ultra-wideband,” *J. Electromagn. Waves Appl.*, 23, 2513-2522, 2009.

[8] M. Ojaroudi, G. Ghanbari, N. Ojaroudi, and C. Ghobadi, “Small square monopole antenna for UWB applications with variable frequency band-notch function,” *IEEE Antennas Wirel. Propag. Lett.*, 8, 1061-1064, 2009.

[9] R. Rouhi, C. Ghobadi, J. Nourinia, and M. Ojaroudi, “Ultra-wideband small square monopole

antenna with band notched function," *Microwave Opt. Technol. Lett.*, 52, 2065-2069, 2010.

[10] Y. S. Li, W. Li, and W. Yu, "A multi-band/UWB MIMO/diversity antenna with an enhanced isolation using radial stub loaded resonator," *Applied Computational Electromagnetics Society (ACES) Journal*, vol. 28, no. 1, pp. 8-20, January 2013.

[11] D. Jiang, Y. Xu, R. Xu, and W. Lin, "A compact ultra-wideband antenna with improved triple band-notched characteristics," *Applied Computational Electromagnetics Society (ACES) Journal*, vol. 28, no. 2, pp. 130-136, February 2013.

[12] J. Zhang, H. Yang, and H. Liang, "Band-notched split-ring resonators loaded monopole antenna for ultra-wideband applications," *Applied Computational Electromagnetics Society (ACES) Journal*, vol. 28, no. 2, pp. 137-142, February 2013.

[13] A. Jafargholi, "Compact broadband printed monopole antenna," *Applied Computational Electromagnetics Society (ACES) Journal*, vol. 28, no. 4, pp. 321-326, April 2013.

[14] N. Ojaroudi, M. Ojaroudi, N. Ghadimi, and M. Mehranpour, "UWB square monopole antenna with omni-directional radiation patterns for use in circular cylindrical microwave imaging systems," *Applied Computational Electromagnetics Society (ACES) Journal*, vol. 28, no. 2, pp. 123-129, February 2013.

[15] M. Ojaroudi, N. Ojaroudi, and S. A. Mirhashemi, "Bandwidth enhancement of small square monopole antenna with dual band-notched characteristics using h-ring slot and conductor backed plane for UWB applications," *Applied Computational Electromagnetics Society (ACES) Journal*, vol. 28, no. 1, pp. 64-70, January 2013.

[16] Ansoft High Frequency Structure Simulation (HFSS), Ver. 10, Ansoft Corporation, Pittsburgh, PA, 2005.

[17] "CST microwave studio," ver. 2008, *Computer Simulation Technology*, Framingham, MA, 2008.

[18] C. R. Medeiros, J. R. Costa, and C. A. Fernandes, "Compact tapered slot UWB antenna with WLAN band rejection," *IEEE Antennas and Wireless Propagation Letters*, vol. 8, pp. 661-664, 2009.

Mohammad Akbari was born on February 3, 1983 in Tehran, Iran. He received his B.Sc. degree in Engineering Telecommunication from the University of Shahid Bahonar, Kerman, Iran in 2007 and his M.Sc. degrees in Electrical Engineering Telecommunication from the University of Urmia, Urmia, Iran in 2011. He has taught courses in microwave engineering, antenna theory and fields & waves and electromagnetic at Aeronautical University, Tehran, Iran. He is currently pursuing his Ph.D. degree jointly at Concordia University, Montreal, Canada. His main field of research contains analysis and design of microstrip antennas, modeling of microwave structures, radar systems, electromagnetic theory and analysis of UWB antennas for WBAN applications, antenna interactions with human body, computational electromagnetics (time and frequency-domain methods) and microwave circuits and components. He is the author or co-author of approximately 40 peer-reviewed scientific journals and international conference papers. Akbari was awarded the Graduate Concordia Merit Scholarship.

Reza Movahedinia was born in 1984 in Mashhad, Iran. He received his B.Sc. degree in Power Electrical Engineering from Shahrood University of Science and Technology and his M.Sc. degree in Telecommunication Engineering from Urmia University. From 2014, he is working towards his Ph.D. degree at Concordia University. His research interests include analysis and design of microstrip antennas, design and modeling of microwave structures, reflectarray antenna, radar systems and electromagnetic theory.

Abdel Razik Sebak (F'10) received his B.Sc. degree (with honors) in Electrical Engineering from Cairo University, in 1976 and the B.Sc. degree in Applied Mathematics from Ein Shams University, in 1978. He received his M.Eng. and Ph.D. degrees from the University of Manitoba, in 1982 and 1984, respectively; both in Electrical Engineering. From 1984 to 1986, he was with the Canadian Marconi Company, working on the design of microstrip phased array antennas. From 1987 to 2002, he was a Professor in the Electrical and Computer Engineering Department at the University of Manitoba. He is a Professor of Electrical and Computer Engineering at Concordia University. His current research interests include phased array antennas, computational electromagnetics, integrated antennas, electromagnetic theory, interaction of EM waves with new materials and bioelectromagnetics. Sebak received the 1992 and 2000 University of Manitoba Merit Award for Outstanding Teaching and Research, the 1994 Rh Award for Outstanding Contributions to Scholarship and Research, and the

1996 Faculty of Engineering Superior Academic Performance. He is a Fellow of IEEE. He has served as Chair for the IEEE Canada Awards and Recognition Committee (2000-2004) and the Technical Program Chair of the 2002 IEEE-CCECE and 2006 ANTEM conferences.

Applications of ANN and ANFIS to Predict the Resonant Frequency of L-Shaped Compact Microstrip Antennas

Ahmet Kayabasi [1], Abdurrahim Toktas [2], Ali Akdagli [3], Mustafa B. Bicer [3], and Deniz Ustun [4]

[1] Department of Electronics and Automation
Silifke-Tasucu Vocational School of Selcuk University, Silifke, Mersin, Turkey
ahmetkayabasi@selcuk.edu.tr

[2] Department of Information Technologies
Mersin University, Ciftlikkoy, Yenisehir, 33343, Mersin, Turkey
atoktas@mersin.edu.tr

[3] Department of Electrical–Electronics Engineering
Mersin University, Ciftlikkoy, Yenisehir, 33343, Mersin, Turkey
akdagli@mersin.edu.tr, mbbicer@mersin.edu.tr

[4] Department of Software Engineering
Mersin University, Tarsus, 33400, Mersin, Turkey
denizustun@mersin.edu.tr

Abstract **─** Since the Compact Microstrip Antennas (CMAs) with various shapes are crucial for mobile communication, they take much attention in present days and studies related to analysis and design on them have been increasing day by day. In this work, simple approaches based on Artificial Neural Network (ANN) and Adaptive Neuro-Fuzzy Inference System (ANFIS) for computing the resonant frequency of L-shaped CMAs operating at UHF band have been presented. In order to train and test the ANN and ANFIS models, 192 LCMAs having different physical dimensions and relative dielectric constants were simulated by electromagnetic simulation software named IE3D™, which is based on Method of Moment (MoM). 172 of LCMAs were employed for training, while the remainders were utilized for testing the models. Average Percentage Errors (APEs) for training were obtained as 0.345% and 0.090% for ANN and ANFIS models, respectively. The constructed models were then tested over the test data and APEs values were achieved as 0.537% for ANN and 0.454% for ANFIS. Afterwards, the accuracy and validity of ANN and ANFIS models proposed in this work were verified on measurement data of the fabricated LCMAs. The results indicate that ANN and ANFIS can be successfully used to predict the resonant frequency of LCMAs without necessitating any other sophisticated calculations.

Index Terms **─** Adaptive Neuro-Fuzzy Inference System (ANFIS), Artificial Neural Network (ANN), compact microstrip antenna, L-shaped compact microstrip antenna, resonant frequency.

I. INTRODUCTION

The Microstrip Antennas (MAs) [1-3], thanks to their attractive features, such as low profile, light weight, easy fabrication and conformability to mounting hosts have been rapidly increasing for applications of wireless communication systems; for instance, 2G/3G mobile services, marine or land vehicle navigations (GPS), wireless LANs access and

Submitted On: April 9, 2013
Accepted On: July 14, 2014

remote sensor with monitoring systems. These applications usually require small antennas in order to meet the miniaturization of mobile units. The size of conventional MAs having rectangular, triangular and circular patch shapes, has become large for mobile terminals. Thus, size reduction is becoming major design considerations. Compact MAs (CMAs) are called for a miniaturized version of MAs. For constructing CMAs, various approaches such as method of loading slots on the patch or ground plane, shorting pins and using high permittivity substrate layer have been employed [2]. Several CMA configurations obtained by using the method of slots loading on the patch, such as C shape by [4], E shape by [5], H shape by [6] and L shape by [7] have been proposed in recent years.

In analysis of the conventional MA, the techniques such as cavity model [8] and transmission line model [9] can be used. These techniques may not be used for CMAs because of their irregular shapes. In general, simulation and experimental studies are successfully carried out for the analysis and design of CMAs. Electromagnetic simulation tools employing the computational electromagnetics, such as Finite Difference Time Domain (FDTD) method [10] and Method of Moment (MoM) [11] to solve the complicated Maxwell equations are utilized. However, designing procedure may be complicated and highly time consuming by using these tools.

The latest advancements in wireless communication technology have led to an increase in the usage of CMAs with various shapes; therefore, simple approaches should be utilized to analyze their performances. The resonant frequency is of crucial importance in the CMA design, since these antennas inherently suffer from narrow bandwidth. In the literature, several approaches based on approximate formulas have been proposed for determining the resonant frequency of CMAs with arrow, C, E, H, L and rectangular ring shapes [12-16]. In these formulas, the resonant frequency is calculated by using the resonant length equations together with the edge extension dimension and effective relative dielectric constant expressions derived for the rectangular MA. In general, the formulation methods lead to confusion because of many successive calculations.

This paper attempt to predict the resonant frequency of L shaped CMAs (LCMAs) by using Artificial Neural Network (ANN) [17] and Adaptive Neuro-Fuzzy Inference System (ANFIS) [18], to take the advantage of the fast computation of the ANN and ANFIS with a simple manner. For achieving this goal, 192 of LCMAs having various parameters, such as antenna dimensions and dielectric constants were simulated by the packaged software named IE3D™ (version 14), depended on the MoM. 172 of LCMAs were used for the training phase and the remainders were utilized for the testing phase of the models. The accuracy and validity of the models were also tested and verified on two experimental data.

The ANN attempted to model poorly understood problems by employing a mathematical model based on brain's structure. The brain consists of billions of densely interconnected neurons. The premise behind ANN models is that mimicking the brain's structure of many highly connected processing elements will enable computers to tackle tasks they have not as of yet performed well [17]. The ANFIS is a very powerful approach for constructing complex and nonlinear relationship between a set of input and output data sets and it combines the advantages of the expert knowledge of the Fuzzy Inference Systems (FISs) and the learning capability of ANNs [19]. Optimization of these linguistically expressions in FIS are made by a network and this provides the learning ability with addition to data processing ability of the ANFIS. The ANN and ANFIS have ability to learn, generalization, the smaller information requirement, fast real-time operation and ease of implementation without needing any expert knowledge [20]. Even if training phase takes a few minutes, the test phase takes only a few microseconds. A distinct advantage of both ANN and ANFIS, is that they bypass the repeated use of complex formulations or processes for a new case given to it after proper training. Because of these attractive features, the ANN and ANFIS have often been used to solve problems related to electromagnetics, microwave and different engineering areas [21-33].

II. MODELING OF THE ANN AND ANFIS FOR LCMAs

A. LCMA

As shown in Fig. 1, a LCMA has a slot having *d* dimensions on one corner of a rectangular patch ($L \times W$) on the substrate of height *h* having relative dielectric constant ε_r overall on the ground plane. Slot loading on the rectangular MA results in a decrease of resonant frequency; thus, size reduction for the antenna has been achieved effectively.

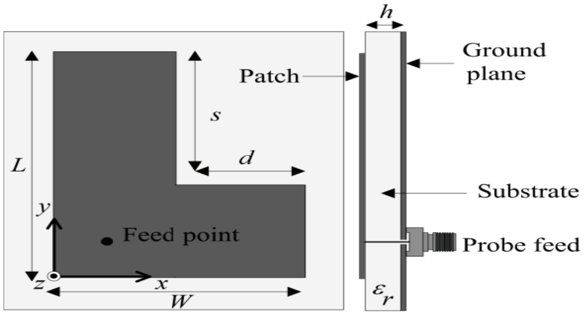

Fig. 1. Geometry of LCMA.

B. Simulations

In order to determine the resonant frequencies of 192 LCMAs having different dimensions and various substrate dielectric constants, which are tabulated in Table 1, simulations have been performed with the use of IE3D™. The antennas operate over the frequency range 0.78-3.23 GHz corresponding to UHF band.

In the simulations, maximum frequency and cell/wavelength rate were assumed as 4 GHz and 40, respectively. A 50 ohm probe feed was applied. Optimization module in IE3D™ based on genetic algorithm [34] was utilized to define the feed point for |S11| < – 10 dB objective function, resulting in the best return loss value.

Table 1: Physical and electrical parameters of simulated LCMAs

Number of Simulations	Patch Dimensions (mm)					
	L	*W*	*s*	*d*	*h*	ε_r
64	30	25	10, 15, 20, 25	4, 8, 12, 16	1.57	2.33, 4.5, 6.15, 9.8
64	40	30	20, 25, 30, 35	5, 10, 15, 20	2.50	2.33, 4.5, 6.15, 9.8
64	50	35	30, 35, 40, 45	6, 12, 18, 24	3.17	2.33, 4.5, 6.15, 9.8

C. Training of the ANN and ANFIS

The ANN and ANFIS have been individually applied to predict the resonant frequency values of LCMAs. 172 of LCMAs are employed for training, while 20 of LCMAs are used for testing the ANN and ANFIS models. As shown in Fig. 2, the physical and electrical parameters (*L*, *W*, *d*, *s*, *h* and ε_r) of the simulated antennas were given as inputs and their respective resonant frequency values of IE3D™ were given as outputs, for training the ANN and ANFIS models.

As shown in Fig. 3, the ANN model based on Multilayer Perceptron (MLP) [17] consisting of 1 hidden layer with 3 neurons, was constructed in this work. "Tangent sigmoid" function was used for input and hidden layers, while "purelin" function was utilized for output layers. The Levenberg–Marquardt (LM) algorithm [35] was used in the ANN model as training algorithm, since it is capable of fast learning and good convergence. The number of epochs, minimum gradient descent, momentum parameter (μ), μ increment, μ decrement, maximum μ and seed value were used for training as 250, 10^{-10}, 0.0001, 4, 0.1, 1010, 1446455104, respectively.

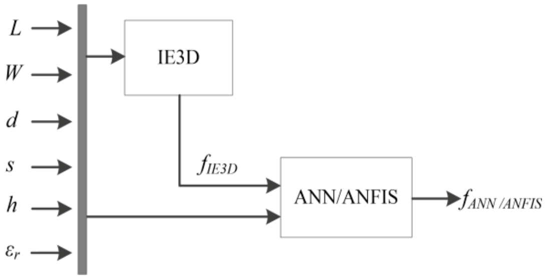

Fig. 2. Training of the ANN and ANFIS.

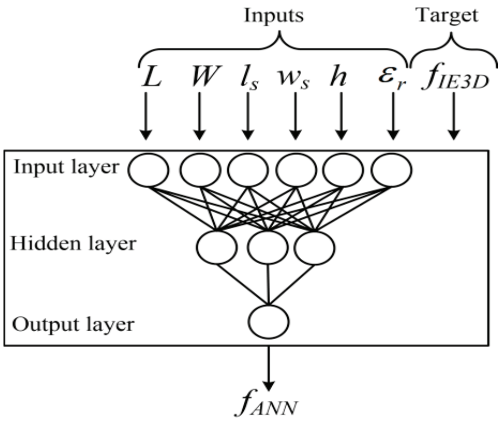

Fig. 3. ANN model.

For the ANFIS network, the hybrid-learning algorithm [18] combining the Least-Squares Method (LSM) and the Backpropagation (BP) [36] algorithm was used. This algorithm converges faster, since it reduces the dimension of the search space of the BP algorithm [37]. The ANFIS network designed in this work was shown in Fig. 4. The number of Membership Functions (MFs) for the input values and output value was selected 22. The number of epochs, range of influence, squash factor, accept ratio and reject ratio used for training were selected as: 100, 0.5, 1.25 0.5 and 0.15, respectively. The MFs used for input values were selected as Gaussian and for the output values was selected as linear functions. The numbers of nodes, linear parameters, nonlinear parameters, total parameters, training data pairs and fuzzy rules are: 317, 154, 264, 418, 172 and 22, respectively.

The training results of the ANN and ANFIS models together with the results of IE3D™ were given in Fig. 5. The method illustrated in Fig. 6 was used for calculating Average Percentage Errors (APEs) and APE values were obtained as 0.345% and 0.090% for the ANN and ANFIS, respectively.

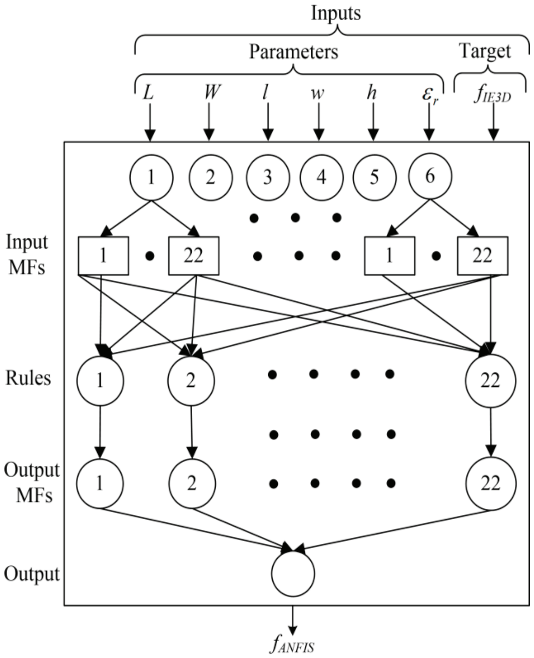

Fig. 4. ANFIS network.

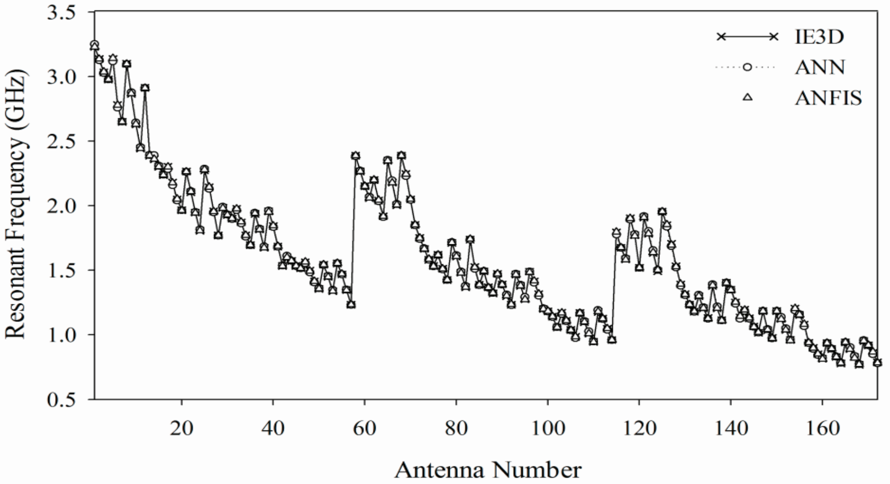

Fig. 5. Comparative results of the simulation, ANN and ANFIS models for training phase.

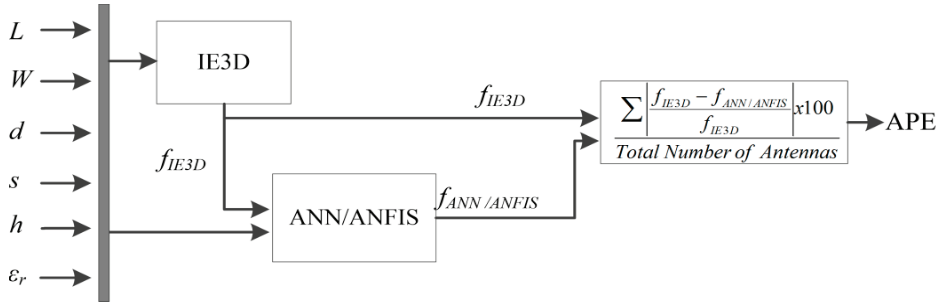

Fig. 6. APE calculation of the ANN and ANFIS.

D. Testing of the ANN and ANFIS

20 of simulated LCMAs representing the whole solution space were utilized to test the performance of the trained ANN and ANFIS models. The simulated and predicted resonant frequency values and calculated APEs with the instruction of Fig. 6, are given in Table 2. APEs were obtained respectively, as 0.537% and 0.454% for the ANN and ANFIS over 20 LCMAs.

Table 2: Resonant frequencies determined by the ANN and ANFIS for test phase

Patch Dimensions (mm)						Resonant Frequencies (GHz)			Percentage Errors (%)	
L	*W*	*s*	*d*	*h*	ε_r	Simulated	ANN	ANFIS	ANN	ANFIS
30	25	15	8	1.57	2.33	2.969	2.959	2.959	0.337	0.337
30	25	25	4	1.57	2.33	3.128	3.125	3.137	0.096	0.288
30	25	25	12	1.57	2.33	2.640	2.650	2.640	0.379	0.000
30	25	10	16	1.57	4.50	2.200	2.216	2.204	0.727	0.182
30	25	10	4	1.57	6.15	2.013	2.031	2.020	0.894	0.348
30	25	20	16	1.57	6.15	1.563	1.556	1.564	0.448	0.064
30	25	20	16	1.57	9.80	1.244	1.246	1.261	0.161	1.367
40	30	25	5	2.50	2.33	2.359	2.345	2.361	0.593	0.085
40	30	30	20	2.50	2.33	1.844	1.837	1.816	0.380	1.518
40	30	25	5	2.50	4.50	1.713	1.716	1.725	0.175	0.701
40	30	35	10	2.50	4.50	1.650	1.647	1.648	0.182	0.121
40	30	20	10	2.50	6.15	1.432	1.423	1.429	0.628	0.209
40	30	30	20	2.50	6.15	1.183	1.189	1.190	0.507	0.592
40	30	20	15	2.50	9.80	1.090	1.093	1.101	0.275	1.009
50	35	30	6	3.17	2.33	1.904	1.944	1.925	2.101	1.103
50	35	35	18	3.17	2.33	1.635	1.618	1.634	1.040	0.061
50	35	35	6	3.17	4.50	1.380	1.376	1.378	0.290	0.145
50	35	40	12	3.17	4.50	1.303	1.305	1.303	0.153	0.000
50	35	35	12	3.17	6.15	1.114	1.110	1.119	0.359	0.449
50	35	45	24	3.17	6.15	0.983	0.993	0.978	1.017	0.509
APE									0.537	0.454

Further to investigate the robustness of the proposed ANN and ANFIS models over measurement data rather than simulation data, a LCMA was also fabricated by using material of Rogers™ RT/duroid 5870. The resonant frequency value of the antenna was measured by Agilent E5071B ENA series RF network analyzer. Figure 7 illustrates the simulated and measured return loss curves of the LCMA. Notice that the measurement result may include discrepancies because of material production, geometry etching and feed connector misalignment in the fabrication process. The measured, simulated and calculated resonant frequency results of the antennas are tabulated in Table 3. Table 3 also contains the measurement results reported by Chen (2000).

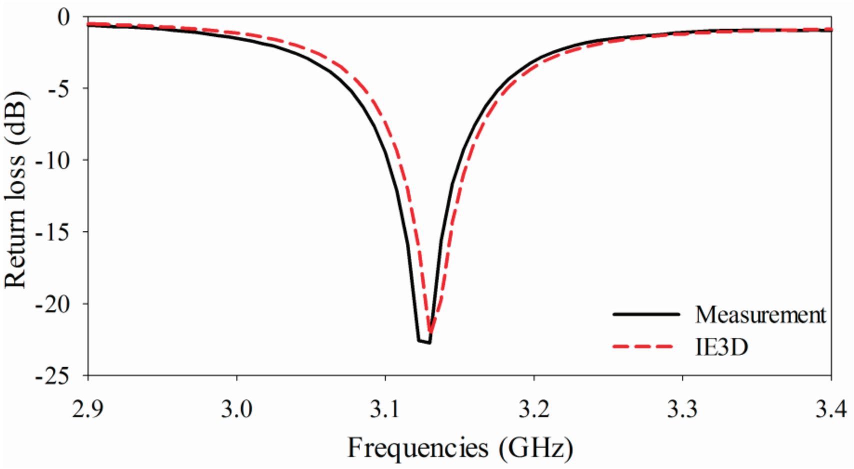

Fig. 7. Return loss (s_{11}) graph of the fabricated LCMA.

Table 3: Results of the simulation, measurement, ANN and ANFIS models

	Patch Dimensions (mm)						Resonant Frequencies (GHz)				Percentage Errors (%)
	L	*W*	*s*	*d*	*h*	ε_r	Measured	ANN	ANFIS	ANN	ANFIS
LCMA *	30	25	10	8	1.57	2.33	3.130	3.121	3.135	0.542	0.096
LCMA [7]	50	45	22	20	8	1.07	2.680	2.738	2.765	0.436	0.545

*Fabricated in this work by using Rogers™ RT/duroid 5870 with $\tan\delta=0.0012$

The simulated radiation patterns for the fabricated LCMA operating at 3.138 GHz are given in Fig. 8 (a) for *x*-*z* plane ($\phi = 0^{\circ}$) and in Fig. 8 (b) for *y*-*z* plane ($\phi = 90^{\circ}$). It is seen that the radiation patterns have good performance and approach omni-directional radiation characteristic.

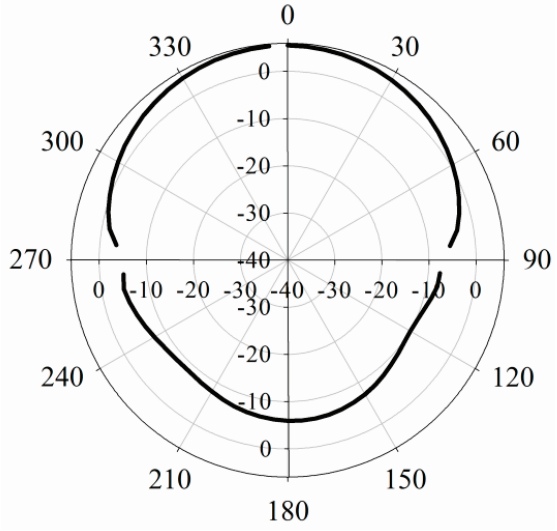

(a)

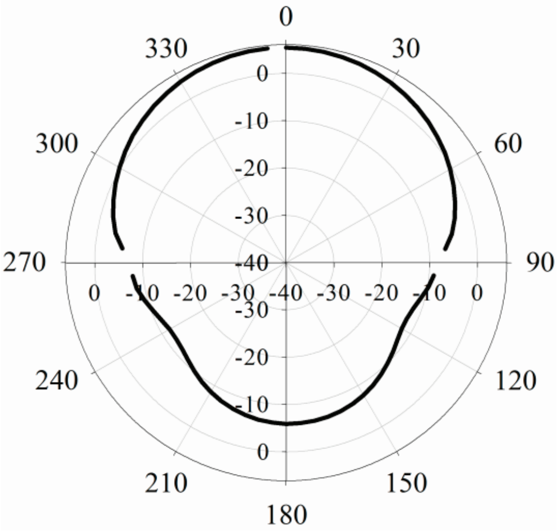

(b)

Fig. 8. The simulated radiation pattern of fabricated antenna at 3.138 GHz: (a) for *x*-*z* plane and (b) for *y*-*z* plane.

The simulated gain plot of the proposed antenna is given in Fig. 9. The peak gain occurs over the resonant frequency of 3.16 GHz with the radiation efficiency exceeding 80%. The gain varies over the 3 dBi for the 3.07-3.24 GHz band. This good radiation efficiency is due to the use of the dielectric material with low tangent loss.

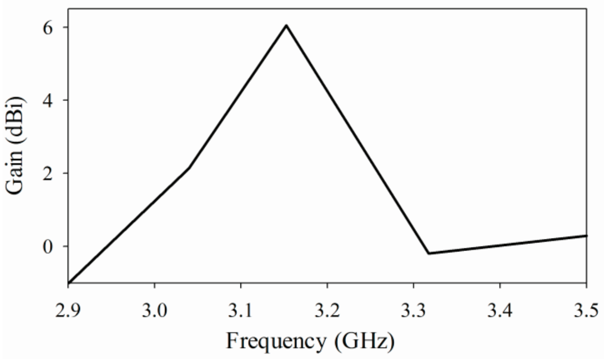

Fig. 9. The simulated gain graph of the fabricated antenna.

From Fig. 5 given for the training phase, the computation results of the ANN and ANFIS well fit to the simulation results of the IE3D™. Test phase results for 20 LCMAs given in Table 2, show that there is a well conformity between the simulated and computed resonant frequencies, in general. In fact, these results are enough to verify the proposed models. However, the experimental data given in Table 3 was also employed to investigate the validity of the models. The very good agreement between the measured values and our computed resonant frequency values supports the validity of the models. These all comparatively results point out that proposed ANN and ANFIS models can be successfully employed to estimate the resonant frequency of the LCMAs operating at UHF band. It is worth noting, that better results may be obtained from the ANN and ANFIS either by choosing different training and test data sets from the ones used in this work, or by supplying more input data set values for training.

III. CONCLUSION

In this study, the ANN and the ANFIS models have been proposed to predict the resonant frequencies of LCMAs. The resonant frequency values were obtained by simulating 192 LCMAs with various antenna dimensions and dielectric constant. It was shown that the computed results by the ANN and ANFIS models trained by means of simulation data are in very good agreement with simulated ones. Accuracy and validity of the proposed ANN and ANFIS models was further tested and verified on two experimental results, of which one was fabricated in this work and the other was reported elsewhere. Thus, the proposed models of ANN and ANFIS can successfully compute the resonant frequency of LCMA operating at UHF band. A major advantage of the ANN and ANFIS computation is that after once accomplished training, no need again any training for each new needs of calculation, since the ANN and ANFIS completely pass the repeated use of complex iterative processes for new cases. The proposed method is not limited to the resonant frequency computation of LCMAs. This method can easily be applied to other antenna and microwave circuit problems. Accurate, fast, and reliable models can be developed from measured/simulated antenna data. Once developed, these models can be used in place of computationally intensive numerical models to speed up antenna design.

REFERENCES

[1] R. Garg, P. Bhartia, I. Bahl, and A. Ittipiboon, "Microstrip antenna design handbook," *Artech House*, Londra, 2001.
[2] K. L. Wong, "Compact and broadband microstrip atennas," *John Wiley & Sons, Inc.*, 2002.
[3] G. Kumar and K. P. Ray, "Broadband microstrip antennas," *Artech House*, USA, 2003.
[4] A. A. Deshmukh and G. Kumar, "Formulation of resonant frequency for compact rectangular microstrip antennas," *Microw. Opt. Techn. Let.*, vol. 49, pp. 498-501, 2007.
[5] F. Yang, X. X. Zhang, X. Ye, and Y. Rahmat-Samii, "Wide-band e-shaped patch antennas for wireless communications," *IEEE Trans. Antennas Propag.*, vol. 49, pp. 1094-1110, 2001.
[6] A. F. Sheta, A. Mohra, and S. F. Mahmoud, "Multi-band operation of a compact h-shaped microstrip antenna," *Microw. Opt. Techn.*, vol. 35, pp. 363-367, 2002.
[7] Z. N. Chen, "Radiation pattern of a probe fed l-shaped plate antenna," *Microw. Opt. Techn. Let.*, vol. 27, pp. 410-413, 2000.
[8] W. F. Richards, Y. T. Lo, and D. D. Harrisson, "An improved theory for microstrip antennas and

applications," *IEEE T. Antenn. Propag.*, vol. 29, pp. 38-46, 1981.

[9] K. Bhattacharyya and R. Garg, "A generalized transmission line model for microstip patches," *IEEE Proc. Microwave Antennas Propag.*, vol. 132, pp. 93-98, 1985.

[10] A. Taflove, "Computational electrodynamics: the finite-difference time domain method," *Artech House*, Boston, 1995.

[11] R. F Harrington, "Field computation by moment methods," *IEEE Press*, Piscataway, NJ, 1993.

[12] M. Paulson, S. O. Kundukulam, C. K Aanandan, and P. Mohanan, "Resonance frequencies of compact microstrip antenna," *Electron. Lett.*, vol. 37, pp. 1151-1153, 2001.

[13] D. K. Neog and R. Devi, "Determination of resonant frequency of slot-loaded rectangular microstrip patch antennas," *Microw. Opt. Techn. Let.*, vol. 52, pp. 446-448, 2010.

[14] A. Akdagli and A. Toktas, "A novel expression in calculating resonant frequency of h-shaped compact microstrip antennas obtained by using artificial bee colony algorithm," *J. Electromagnet. Wave*, vol. 24, pp. 2049-2061, 2010.

[15] A. Toktas, A. Akdagli, M. B. Bicer, and A. Kayabasi, "Simple formulas for calculating resonant frequencies of c and h shaped compact microstrip antennas obtained by using artificial bee colony algorithm," *J. Electromagnet. Wave*, vol. 25, pp. 1718-1729, 2011.

[16] A. Toktas and A. Akdagli, "Computation of resonant frequency of e-shaped compact microstrip antennas," *Journal of the Faculty of Engineering and Architecture of Gazi University*, vol. 27, pp. 847-854, 2012.

[17] S. Haykin, "Neural networks: a comprehensive foundation," *Macmillan College Publishing Company*, New York, A.B.D, 1994.

[18] J. S. R. Jang, "ANFIS: adaptive-network-based fuzzy inference system," *IEEE T. Syst. Man. Cy.*, vol. 23, pp. 665-685, 1993.

[19] K. Guney and N. Sarikaya, "Adaptive neuro-fuzzy inference system for computing the resonant frequency of electrically thin and thick rectangular microstrip antennas," *International Journal of Electronics*, vol. 94, pp. 833-844, 2007.

[20] Y. B. Tian and Z. B. Xie, "Particle-swarm-optimization-based selective neural network ensemble and its application to modeling resonant frequency of microstrip antenna," *Microstrip Antennas, InTech*, 2011.

[21] S. Sagiroglu and K. Guney, "Calculation of resonant frequency for an equilateral triangular microstrip antenna with the use of artificial neural networks," *Microw. Opt. Techn. Let.*, vol. 14, pp. 89-93, 1997.

[22] K. Guney and S. S. Gultekin, "Artificial neural networks for resonant frequency calculation of rectangular microstrip antennas with thin and thick substrates," *Int. J. Infrared Milli.*, vol. 25, pp. 1383-1399, 2004.

[23] H. J. Delgado, "A novel neural network the synthesis of antennas and microwave devices," *IEEE T. Neural Networ.*, vol. 16, pp. 1590-1600, 2005.

[24] E. B. Rahouyi, J. Hinojosa, and J. Garrigós, "Neuro-fuzzy modeling techniques for microwave components," *IEEE Microw. Wirel. Co.*, vol. 16, pp. 72-74, 2006.

[25] J. Hinojosa and G. Doménech-Asensi, "Space-mapped neuro-fuzzy optimization for microwave device modeling," *Microw. Opt. Techn. Let.*, vol. 49, pp. 1328-1334, 2007.

[26] M. Turkmen, S. Kaya, C. Yildiz, and K. Guney, "Adaptive neuro-fuzzy models for conventional coplanar waveguide," *Prog. Electromagn. Res.*, vol. 6, pp. 93-107, 2008.

[27] P. Malathi and R. Kumar, "On the design of multilayer circular microstrip antenna using artificial neural network," *International Journal of Recent Trends in Engineering*, vol. 2, pp. 70-74, 2009.

[28] A. Dadgarnia and A. A. Heidari, "A fast systematic approach for microstrip antenna design and optimization using ANFIS and GA," *J. Electromagnet. Wave*, vol. 24, pp. 2207-2221, 2010.

[29] T. Khan and A. De, "Computation of different parameters of triangular patch microstrip antennas using a common neural model," *International Journal of Microwave and Optical Technology*, vol. 5, no. 4, pp. 219-224, 2010.

[30] A. Kayabasi, M. B. Bicer, A. Akdagli, and A Toktas, "Computing resonant frequency of h-shaped compact microstrip antennas operating at UHF band by using artificial neural networks." *Journal of the Faculty of Engineering and Architecture of Gazi University*, vol. 26, pp. 833-840, 2011.

[31] M. Pandit and T. B. Roy, "Artificial models for determining antenna parameters for a resonant frequency," *International Journal of Current Engineering and Technology*, vol. 3, no. 2, pp. 297-302, 2013.

[32] R. Ghayoula, N. Fadlallah, A. Gharsallah, and M. Rammal, "Design, modelling, and synthesis of radiation pattern of intelligent antenna by artificial neural networks," *Applied Computational Electromagnetics Society (ACES) Journal*, vol. 23, no. 4, pp. 336-344, December

2008.

[33] Y. Xiong, D. G. Fang, and R. S. Chen, "Application of two-dimensional AWE algorithm in training multi-dimensional neural network model," *Applied Computational Electromagnetics Society (ACES) Journal*, vol. 18, no. 2, pp. 64-71, July 2003.

[34] J. H. Holland, "Adaptation in natural and artificial systems," *University of Michigan Press*, Ann Arbor, 1975.

[35] M. T. Hagan and M. Menhaj, "Training feedforward networks with the marquardt algorithm," *IEEE T. Neural Networ.*, vol. 5, pp. 989-993, 1994.

[36] J. S. R. Jang, "Self-learning fuzzy controllers based on temporal backpropagation," *IEEE T. Neural Networ.*, vol. 3, pp. 714-723, 1992.

[37] K. Guney and N. Sarikaya, "Adaptive neuro-fuzzy inference system for computing patch radius of circular microstrip antennas," *Microw. Opt. Techn. Let.*, vol. 48, pp. 1606-1610, 2006.

Ahmet Kayabasi was born in 1980. In 2001, he received his B.S. degree in Electrical and Electronics Engineering from Selcuk University, Turkey. In 2005, he received his M. S. degree in Electrical and Electronics Engineering from Selcuk University, Turkey. Since 2001 he has been working as Lecturer in Electronics and Automation Department of Silifke-Tasucu Vocational School of Selcuk University. Since 2009 he has been studying towards his Ph.D. degree in Electrical and Electronics Engineering from Mersin University. His current research interests include antennas, microstrip antennas, computational electromagnetic, artificial intelligent and applications of optimization algorithms to electromagnetic problem such as radiation, resonance and bandwidth.

Abdurrahim Toktas was born in 1977. He received his B.S. degree in Electrical and Electronics Engineering from Gaziantep University, Turkey in 2002. He worked as Telecom Expert from 2003 to 2010 for Turk Telecom Company, which is the national PSTN and wideband internet operator. He obtained his M. S. and Ph.D. degrees in Electrical and Electronics Engineering from Mersin University, Turkey, in 2010 and 2014, respectively. He has been working in the IT Department at Mersin University. His current research interests include electromagnetics, antennas, MIMO antennas, computational electromagnetic, artificial intelligent, evolutionary optimization algorithms and their applications to electromagnetics, microwave circuits and wireless communication systems.

Ali Akdagli obtained his B.S., M.S. and Ph.D. degrees from Erciyes University, Kayseri, in 1995, 1997 and 2002, respectively; all in Electronic Engineering. From 2003 to 2006 he was an Assistant Professor in the Electronic Engineering department at Erciyes University. He joined the same department at Mersin University, where he currently works as a Professor. He has published more than 90 papers in journals and conference proceedings. His current research interests include evolutionary optimization techniques (genetic algorithm, ant colony optimization, differential evolution, particle swarm optimization and artificial bee colony algorithms), artificial neural networks and their applications to electromagnetic, wireless communication systems, microwave circuits, microstrip antennas and antenna pattern synthesis problems. Akdagli is an editorial board member of "Recent Patents on Electrical Engineering," "International Journal of Computers" and Journal of "Computational Engineering."

Mustafa Berkan Bicer was born in 1988. In 2009, he received his B.S. degree in Electrical and Electronics Engineering from Firat Universiy, Turkey. In 2012, he received M.S. degree in Electrical and Electronics Engineering from Mersin University, Turkey. Since 2009 he has been working as a Research Engineer in the Electrical and Electronics Engineering Department at Mersin University. He has been studying towards his Ph.D. degree in the same department. His current research interests include antennas, microstrip antennas, computational electromagnetic, artificial intelligent and applications of optimization algorithms to electromagnetic problem such as radiation, resonance and bandwidth.

Deniz Ustun was born in 1976. In 2001, he received his B.S. degree in the department of Computer Science Engineering from Istanbul University, Turkey. In 2009, he also received his M.S. degree in Electrical and Electronics Engineering from Mersin University, Turkey. Since 2010, he has been studying towards his Ph.D. degree in the same department. He has been working as Lecturer in the department of Software Engineering at Mersin University for one year. His current research interests are artificial neural network, data mining, algorithms and theory of computation, information systems, artificial intelligent optimization algorithm, computer modeling and simulation (microstrip antennas, computational electromagnetic) and applications of optimization algorithms to electromagnetic problem such as radiation, resonance and bandwidth.

Impact of the Hand on the Specific Absorption Rate in the Head

Ivan B. Bonev, Ondrej Franek and Gert F. Pedersen

Department of Electronic Systems
Antennas, Propagation and Radionetworking Group
Aalborg University, Aalborg 9000, Denmark
ibonev@mail.bg, of@es.aau.dk, gfp@es.aau.dk

***Abstract* ─** In this article, we have investigated the influence of the hand on the Specific Absorption Rate (SAR) in the head for single and dual-antenna mobile terminals. The SAR in the head has been evaluated via Finite Difference Time Domain (FDTD) numerical computations. In the numerical models, the user has been represented not only by using the Specific Anthropometric Mannequin (SAM) head phantom, but also by including a hand phantom. Two types of hand grips (soft and firm) have been used to investigate the impact of the hand on the SAR. Moreover, the influence of the index finger position on the SAR has been investigated by using hand models with different locations of the index finger. At low band, the SAR evaluation in the head without including the hand phantom overestimates the actual value, with the hand phantom presents independently on the type, location and number of antennas. The highest overestimation of 50% has been observed for the mobile terminal with bottom positioned Folded J Antenna (FJA). At the high band and when considering the dual-antenna mobile terminals, the hand increases the SAR in the head by up to 40% compared to the respective calculated values without a hand phantom. Further, the SAR evaluation when the firm hand grip is used can be considered as a worst case estimation, because higher SAR values in the head have been obtained compared to when using the soft phantom.

***Index Terms* ─** Hand phantom, near fields and specific absorption rate.

I. INTRODUCTION

The effect of the electromagnetic radiation from the mobile phone towards the user, has been evaluated through the SAR in the head [1]. However, in the estimation procedure, a hand phantom is not included due to the lack of detailed knowledge on the hand grips up until recently. In a recent study [2], two hand grip models have been identified when the mobile phone is used in talk mode. The SAR is related to the Near Fields (NF) in vicinity of the antenna. Some fundamental results have been outlined in [3]. In [4], the first antenna solution with a reduced SAR in the head has been proposed. The use of a parasitic element connected to the ground plane to manipulate the Near Fields (NF) and consequently the SAR, has been proposed in [5]. In [6], when the SAM phantom has been used, a dual-antenna configuration has been found to have higher SAR in the head than the respective one when single antenna is used.

In this article, we have investigated different antenna configurations having one or two antennas. The types of the antennas have been chosen in a way to represent the most common types used in the mobile phones nowadays. In our study, we have considered four antenna configurations with one antenna and four with two antennas; combining FJA, Planar Inverted F Antenna (PIFA) and Folded Inverted Conformal Antenna (FICA), fitting into a typical candy bar mobile phone. The two main issues, which have been addressed and investigated in the current work, were the contribution of the hand on the SAR value in the head for both single and dual-antenna mobile terminals and the influence of the index finger position on the SAR in the head for both general hand grips in use. A useful conclusion for the future SAR evaluation by using

Submitted On: March 10, 2013
Accepted On: April 24, 2014

an appropriate hand grip has been given.

II. ANTENNA DESIGNS AND USER PHANTOM MODELS

The information for the mobile terminals under investigation is summarized in Table 1.

Table 1: Mobile terminals' antennas used in the investigation

Type	Location	Notation
FJA	Top	H1
FJA	Bottom	H2
PIFA	Top	H3
PIFA	Bottom	H4
PIFA-PIFA	Bottom	H5
PIFA-PIFA	Top	H6
PIFA-PIFA	Top and Bottom	H7
FICA-FICA	Top and Bottom	H8

H1 to H4 are mobile terminals with single antenna, while H5 to H8 are with two antennas. The single antennas have been designed to cover the 900 MHz (low) and 1800 MHz (high) GSM bands. The dual-antenna configurations have covered the LTE (746-796) MHz (low) and (1920 -2170) MHz (high) frequency bands. In order to obtain maximum bandwidth, the trivial position of the planar antennas is the one coinciding with the edges of the ground plane. The dimension of the mobile handset is 40 mm x 100 mm x 10 mm (width x length x thickness). The ground plane and the metallic antenna elements have been modelled as a Perfect Electric Conductor (PEC). All mobile terminals in our analysis have been designed including a battery, which is made of PEC and it may have an important significance on the SAR in the head. Other parts available in the real phones, such as a phone case, are made of dielectric material with low relative permittivity and therefore will not influence drastically the SAR results. Thus, they will not be included in the mobile phone models. A parallel in-house FDTD code [7] developed at Antennas, Propagation and Radio-Networking (APNET) group at Aalborg University, has been used for the investigation. For the termination of the simulation space, the perfectly matched layer absorbing boundaries [8] were used. The profiles of the antenna configurations are shown in Fig. 1.

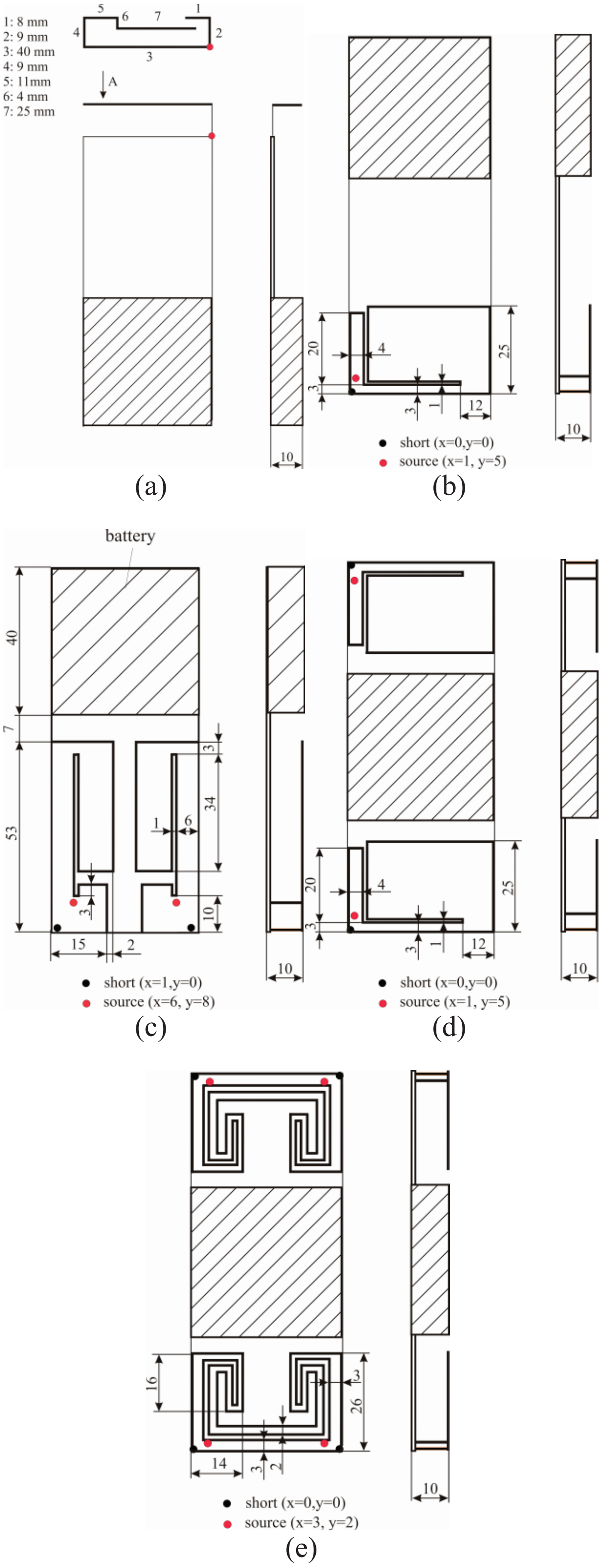

Fig. 1. Profiles of the designed antennas: mobile terminals (a) H1, (b) H3, (c) H5, (d) H7 and (e) H8.

Two hand grips have been identified when the mobile phone is used in talk mode in [2]. Both are shown in Fig. 2. In the case of soft grip style, there is a significant gap between the hand palm and the mobile phone, as opposed to the firm grip where the hand holds the phone tightly. The hand phantoms have been originally created using the 3D software POSER and then converted to “wrl” type of files. Lastly, they have been processed via MATLAB, in order to create the hand phantoms as external objects in our in-house FDTD code. The dimensions of the hands were scaled according to the study in [9] and their electromagnetic properties were chosen according to the investigation in [10]. As a head phantom, we have used the SAM phantom head which has been standardized for SAR evaluation [1]. According to the latter, the mobile phone is placed in “right tilt position” with respect to the SAM head phantom. The hand models with different location of the index finger are shown in Fig. 3.

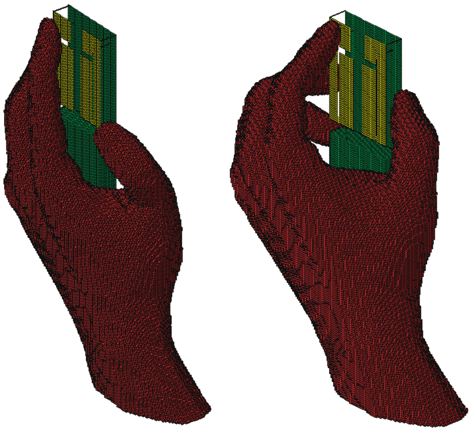
(a) (b)

Fig. 2. (a) Firm and (b) soft hand phantoms.

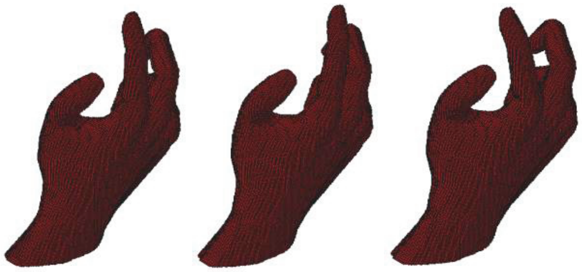
(a) (b) (c)

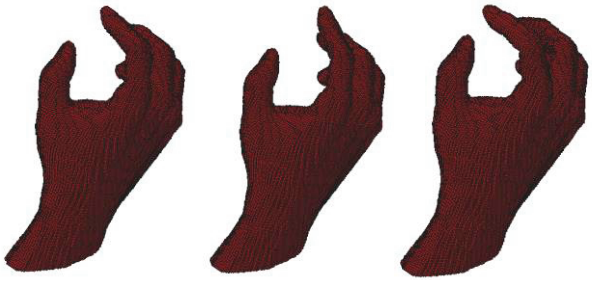
(d) (e) (f)

Fig. 3. Firm hand phantom with the index finger positioned on: (a) “initial,” (b) “right” and (c) “left;” and soft hand having the index finger located on: (d) “initial,” (e) “right” and (f) “left”.

III. RESULTS AND DISCUSSION

The SAR is defined via the equation:

$$\mathrm{SAR} = \frac{\sigma |E|^2}{\rho}, \qquad (1)$$

where σ is the conductivity of the tissue where the computation is made, E is the total electric field within the tissue and ρ is the sample density.

The SAR values averaged in 1 g for all mobile terminals under investigation are shown in Fig. 4.

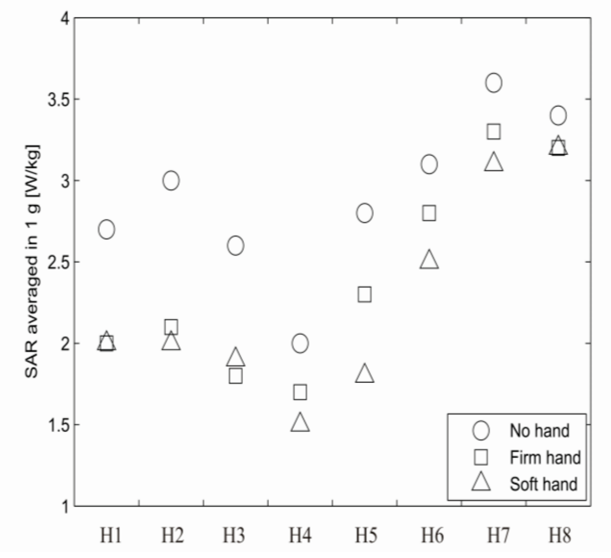

(a)

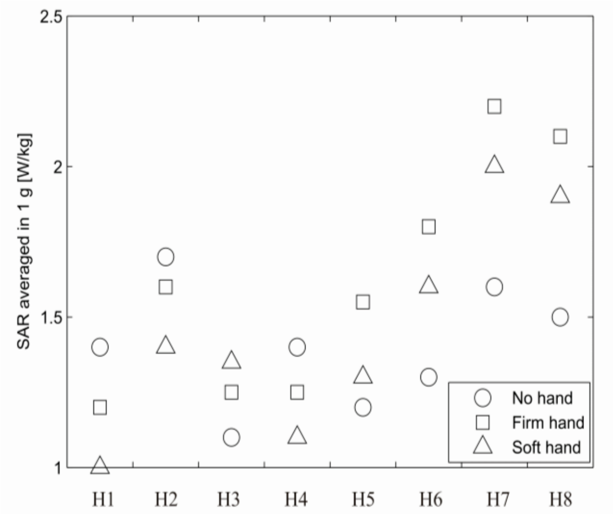

(b)

Fig. 4. SAR averaged in 1 g for: (a) low band and (b) high band, for initial location of the index finger.

At low band, the presence of the hand leads to decrease of the SAR in the head independently on the type, location and number of antennas. In this aspect, according to [1], the current evaluation of the SAR without a hand phantom seems to overestimate the realistic value (when the hand phantom is present). This overestimation can be assumed to be the worst case and therefore the evaluation of the SAR in the head without using a hand phantom can be considered as an acceptable solution. The highest overestimation has been observed in the case of H2 and it is approximately 50%. Comparing the obtained results for H1 and H2, we can easily see that the hand model equalizes the SAR values in the head for both types of mobile phones, as opposed to when it is not present. The PIFA single-antenna mobile terminals have lower SAR values compared to the ones having FJA. The mobile terminal H4 having the radiating element on the bottom of the ground plane has the lowest SAR values.

Following equation (1), the SAR is dependent on the electric field within the head phantom. There is a strict relationship between the electric field and the frequency for a given antenna under consideration. The lower the frequency is, the higher the electric field is. The low band of the LTE technology is lower than the low band of the GSM. The high band of the GSM is lower than the high band of the LTE. Due to these reasons we would expect that at the low band intrinsically, the SAR in the head when the mobile terminal has more than one antenna would be slightly higher than the one with one antenna. H5 and H6 consist of two PIFA on one side of the ground plane. However, in the case of H5, which has two PIFA on the bottom of the ground plane, the SAR in the head is comparatively low. The latter can be explained by lowering of the total peak electric field, because the fields provided by both antennas are out of phase. As expected, when the radiating elements are located on the top side (H6), the SAR in the head is higher than in the case when the elements are on the bottom (H5). However, when the radiating elements are bottom and top located as it is the case of H7 and H8, the SAR in the head has high values. The same trend observed for H1 and H2 is valid for the influence of the hand model on the SAR in the head, when H7 and H8 are used. The hand seems to make the computed SAR values in the head very close to each other for H7 and H8.

However, at the high band, the hand phantom seems to be an importance for SAR evaluation. For all dual-antenna mobile terminals, the averaged increase in the SAR in the head when the hand is included, is more than 25% compared to the respective case without the hand included. Moreover, the SAR in the head when the firm grip style is used is almost always higher (always for all dual-antenna configurations) than the respective case with a soft grip phantom. The differences in the SAR in the head when the hand is present or not, are much higher for the case of dual-antenna mobile terminals than for the single-antenna mobile terminals.

In the next four figures, the SAR values in the head have been calculated for hand phantoms having different locations of the index finger. Soft and firm hand grips having different locations of the index finger (see Fig. 3) needs to be investigated, because the variation of the SAR values can be used to define a generalized hand model for correct and realistic evaluation of the SAR in the head.

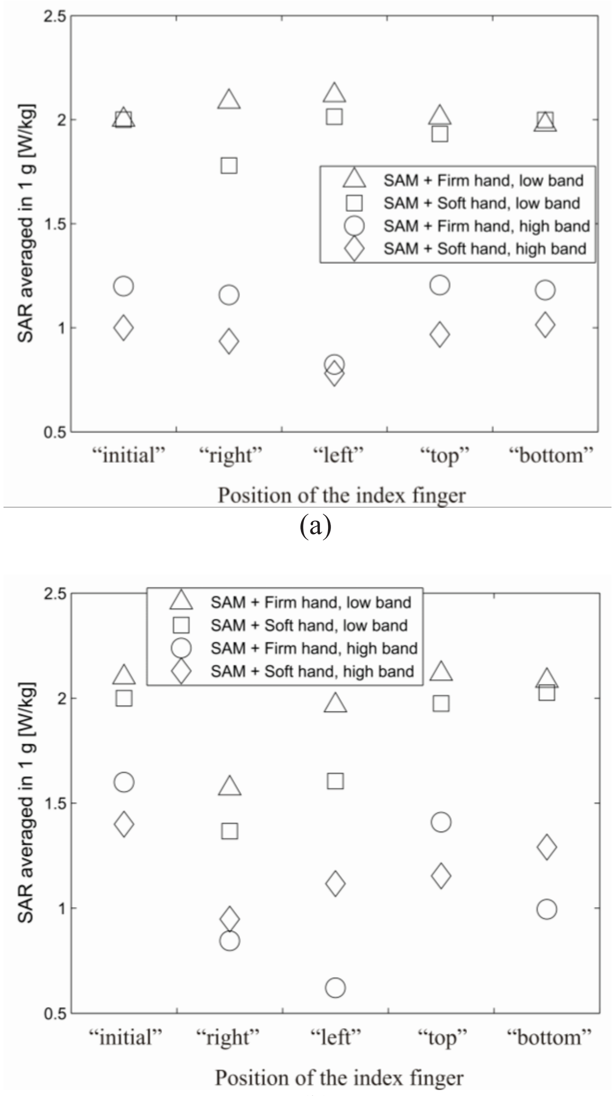

(a)

(b)

Fig. 5. SAR averaged in 1 g in the case of: (a) H1 and (b) H2, for different positions of the index finger.

The hand may influence the SAR in the head significantly depending on the hand grip in use. In the case of H1 at both frequency bands, when moving the index finger in y direction (see Fig. 1), the SAR in the head does not change significantly. The same trend has been observed when using H2 at low band. However, in the case of H2 at high band, when the index finger is on the “top” or “bottom” position, the SAR in the head gets reduced by up to 60%, compared to the one when the index finger is in “initial” position. When the index finger is placed on the “right” or “left” position, the SAR in the head may get decreased drastically, as it is the case of H2 at high band.

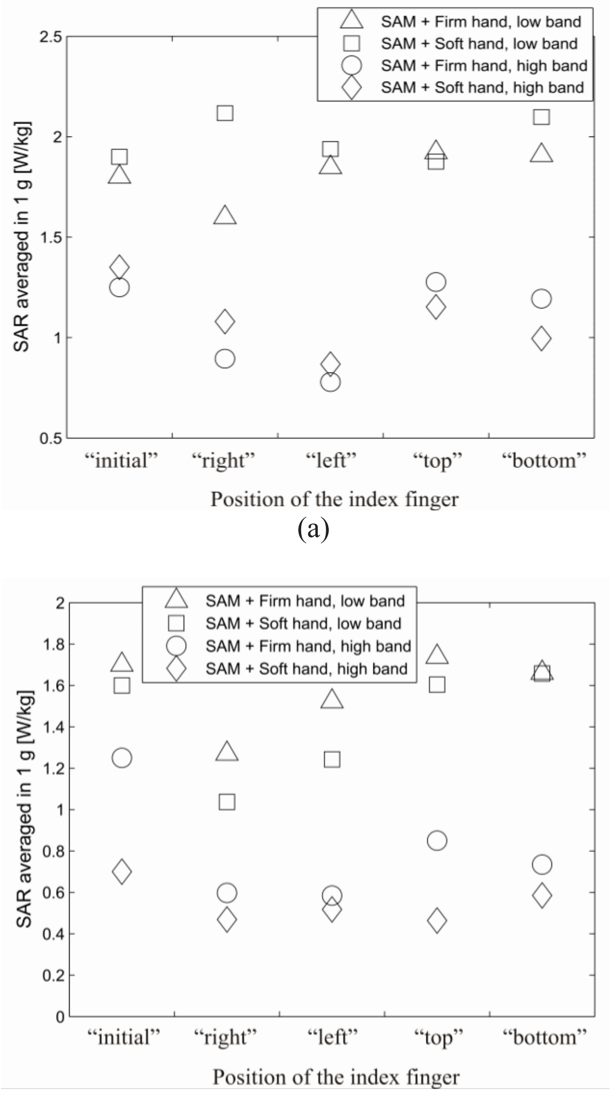

(a)

(b)

Fig. 6. SAR averaged in 1 g in the case of: (a) H3 and (b) H4, for different positions of the index finger.

As it is seen from the SAR results, when using the firm hand phantom in the SAR estimation, the computed SAR values in the head are higher compared to the respective cases with a soft hand phantom. However, the opposite trend has been observed for H3, being a single-antenna mobile terminal having a top positioned PIFA. Further, at the high band, the SAR values in the head when the index finger is positioned on “left” or on “right,” positions are lower than the one obtained for the hand phantoms with initial position of the index finger. For example, when the index finger is positioned on “left,” the SAR in the head is almost two times lower than the one for the case of the initial location of the index finger.

An important general conclusion for the influence of the index finger position on the SAR in the head, can be drawn in the case of single-antenna mobile terminals. The SAR in the head is dependent on whether the index finger is positioned in the region of high electric fields, considering the electric near field antenna pattern in free space. All investigated single-antenna mobile terminals have simplified electric near field pattern in free space. Therefore, when the index finger is positioned in the region of high electric fields, which is the case of the “initial” position of the index finger, the computed SAR in the head is high. When the index finger gets moved further from the region with the high electric fields, the SAR values get decreased. The same trend is not supposed to be observed in the case of the dual-antenna terminals, because of the more complicated total electric near field pattern in free space due to the presence of two antennas and the necessity of addition of their electric near fields.

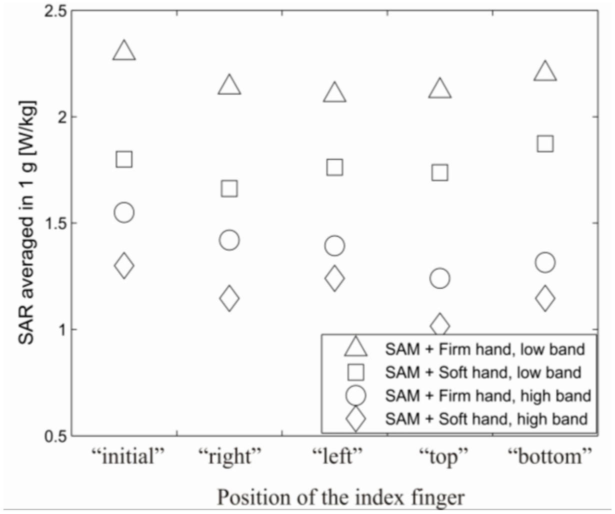

(a)

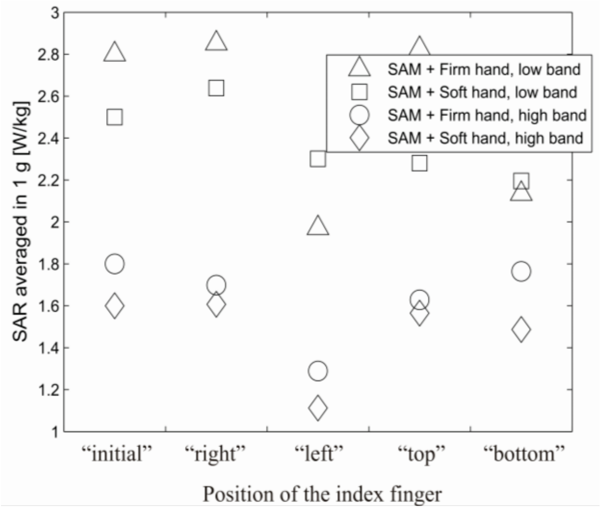

(b)

Fig. 7. SAR averaged in 1 g in the case of: (a) H5 and (b) H6, for different positions of the index finger.

In the case of H5, both PIFA are located on the bottom of the mobile phone. As we would expect, because the index finger is located far from the radiating elements, the variation of the SAR values in the head due to the index finger position is negligible. However, for top positions of the PIFA (H6), the lowest SAR values in the head have been observed for case when the hand grips with index finger in “left” position is used. In general, the SAR values in the head when H6 is used are higher than the respective ones when with H5.

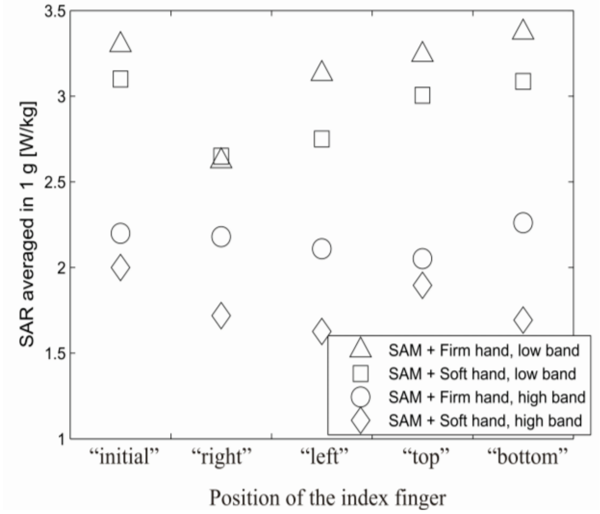

(a)

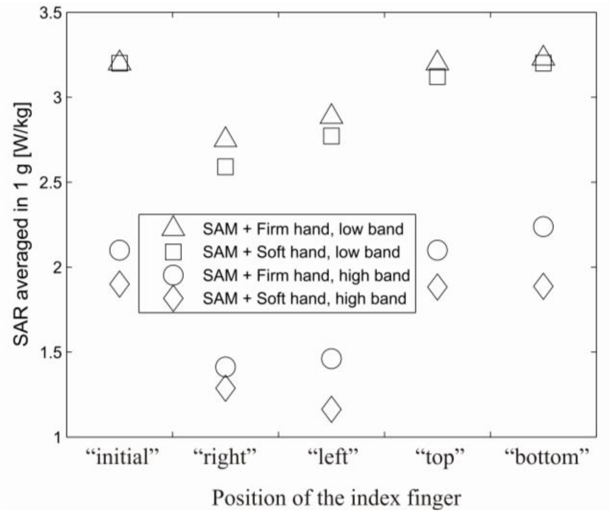

(b)

Fig. 8. SAR averaged in 1 g in the case of: (a) H7 and (b) H8, for different positions of the index finger.

The last two antenna configurations are dual, having top and bottom locations of the radiating elements (H7 and H8). In general, the SAR in the head in the case of H7 and H8 is higher than when H5 and H6 are used. Moreover, when the hand phantoms with the index finger on “right” or “left” position is used, the SAR in the head experiences lower values than the ones with the hand model with the initial location of the index finger. In that aspect, the dependence of the SAR in the head on the index finger position is similar to the trend obtained for the case of single-antenna mobile terminal; i.e., the SAR in the head experiences reduction when the index finger is positioned on “right” or “left”.

In general, the SAR in the head when the firm hand has been used is almost in all cases higher than the respective one with the soft hand in use. Therefore, the antenna exposure to the user considering firm hand in the modelling can be assumed to be the worst case scenario and therefore it should be preferred for SAR evaluation.

IV. CONCLUSION

Two basic hand grips have been used to investigate the influence of the hand on the SAR in the head when using single and dual-antenna mobile terminals. Moreover, hand phantoms with different positions of the index finger for each hand grip have been modelled and included in the investigation. At low band, the way of SAR evaluation in the head without the presence of the hand overestimates the realistic value (when the hand phantom is included); i.e., the hand decreases the SAR in the head independently on the type, location and number of antennas. The highest overestimation has been observed for H2 as it reaches 50%. In the case of dual-antenna mobile terminals and at high band, we have shown that the hand increases the SAR in the head compared to the respective calculated values without a hand phantom. Namely, the increase of the SAR in the head is up to 40% (25% on average) compared to the case without a hand phantom.

Generally, the firm hand grip has been proved to be the hand grip which secures the highest SAR values and therefore it can be considered as a worst case evaluation. Therefore, a test hand phantom similar to the firm grip presented in the current work has to be used to evaluate the SAR in the head for the upcoming LTE technology using more than one antenna in the mobile terminal. Further, the index finger of the hand grip in use should be positioned in a position closed to the “initial” investigated in the current work.

ACKNOWLEDGMENT

The authors thank Dr. Mauro Pelosi for helping with the numerical modelling and for providing the hand phantom models.

REFERENCES

[1] “Human exposure to radio frequency fields from hand-held and body-mounted wireless communication devices-human models, instrumentation and procedures-part 1: procedure to determine the specific absorption rate (SAR) for hand-held devices used in close proximity to the ear (frequency range of 300 MHz to 3 GHz),” 2006.

[2] M. Pelosi, O. Franek, M. Knudsen, M. Christensen and G. F. Pedersen, “A grip study for talk and data modes in mobile phones,” *IEEE Transactions on Antennas and Propagation*, vol. 57, no. 4, pp. 856-865, April 2009.

[3] I. B. Bonev, M. Christensen, O. Franek and G. F. Pedersen, “Impact of the mobile phone dimensions on the hearing aids compatibility,” *Applied Computational Electromagnetics Society Journal*, November 2011.

[4] G. F. Pedersen, “Antennas for small mobile terminals,” Ph.D. thesis, *Aalborg University*, 2003.

[5] I. B. Bonev, O. Franek and G. F. Pedersen, "Parametric study of antenna with parasitic element for improving the hearing aids compatibility of mobile phones and the specific absorption rate in the head," *Progress In Electromagnetics Research Symposium PIERS*, March 2011.

[6] J. O. Mattsson and L. P. De Leon, "SAR evaluation of multi-antenna system," *Antennas and Propagation Society International Symposium*, pp. 1373-1376, 2007.

[7] Y. Wang, I. B. Bonev, J. Nielsen, I. Kovacs and G. F. Pedersen, "Characterization of the indoor multi-antenna body-to-body radio channel," *IEEE Transactions on Antennas and Propagation*, vol. 56, nr. 12, April 2009.

[8] A. Taflove, "Computational electrodynamics: the finite difference time domain method," *Artech House Publishers*, Norwood, MA, 2005.

[9] Greiner, "Hand anthropometry of US army personnel," *Natick/TR-92/011*, 1991.

[10] C. Gabriel, "Tissue equivalent material for hand phantoms," *Phys. Med. Biol.*, PMB-52, pp. 4205-4210, 2007.

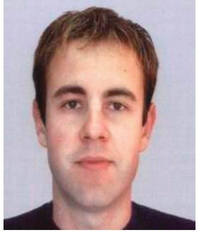

Ivan B. Bonev was born in Yambol, Bulgaria, in April 1980. He received his B.Sc. and M.Sc. degrees (Hons.) in Telecommunications from the Technical University of Varna, Varna, Bulgaria, in 2002 and 2004, respectively; where he also received the M.Sc. degree in Electrical Engineering in 2007. He is currently pursuing his Ph.D. degree in Wireless Communications at Aalborg University, Aalborg, Denmark. He has been a Visiting Researcher at Ecole Politechnique de l'universite de Nantes, Nantes, France; Tampere University of Technology, Tampere, Finland; and Atlantic Cape Community College, Cape May Court House, NJ. In 2007, he joined the Antennas, Propagation and Radio-Networking (APNET) Group at Aalborg University. His current research interests include antennas, theoretical aspects of antenna systems, antenna interactions with a human body, hearing aid compatibility of mobile phones and specific absorption-rate problems. Bonev is a member of the Applied Computational Electromagnetics Society, Sigma Xi, Hearing Loss Association of America, NOVA 100 and Danish Society of Engineers. He is the recipient of the URSI young scientist award in group B "Waves and Fields" for 2011.

Ondrej Franek (S'02-M'05) was born in 1977. He received his M.Sc. (Ing., with honors) and Ph.D. degrees in Electronics and Communication from Brno University of Technology, Czech Republic, in 2001 and 2006, respectively. Currently, he is working at the Department of Electronic Systems, Aalborg University, Denmark, as an Associate Professor. His research interests include computational electromagnetics with a focus on fast and efficient numerical methods, especially the finite-difference time-domain method. He is also involved in research on biological effects of non-ionizing electromagnetic radiation, indoor radiowave propagation and electromagnetic compatibility. Franek was the recipient of the Seventh Annual SIEMENS Award for outstanding scientific publication.

Gert Frølund Pedersen was born in 1965 is married to Henriette and they have 7 children. He received his B.Sc. E. E. degree with honour in Electrical Engineering from the College of Technology in Dublin, Ireland, and his M.Sc. E. E. and Ph.D. degrees from Aalborg University in 1993 and 2003. He has been employed by Aalborg University since 1993, where he is now full Professor heading the Antenna, Propagation and Networking group and is also the head of the doctoral school on wireless communications, which has close to 100 Ph.D. students enrolled. His research has focused on radio communication for mobile terminals, especially small antennas, diversity systems and Propagation and Biological effects. He has published more than 75 peer reviewed papers and holds 20 patents. He has also worked as consultant for developments of more than 100 antennas for mobile terminals, including the first internal antenna for mobile phones in 1994 with lowest SAR, first internal triple-band antenna in 1998 with low SAR and high TRP and TIS, and lately various multi antenna systems rated as the most efficient on the market. He has been one of the pioneers in establishing over-the-air measurement systems. The measurement technique is now well established for mobile terminals with single antennas and he was chairing the COST2100 SWG2.2 group with liaison to 3GPP for over the-air test of MIMO terminals.

Focusing of Electromagnetic Wave from Quartic Inhomogeneous Chiro-Slab

A. Ghaffar [1,4], M. Sharif [2], Q. A. Naqvi [3], M. A. S. Alkanhal [4], F. Khalid [1], and S. Shukurullah [1]

[1] Department of Physics
University of Agriculture, Faisalabad 3800, Pakistan
chabdulghaffar@yahoo.com, shizra_13@yahoo.com, zshukrullah@gmail.com

[2] Department of Physics
GC University, Faisalabad 3800, Pakistan
Msharif_gcuf@yahoo.com

[3] Department of Electronics
Quaid-i-Azam University, Islamabad, Pakistan
nqaisra@yahoo.com

[4] Department of Electrical Engineering
King Saud University, Riyadh, Saudi Arabia
majeed@ksu.edu.sa

Abstract ─ The focusing of electromagnetic waves from a quartic inhomogeneous chiro-slab is examined, using Maslov's method. Analytic field expressions are derived for the transmission coefficients at the interfaces and numerical computations are made to determine the field behavior around the caustic point of the chiro-slab. The effects of chirality parameter, permittivity and permeability on the intensity of the field around caustic point of the chiro-slab are also discussed. The results obtained through this method are shown to be in good agreement with those obtained from Huygens Kirchhoff's integral.

Index Terms ─ Caustic, chiral, Hamilton, intensity and Maslov's method.

I. INTRODUCTION

The discovery of chiral media and metamaterials during the last century has brought together the scientists and researchers from areas as diverse as physics, chemistry and biology [1]. This media offered a range of new millimeter, microwave and optical devices, in the area of electromagnetic and optics. For example, a chiral slab with negative refractive index has been shown to act as a perfect lens having sub-wavelength for circularly polarized waves [2-4]. Many other applications of the chiral metamaterials include but not limited to waveguides, antennas, polarization rotators and cloaking surfaces [5-14].

Two distinct properties of chiral media are the optical activity and circular dichroism. The irregular molecule arrangement enable the chiral material to rotate the plane of polarization of incident wave by an amount proportional to the width of the medium transverse relative to the wavelength of the wave. Moreover, the attenuation of the right-hand and left-hand circularly polarized wave is shown to be strongly affected by the chirality parameter of the medium [15,16]. Chiral scatterers are quite different from their dielectric or conducting counterparts, in that, the former produce both the co-polarized and cross-polarized scattered fields. The circular dichroism property of chiral media on the other hand, gives rise to different absorptivity of the right and left-circularly polarized waves inside a chiral medium.

Submitted On: January 26, 2013
Accepted On: March 8, 2014

In electromagnetics, to study the scattering and propagation, different numerical and analytical methods are available. Asymptotic Ray Theory (ART) is a simple and powerful tool for the evaluation of high frequency fields [17-19]. It is widely used to provide and explain the behavior of electromagnetic fields in both homogeneous and inhomogeneous media, but the field in caustics and shadow boundary has to be treated as a separate problem because ART shows singularities at these points. Kirchhoff integral is usually employed to calculate the fields at these points. There is a more convenient method based on Maslov's theory. Maslov's asymptotic theory is based on an idea that combines both the simplicity of ART and generality of Fourier transform. This method has been used by many authors [20-22] to find out the field behavior in the focal region of different geometries.

In this paper, we have treated a quartic inhomogeneous chiro slab to study the behavior of electromagnetic waves around caustic point using Maslov's method. We are extending our previous work from focusing of dielectric inhomogeneous slab and quadratic inhomogeneous slab composed of chiral medium to inhomogeneous chiral uniform thickness slab with quartic dependent permittivity on one transversal Cartesian coordinate using this technique [16,20]. We have determined the transmission coefficient of electromagnetic waves by an inhomogeneous quartic chiro slab for normal incident analytically. The numerical computations have been made to study the behavior of transmitted electromagnetic field from a quartic inhomogeneous slab composed of chiral medium.

II. FORMULATION

Consider an inhomogeneous chiral planar slab of uniform thickness d and placed in a dielectric medium as shown in Fig. 1. The dielectric medium is described by the constitutive parameters (μ_1,ε_1), whereas chiral medium filling the slab is described by the constitutive parameters (μ,ε,γ). It is assumed that inhomogeneity chiral medium slab is incorporated through permittivity parameter of the chiral medium. It is also assumed that distribution of permittivity is described by a fourth order polynomial equation (hereafter termed as quartic distribution) as given below[20]:

$$\varepsilon(x) = \varepsilon_c[1 - bx^2 - c(x^2)^2], \tag{1}$$

where ε_c is permittivity of corresponding homogeneous material, parameters b and c are associated with focal length of the chiro slab.

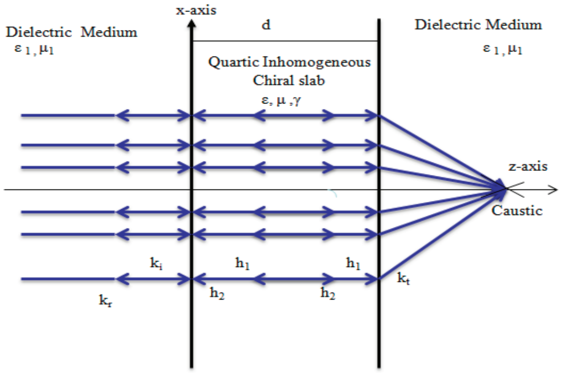

Fig. 1. Quartic inhomogeneous chiral slab.

The electromagnetic field in the chiral medium filling the slab region is described by [2-4]:

$$\boldsymbol{D} = \varepsilon\boldsymbol{E} + j\gamma\boldsymbol{B}, \tag{2}$$

$$\boldsymbol{H} = j\gamma\boldsymbol{E} + \frac{1}{\mu}\boldsymbol{B}, \tag{3}$$

where ε and μ are the permittivity permeability of chiral medium and γ is the chirality parameter, which describes electromagnetic coupling. Two wave numbers h_1 and h_2 for eigenwaves propagating inside the chiral medium are:

$$h_1 = \frac{k}{1+k\,\gamma}, \tag{4}$$

$$h_2 = \frac{k}{1-k\gamma}, \tag{5}$$

with $k = \omega\sqrt{\mu_0\epsilon_0}$. A set up of Cartesian coordinate system with unit vectors $\boldsymbol{a}_x$, $\boldsymbol{a}_y$ and $\boldsymbol{a}_z$ are introduced here to explain the problem of transmission through quartic inhomogeneous chiro slab. In the region $z \le 0$, the incident plane electromagnetic wave is written as [16]:

$$\boldsymbol{E}_i = E_i\boldsymbol{a}_x\, e^{ik_iz}, \tag{6}$$

$$\boldsymbol{H}_r = \eta_1^{-1}E_r\boldsymbol{a}_y\, e^{ik_iz}. \tag{7}$$

The unknown reflected electromagnetic fields can be written as:

$$\boldsymbol{E}_r = E_r\boldsymbol{a}_x\, e^{-ik_iz}, \tag{8}$$

$$\boldsymbol{H}_r = -\eta_1^{-1}E_r\boldsymbol{a}_y\, e^{-ik_iz}. \tag{9}$$

The four electromagnetic waves are propagating inside the inhomogeneous chiro slab ($0 \le z \le d$), two propagating towards interface located at $z = d$ and the other two waves are propagating towards the interface $z = 0$, as shown in Fig. 1. The expressions for electromagnetic waves propagating towards the interface $z = d$ are represented as:

$$\boldsymbol{E}_{0c}^{+} = E_{01}^{+}\left(\boldsymbol{a}_x + i\boldsymbol{a}_y\right)e^{ih_1 z} + E_{02}^{+}\left(\boldsymbol{a}_x - i\boldsymbol{a}_y\right) e^{ih_2 z}, \tag{10}$$

$$\boldsymbol{H}_{0c}^{+} = -iZ^{-1}E_{01}^{+}\left(\boldsymbol{a}_x + i\boldsymbol{a}_y\right)e^{ih_1 z} + iZ^{-1}E_{02}^{+}\left(\boldsymbol{a}_x - i\boldsymbol{a}_y\right) e^{ih_2 z}. \tag{11}$$

The electromagnetic fields of the two waves propagating towards the interface $z = 0$ are represented as:

$$\boldsymbol{H}_{0c}^{-} = iZ^{-1}E_{01}^{+}\left(\boldsymbol{a}_x - i\boldsymbol{a}_y\right)e^{-ih_1 z} - iZ^{-1}E_{02}^{+}\left(\boldsymbol{a}_x + i\boldsymbol{a}_y\right) e^{-ih_2 z}, \tag{12}$$

$$\boldsymbol{E}_{0c}^{-} = -E_{01}^{-}\left(\boldsymbol{a}_x - i\boldsymbol{a}_y\right)e^{-ih_1 z} - E_{02}^{-}\left(\boldsymbol{a}_x + i\boldsymbol{a}_y\right) e^{-ih_2 z}, \tag{13}$$

where E_{01}^{+}, E_{02}^{+}, E_{01}^{-} and E_{02}^{-} are the amplitudes of the unknown coefficients. Z is wave impedance in the region $z \geq d$, the transmitted electromagnetic field in terms of unknown coefficient is written as:

$$\boldsymbol{E}_{0t} = E_t \boldsymbol{a}_x e^{ik_t z}, \tag{14}$$

$$\boldsymbol{H}_{0t} = \eta_1^{-1} E_t \boldsymbol{a}_y e^{ik_t z}, \tag{15}$$

where $k_t = k_i$. In above equations, unknown coefficients can be determined using the boundary conditions. The boundary conditions for the electromagnetic fields at interfaces $z = 0$ and $z = d$ are [4,15]:

$$(\boldsymbol{E_i} + \boldsymbol{E_r}) \times \boldsymbol{a}_z = (\boldsymbol{E}_c^{+} + \boldsymbol{E}_c^{-}) \times \boldsymbol{a}_z, \tag{16}$$

$$(\boldsymbol{H_i} + \boldsymbol{H_r}) \times \boldsymbol{a}_z = (\boldsymbol{H}_c^{+} + \boldsymbol{H}_c^{-}) \times \boldsymbol{a}_z, \tag{17}$$

$$(\boldsymbol{E}_c^{+} + \boldsymbol{E}_c^{-}) \times \boldsymbol{a}_z = \boldsymbol{E_t} \times \boldsymbol{a}_z, \tag{18}$$

$$(\boldsymbol{H}_c^{+} + \boldsymbol{H}_c^{-}) \times \boldsymbol{a}_z = \boldsymbol{H_t} \times \boldsymbol{a}_z, \tag{19}$$

application of above boundary conditions yield the following equations:

$$E_{01}^{+} + E_{02}^{+} - E_{01}^{-} - E_{02}^{-} - E_r = E_i, \tag{20}$$

$$E_{01}^{+} - E_{02}^{+} + E_{01}^{-} - E_{02}^{-} = 0, \tag{21}$$

$$E_{01}^{+} - E_{02}^{+} - E_{01}^{-} + E_{02}^{+} = 0, \tag{22}$$

$$gE_{01}^{+} + gE_{02}^{+} + gE_{01}^{-} + gE_{02}^{+} + E_r = E_i, \tag{23}$$

$$E_{01}^{+}e^{ih_1 d} + E_{02}^{+}e^{ih_2 d} - E_{01}^{-}e^{-ih_1 d} - E_{02}^{-}e^{-ih_2 d} - E_t e^{ik_i d} = 0, \tag{24}$$

$$E_{01}^{+}e^{ih_1 d} - E_{02}^{+}e^{ih_2 d} + E_{01}^{-}e^{-ih_1 d} - E_{02}^{-}e^{-ih_2 d} = 0, \tag{25}$$

$$E_{01}^{+}e^{ih_1 d} - E_{02}^{+}e^{ih_2 d} - E_{01}^{-}e^{-ih_1 d} + E_{02}^{+}e^{-ih_2 d} = 0, \tag{26}$$

$$gE_{01}^{+}e^{ih_1 d} + gE_{02}^{+}e^{ih_2 d} + gE_{01}^{-}e^{-ih_1 d} + gE_{02}^{+}e^{-ih_2 d} - E_t\, e^{ik_i d} = 0. \tag{27}$$

By solving set of equations (20-27), we obtain reflection and transmission coefficients. We consider transmission at the rear face of chiro slab, so transmission coefficient at this interface is given by [4]:

$$E_t = E_i \frac{2\mathrm{g}}{(1-\mathrm{g})^2} \frac{\mathrm{e}^{\mathrm{i}d(h_1-k_i)}+\mathrm{e}^{\mathrm{i}d(h_2-k_i)}}{[(1+\mathrm{g})/(1-\mathrm{g})]^2-\mathrm{e}^{\mathrm{i}d(h_1+h_2)}}, \tag{28}$$

where $\mathrm{g} = \sqrt{(\mu_1/\epsilon_1)\gamma^2 + (\epsilon\mu_1/\mu\epsilon_1)}$.

A. Solution of Hamilton's equations

The solution of Hamilton's equations for the inhomogeneous medium described by equation (1) are given as [20]:

$$\left.\begin{aligned} x &= \xi[(1+v)cos3\psi] \\ z &= \mathrm{p_z}\tau \\ p_x &= -\beta\xi[(1+v)sin\psi - 3vsin3\psi] \\ p_z &= \sqrt{\varepsilon - {p_x}^2} \end{aligned}\right\}, \tag{29}$$

where τ is the parameter along the ray length and $\mathrm{v} = \frac{\mathrm{c}'\mathrm{b}'^2\xi^2}{4}$, $\mathrm{b}' = \lambda\mathrm{b}$ and $\mathrm{c}' = \mathrm{kc}$.

The Cartesian coordinates of refraction point at the rear face (ξ_1, η_1) and the components of associated wave vector are given by:

$$\left.\begin{aligned} \xi_1 &= \xi[(1+v)cos\psi_1 - vcos3\psi_1] \\ \zeta_1 &= d \\ p_{x0} &= -\beta\xi[(1+v)sin\psi_1 - 3vsin3\psi_1] \\ p_{z0} &= \sqrt{\varepsilon_c(1 - b^2\xi^2 + cb^4\xi^4)} \\ p_{z0}\tau_1 &= d, \qquad \psi_1 = \beta\tau_1 \end{aligned}\right\}, \tag{30}$$

where τ_1 is the arc length of the ray for $0 < z < d$. In above equations (ξ, η) are the Cartesian coordinates of refraction point of front face of the chiro slab. The coordinate of the ray after passing through the slab, there is $z > d$, are given by[18]:

$$x = \xi_1 + p_{x1}\,\tau,$$
$$z = \zeta_1 + p_{z1}\,\tau,$$
$$p_{x1} = -\beta\xi[(1+v)sin\psi_1 - 3vsin3\psi_1],$$
$$p_{z1} = \sqrt{1 - \beta^2\,\xi^2\,[(1+v)sin\psi_1 - 3vsin3\psi_1]^2}.$$

B. Focused field at caustic point

The geometrical optics solution is given by [20]:

$$\mathbf{E_t}(\mathrm{x}, \mathrm{z}) = \mathbf{E}_{0\mathrm{t}}[\mathrm{J}(\tau)]^{-\frac{1}{2}}\exp\left[-\mathrm{jk}\left(\psi_0 + \tau\right)\right], \tag{31}$$

where $\mathrm{J}(\tau)$ is Jacobean and ψ_0 is the value of initial phase difference between front and rear faces of the chiro slab, which is given by [20]:

$$\psi_0 = \epsilon_c\left(1 - \frac{\beta^2\xi^2}{2}\right)\tau_1 - \frac{\beta\xi^2}{4}\sin2)\,\psi_1.$$

Geometrical optics field contains singularity at the focal point. Our interest is to find the uniform field expression valid in focal region using Maslov's method. The uniform expression which is valid in the focal region is given by [20,21]:

$$\mathbf{E}(\mathrm{r}) = \sqrt{\frac{\mathrm{k}}{i2\pi}}\int_{-\infty}^{\infty}\boldsymbol{E}_{0t}\left[\frac{1}{\mathrm{D}(0)}\frac{\partial(\mathrm{p}_{\mathrm{x1}},\mathrm{z})}{\partial(\xi,\mathrm{t})}\right]^{-\frac{1}{2}}\times$$
$$\exp\left[-ik\,\psi_1(\mathrm{p}_{\mathrm{x1}},\mathrm{z})\right]\mathrm{dp}_{\mathrm{x1}} \qquad (32)$$

Quantities in the square brackets and phase function $\psi_1(\mathrm{p}_{\mathrm{x1}},\mathrm{z})$ are obtained by the procedure given in [20] and variable of integration are changed from wave vector domain to the ray domain. The field intensity expression in component form may be expressed as:

$$\mathrm{E}_{\mathrm{x}} = \sqrt{\frac{\mathrm{k}}{2\pi i}}\int_0^{\mathrm{d}}\sqrt{\mathrm{S}}\,\mathrm{E}_{\mathrm{t}}\,e^{-ik\psi_1(\mathrm{p}_{\mathrm{x1}},\mathrm{z})}\mathrm{d}\xi, \qquad (33)$$

$$\mathrm{E}_{\mathrm{z}} = \sqrt{\frac{\mathrm{k}}{2\pi i}}\int_0^{\mathrm{d}}\Gamma\sqrt{\mathrm{S}}\,\mathrm{E}_{\mathrm{t}}\,e^{-ik\psi_1(\mathrm{p}_{\mathrm{x1}},\mathrm{z})}\mathrm{d}\xi. \qquad (34)$$

The amplitude and phase function in simplified form can be written as:

$$\mathrm{S} = S_1 S_2$$
$$S_1 = \frac{\beta^4\mathrm{d}\xi^2}{\mathrm{P}_{\mathrm{z}_0}^3}S_3 + \beta\left(9\mathrm{v}\sin 3\psi_1 - (1+3\mathrm{v})\sin\psi_1\right),$$
$$S_2 = \frac{\beta^3\mathrm{d}\xi^2}{\mathrm{P}_{\mathrm{z}_0}^3}S_4 + (1+3\mathrm{v})\cos\psi_1 - 3\mathrm{v}\cos 3\psi_1,$$
$$S_3 = \left(2\mathrm{c}\xi^2 - 1 - \mathrm{v}\right)\cos\psi_1 - 9\mathrm{v}\cos 3\psi_1,$$
$$S_4 = \left(\left(2\mathrm{cb}^2\xi^2 - 1 - \mathrm{v}\right)\sin\psi_1 - 3\mathrm{v}\sin 3\psi_1\right),$$
$$\Gamma = \tan\left(\frac{\mathrm{d}(\mathrm{h}_2 - \mathrm{h}_{1)}}{2}\right).$$

The phase function is given as:

$$\psi_1(\mathrm{p}_{\mathrm{x1}},\mathrm{z}) = \psi_1' + \mathrm{Y}(\mathrm{z}-\mathrm{d}) - \epsilon_{\mathrm{c}}\mathrm{vb}^2\xi^2\ \psi_0',$$
$$\psi_0' = \tau_1 - \frac{\sin 4\psi_1}{4\beta},$$
$$\psi_1' = \psi_0 + \epsilon_{\mathrm{c}}\mathrm{cb}^4\xi^4\psi_2' + \beta\xi^2\left(\vartheta\ \cos\psi_1 + \psi_3'\right),$$
$$\psi_2' = \frac{3}{8}\tau_1 + \frac{2}{16\beta}\sin 2\psi_1 + \frac{1}{32\beta}\sin 4\psi_1,$$
$$\psi_3' = \mathrm{v}\cos 3\psi_1\ \sin\psi_1 - 3\mathrm{v}\sin 3\psi_1\ \cos\psi_1,$$
$$\mathrm{Y} = \sqrt{1 - \beta^2\xi^2\left(\vartheta\sin\psi_1 - 6\mathrm{v}\ \sin\psi_1\sin 3\psi_1\right)^2},$$
$$\vartheta = (1+2\mathrm{v})\ \sin\psi_1.$$

III. HUYGENS KIRCHHOFF'S INTEGRAL

To check the accuracy of the results obtained in the Caustic region of quartic inhomogeneous chiro slab, we compare the computational results obtained by Kirchhoff's approximation. Using Green's theorem, we may show that transmitted field from quartic inhomogeneous chiro-slab is obtained by [16]:

$$\boldsymbol{E}_{\boldsymbol{t}}(x,z) = \int_0^d \boldsymbol{E}_{\mathbf{0}\boldsymbol{t}}\sqrt{\frac{2}{\pi k\tau}}\,e^{-ik\left(\Psi_0+\tau-\frac{\pi}{4}\right)}d\xi, \qquad (35)$$

where $\tau = p_x(x-\xi) + p_z(z-d)$ and $\boldsymbol{E}_{0t}$ is defined in above section 4.

The field intensity expression in component form may be expressed as:

$$\mathrm{E}_{\mathrm{x}} = \sqrt{\frac{\mathrm{k}}{2\pi i}}\int_0^{\mathrm{d}}\frac{\mathrm{E}_{\mathrm{t}}}{\sqrt{\tau}}\,e^{-ik\Phi}d\xi, \qquad (36)$$

$$\mathrm{E}_{\mathrm{z}} = \sqrt{\frac{\mathrm{k}}{2\pi i}}\int_0^{\mathrm{d}}\frac{\mathrm{E}_{\mathrm{t}}}{\sqrt{\tau}}\Gamma e^{-ik\Phi}d\xi, \qquad (37)$$

$$\Phi = \psi_0 + \beta\,\xi^2\,sin\,\psi_1\,cos\,\psi_1 + \beta r\xi\,sin\,\psi_1 +$$
$$(z-d)\ \sqrt{1-\beta^2\,\xi^2\,sin^2\,\psi_1}\ -\frac{\pi}{4}. \qquad (38)$$

IV. RESULTS AND DISCUSSIONS

In this paper, we have solved equations (34), (35), (37) and (38) numerically to study the focusing behavior of quartic inhomogeneous chiro slab. The effect of chirality γ, permittivity ε and permeability μ on transmitted fields are observed by varying these parameters. The thickness of the slab is taken as $d = 0.7$, wave number is assumed as $k = 1000$, $b = 0.3$, $c = 0.1$ and $\beta = 0.3$ in this work. To check accuracy of our high frequency field expressions, we compare the results obtained using Maslov's method (solid line) and Huygens-Kirchhoff's integral (dashed line), which are in good agreement. These results are shown in Fig. 2.

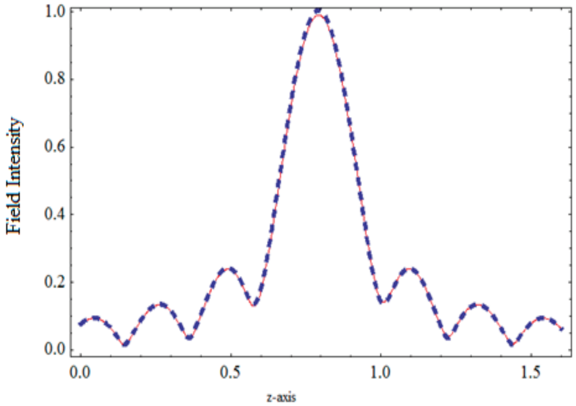

Fig. 2. Comparison of normalized field intensity of chiro slab around focal point along the z-axis using Maslov's method (solid line) and Huygens-Kirchhoff's integral (dashed line).

Figures 3 and 4 represent the comparison of responses for the case of normalized field intensity distribution around the focal region along the z-axis and x-axis, respectively, with the variation of chirality parameters. These comparisons show that the field intensity shifts to a smaller value as we decrease the chirality and vice versa. Figures 5 and

6 represent the comparison of normalized field intensity distribution around the focal region along the z-axis and x-axis, respectively, with the variation of permittivity. These comparisons show that the field intensity shifts to a smaller value as we increase the permittivity and vice versa. Figures 7 and 8 represent the comparison of normalized field intensity distribution around the focal region along the z-axis and x-axis, respectively, with the variation of permeability of chiral medium. These comparisons show that the field intensity shifts to a smaller value as we decrease the permeability and vice versa. A slab of such chiral medium may be used as a perfect lens, which provide sub wavelength resolution for circularly polarized waves.

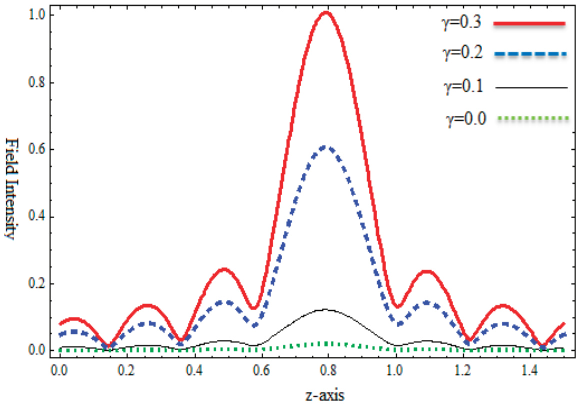

Fig. 3. Comparison of normalized intensity of slab around focal point along z-axis with w.r.t. values of chirality parameter.

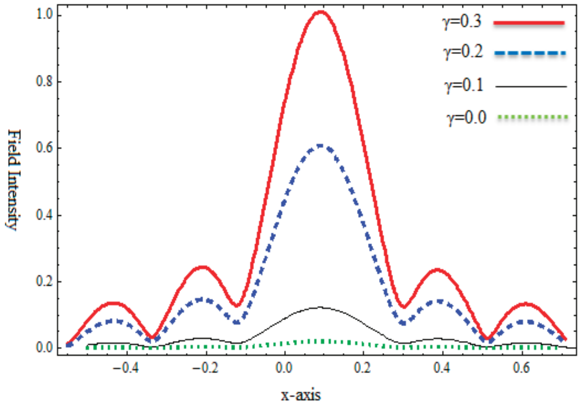

Fig. 4. Comparison of normalized intensity of slab around focal point along x-axis with w.r.t. values of chirality parameter.

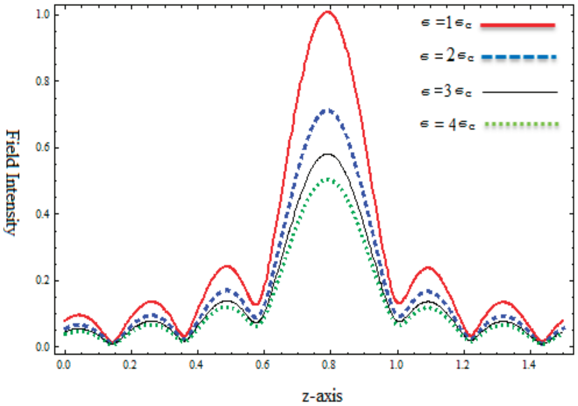

Fig. 5. Comparison of normalized intensity of slab around focal point along z-axis with w.r.t. values of permittivity.

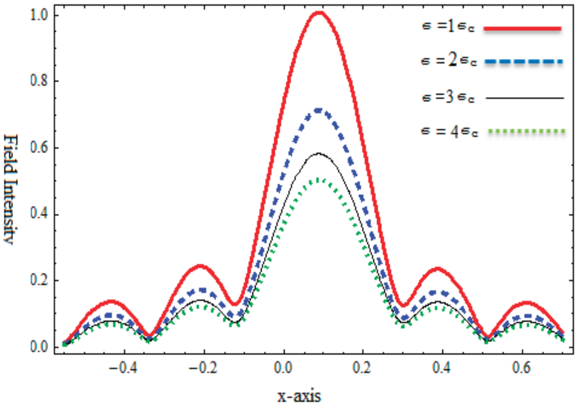

Fig. 6. Comparison of normalized intensity of slab around focal point along x-axis with w.r.t. values of permittivity.

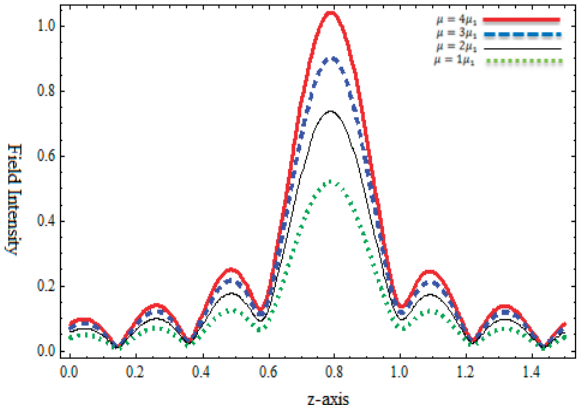

Fig. 7. Comparison of normalized intensity of slab around focal point along z-axis with w.r.t. values of permeability.

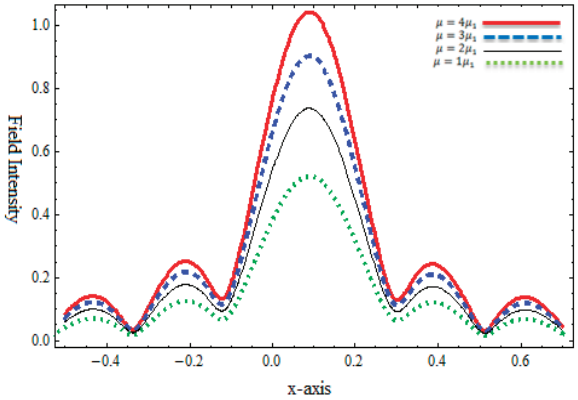

Fig. 8. Comparison of normalized intensity of slab around focal point along x-axis with w.r.t. values of permeability.

V. CONCLUSION

In this study, transmission of electromagnetic waves from a quartic inhomogeneous chiro slab is analyzed. We have used Maslov's method to calculate the field expressions for refracted field from the quartic inhomogeneous chiro slab. The effects of slab's parameters, i.e., chirality, permittivity and permeability on the amplitude of transmitted field in caustic region are shown and discussed. From the plots, we have observed that the field intensity in the caustic region of a quartic inhomogeneous chiral slab decreases by decreasing the chirality parameter. The results presented here will be helpful for potential applications in novel waveguide devices such as directional couplers, cloaking and polarization transformer.

ACKNOWLEDGMENT

Authors would like to thank Research Center, College of Engineering, Deanship of Scientific Research and King Saud University.

REFERENCES

[1] N. Engheta and D. L. Jaggard, "Electromagnetic chirality and its applications," *IEEE Antennas and Propag. Society Newsletter*, vol. 30, pp. 6-12, 1988.

[2] A. Lakhtakia, "Beltrami fields in chiral media," *World Scientific Series in Contemporary Chemical Physics*, 1994.

[3] J. Lekner, "Properties of a chiral slab waveguide," *Pure Applied Optics*, vol. 6, pp. 373-384, 1997.

[4] S. Bassiri, C. H. Papas, and N. Engheta, "Electromagnetic wave propagation through a dielectric-chiral interface and through a chiral slab," *J. Opt. Soc. Am. A.*, vol. 5, pp. 1450-1459, 1988.

[5] J. B. Pendry, "Negative refraction makes a perfect lens," *Phys. Rev. Lett.*, vol. 85, pp. 39-66, 2000.

[6] Y. Jin and S. He, "Focusing by a slab of chiral medium," *Optics Express*, vol. 30, pp. 49-74, 2005.

[7] A. Ghaffar, S. I. Ahmad, R. Fazal, S. Shukrullah, and Q. A. Naqvi, "Scattering of electromagnetic wave by perfect electromagnetic conductor (PEMC) sphere placed in chiral media," *Optik-Int. J. of Light and Electron Optics*, vol. 125, pp. 1589-1597, 2013.

[8] J. F. Dong and J. Li, "The reflection and transmission of electromagnetic waves by a uniaxial chiral slab," *Progress In Electromagnetic Research*, vol. 127, pp. 389-404, 2012.

[9] A. Ghaffar, M. Arif, Q. A. Naqvi, and M. Alkanhal, "Radiation properties of a uniaxial chiral quadratic inhomogeneous slab under oblique incidence," *Optik-Int. J. of Light and Electron Optics*, vol. 124, pp. 4947-4951, 2013.

[10] A. Ghaffar, "Focusing by a cylindrical plano convex lens of chiral medium," *J. Electromag. Wave Appli.*, vol. 25, pp. 833-844, 2011.

[11] A. K. Hamid, "Scattering by chiral lossy metamaterial elliptic cylinders," *Applied Computational Electromagnetics Society (ACES) Journal*, vol. 27, pp. 603-609, 2012.

[12] N. L. Tsitsas, "Analysis of electromagnetic wave propagation in frequency bands of nonlinear metamaterials," *Applied Computational Electromagnetics Society (ACES) Journal*, vol. 27, pp. 169-180, 2012.

[13] A. M. Attiya, "Coupled mode analysis of two-dimensional chiral grating," *Applied Computational Electromagnetics Society (ACES) Journal*, vol. 26, pp. 303-311, 2011.

[14] S. T. Imeci, F. Altunkilic, J. R. Mautz, and E. Arvas, "Transmission through an arbitrarily shaped aperture in a conducting plane separating air and a chiral medium," *Applied Computational Electromagnetics Society (ACES) Journal*, vol. 25, pp. 587-599, 2010.

[15] B. N. Khatir, M. Al-Kanhal, and A. Sebak, "Electromagnetic wave scattering by elliptic chiral cylinder," *J. Electromag. Wave Applic.*, vol. 20, pp. 1377-1390, 2006.

[16] A. Ghaffar, H. M. Shahbaz, and Q. A. Naqvi, "Analysis of electromagnetic field transmitted by a quadratic inhomogeneous slab composed of chiral medium," *Int. J. of Applied Electromagnetics and Mechanics*, vol. 42, pp. 613-622, 2013.

[17] V. P. Maslov, "Thtorie des perturbations et mtthodes asymptotiques," *Dunod*, Paris, France, 1972.

[18] V. P. Maslov, “Perturbations theory and asymptotiques method, *Moskov. Gos. Univ.*, Moscow, 1965.

[19] R. W. Ziolkowski and G. A. Deshamps, “Asymptotic evaluation of high frequency field near a caustic: an introduction to maslov’s method,” *Radio Sci.*, vol. 19, pp. 1001-1025, 1984.

[20] A. Ghaffar Hussain, Q. A. Naqvi, and K. Hongo, “Radiation characteristics of an inhomogeneous slab using maslov’s method,” *J. Electromag. Wave Applic.*, vol. 22, pp. 301-312, 2008.

[21] A. Ghaffar, S. Ahmed, and Q. A. Naqvi, “Electromagnetic field in the caustic region of a spherical reflector under oblique incidence using maslov’s method,” *Int. J. of Applied Electromagnetics and Mechanics*, vol. 38, pp. 1-17, 2012.

[22] A. Ghaffar, M. Shoaib, N. Mehmood, M. Y. Naz, M. Azam, and Q. A. Naqvi, “Electromagnetic field diffraction of a paraboloidal mirror under oblique incidence,” *Int. J. of Applied Electromagnetics and Mechanics*, vol. 41, pp. 579-494, 2013.

Abdul Ghaffar was born in Mitha Tiwana district Khushab Pakistan, Punjab (Pakistan) on January 1, 1976. He received his M.Sc. (Physics) degree from Uninversity of Punjab in 2001. He received his Ph.D. degree from Quaid-i-Azam University, Islamabad, Pakistan in 2009. He is Assistant Professor at Agriculture University, Faisalabad (Pakistan). Currently he is working towards his research at King Saud University, Saudi Arabia. His research interests are chiral media, high frequency electromagnetic scattering from slabs and antennas. He has published over 35 papers in international journals. He has successfully supervised more than 10 M.Sc. and 15 M. Phil students after his Ph.D.

M. Sharif was born in Vehari Pkistan. He received his Ph.D. degree from Quaid-i-Azam in 2007. He is an Assistant Professor at GCUF. His research intrest is scattering Plasm structure.

Qaisar Abbas Naqvi was born in the village of District Narowal (Pakistan). He received his M.Sc., M.Phil and Ph.D. degrees from Quaid-i-Azam University, Islamabad (Pakistan). He has published over one hundred and fifty (150) papers in international journals. He’s also author of a book and chapters in different books. He has successfully supervised eight Ph.D.’s and more than 80 M.Phil students after his Ph.D. in 1998. His research inetersts are Kobyashi potential, Maslov’s method, GTD, fractional electromagnetics, buried cylinders, waveguides, slits, strips, antennas and numerical electromagnetics.

Majeed A. S. Alkanhal obtained his B.Sc. and M.Sc. degrees in Electrical Engineering from King Saud University (Saudi Arabia) in 1984 and 1986, respectively. He received his Ph.D. degree in Electrical Engineering from Syracuse University, Syracuse, New York in 1994. Alkanhal is currently a Full Professor in the Electrical Engineering Department at King Saud University. His research interests include RF and microwave/millimeter-wave communications and radar systems, electromagnetic scattering from complex bodies and material objects, antenna design and optimization for communication and radar systems, application of modern estimation and optimization techniques to signal processing and digital communications problems, numerical solutions to electromagnetics and electronic/optical device problems.

Farayal Khalid was born in Faisalabad (Pakistan). She received her B.S. (honour) from GC Faisalabad and M.Phil degree in Physics from University of Agriculture Faisalabad in 2012. Her current research interest include high frequency techniques used electromagnetic.

Shazia Shukurullah was born in Faisalabad. She received her M.Sc. degree from the University of Punjab. She is currently a Ph.D student. Her research intrests are numerical techniques in electromagnetics and Nano technology**.**

Comparison and Analyzing of Propagation Models with Respect to Material, Environmental and Wave Properties

M. B. Tabakcioglu [1], D. Ayberkin [2], and A. Cansiz [3]

[1] Department of Electrical and Electronics Engineering
Bayburt University, Bayburt 69000, Turkey
mbtabakcioglu@bayburt.edu.tr

[2] Department of Computer Programming
Bayburt University, Bayburt 69000, Turkey
doruk@bayburt.edu.tr

[3] Department of Electrical Engineering
Istanbul Technical University, Istanbul 34469, Turkey
acansiz@itu.edu.tr

Abstract **─** This paper presents a study on a class of algorithms based on Uniform Theory of Diffraction (UTD) for multiple diffractions. Within this context Slope UTD with Convex Hull (S-UTD-CH) model based on Slope UTD and Fresnel zone concept was reviewed. S-UTD-CH model can be used for fast and more accurate field prediction for multiple diffractions in transition zone. An extensive simulation results for comparison of UTD based algorithms with respect to the computation time and accuracy was provided. Furthermore, the study shows how relative permittivity constant, conductivity and inner angle of wedge and polarization type affect the relative path loss.

Index Terms **─** Convex hull, Fresnel zone, material properties, multiple wedge diffraction, radio propagation, slope diffraction and Uniform Theory of Diffraction (UTD).

I. INTRODUCTION

In order to construct more reliable and efficient digital communication networks and broadcasting systems, accurate and time efficient theoretical models being capable of generating field predictions are necessary. Along with the literature, many models have been proposed to meet required demand of accuracy. Propagation models have traditionally treated irregularities in the terrain as knife edge, wedge or cylinder for UHF. For example, while mountains and hills can be modeled as wedge, buildings can be modeled as knife-edge.

Multiple diffraction problems have widely been investigated for a long time; UTD based and numerical solutions have been proposed to predict the field strength in the urban, rural, suburban and indoor environments. In asymptotic high-frequency electromagnetic wave propagation methods, the total electric field at a receiving point is the sum of the field associated with all the rays that reach this point. These reached rays can be direct, reflected, refracted or diffracted rays [1, 2].

Although, previously proposed UTD method by [3] is time efficient method, it fails to predict the field strength accurately when, even if one obstacle is placed in the transition zone of the frontal obstacle. UTD method is high frequency asymptotic method used in electromagnetic wave propagation [4]. A more accurate solution is called S-UTD, has been proposed by [5, 6] by including slope diffraction terms to predict the field strength accurately. In S-UTD method, it is claimed that the phase continuity should be ensured in calculating the distance parameters appearing in the amplitude and the slope diffraction coefficients. S-UTD method gives acceptable

Submitted On: March 25, 2013
Accepted On: July 14, 2014

results when compared with [7]. Vogler's method is based on numerical solution of Fresnel–like integrals and it is known to be ultimate in accuracy. However, S-UTD method still exhibits an error when number of diffraction increases. Although, S-UTD method has shown to deal with multiple transition diffraction problems, its validity has been reported to be limited in the number of diffractions. It is reported in various studies [8-10] that after a total of 10 diffractions, S-UTD method loses the accuracy, causing unreliable and inefficient digital communication networks and broadcasting systems.

Relative path loss is a measure of the average RF attenuation experienced by a transmitted signal when it arrives at the receiver, after traversing a path of several wavelengths [11]. In other words, relative path loss is a path loss divided by free space loss. In order to overcome the path loss problem, a UTD based method called as the Slope UTD with Convex Hull (S-UTD-CH) is proposed in [9, 10]. S-UTD-CH method combines S-UTD and Convex Hull methods. Convex hull method reduces the diffracting wedges and then Slope UTD algorithm runs. By reducing wedge number, computation time is reduced. UTD based solutions are known with small computation time in urban radio propagation modeling, with respect to numerical methods. There is a trade-off between computation time and accuracy. Methods having higher accuracy require large computation time as in numerical methods [7, 12-15]. These methods seem to be infeasible in many cases. In this paper, the UTD based model proposed in [9, 10] is reviewed. The simulation results for comparison of UTD solutions are presented and discussed. Hard polarization is considered in simulations. Accuracy of predicted relative path loss and computation time is compared in UTD models. Moreover, how material properties like wedge angle, conductivity and relative permittivity constant of wedge affects the path loss is analyzed.

II. SLOPE UTD WITH CONVEX HULL METHOD

S-UTD-CH method combines S-UTD and Convex Hull methods. Convex hull method uses the Fresnel zone concept [16]. Fresnel zone concept is not new and has widely been used in UTD based radio propagation modeling in urban/suburban, rural and indoor applications. Fresnel zones are ellipsoid of revolution about the direct line from a transmitter to a receiving end, with the transmitter and receiving ends serving as foci of the ellipse, as shown in Fig. 1.

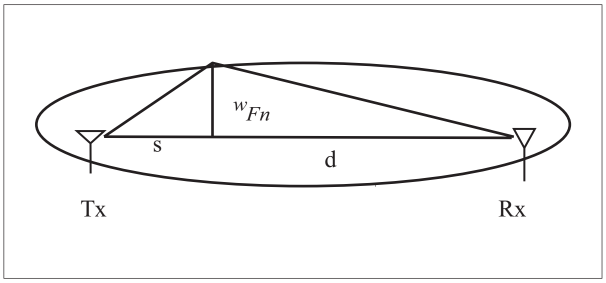

Fig. 1. Fresnel zone configuration.

In this figure, w_{Fn} is radius of Fresnel zone at a given distance given by:

$$w_{F_n} = \sqrt{\frac{\lambda s d}{s+d}}, \tag{1}$$

where λ is wavelength of the incoming wave. s and d is distance from transmitter and receiver. Fresnel zone radius is the maximum at the midpoint between the transmitter and receiver. Although, the obstacles which are placed outside the first Fresnel zone may introduce reflected, diffracted or scattered contributions to the total field strength, they cause only a small distortion in the original wave and can mostly be ignored [9, 10].

In order to reduce the computation complexity of diffraction problem, convex hull model is introduced [16]. By means of convex hull model, unsuccessive diffracting obstacles are excluded from the scenery. Convex hull is described as a polygon formed by some selected wedges between the transmitter and receiver positions [12].

S-UTD-CH based on Fresnel zone concept along with S-UTD, provides an improvement to S-UTD implementation both for computation time and accuracy when the number of the diffracting obstacles is greater than 10. S-UTD-CH model compared numerical model proposed in [13] and relatively small computation time obtained [9, 17]. The detailed sequence of S-UTD-CH algorithm is given in reference [9-10].

According to this sequence for a given height distribution, the main Fresnel zone is constructed between the transmitter and the receiver and the obstacles outside the main Fresnel Zone are eliminated. Following, the secondary Fresnel zones are constructed between the transmitter and the highest obstacle and then the highest obstacle and the receiver. The obstacles outside these secondary Fresnel zones are eliminated. The process is repeated successively for smaller Fresnel zone to be constructed under the secondary Fresnel zones until no obstacles are remained for elimination. In this way, the convex hull is constructed by the obstacles remained as a results of the elimination process. From the theoretical point of view, the diffraction from the obstacle placed outside the first Fresnel zone does not contribute much to the received field and can be ignored for most cases. After forming the convex hull, 2D ray tracing algorithm is run to find all the rays originated from the transmitter to the receiver point. Finally, S-UTD algorithm runs for calculating the total field at the receiver. For the wedge case, the process is illustrated in Fig. 2.

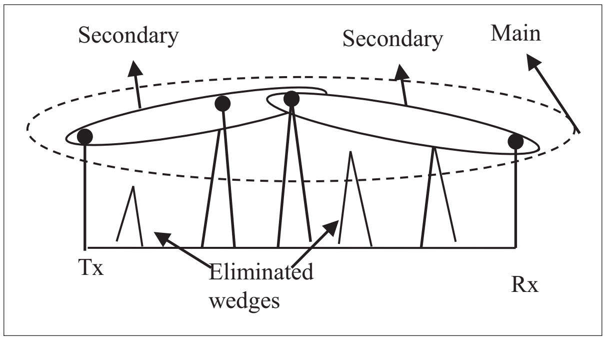

Fig. 2. Construction of the convex hull.

The motivation for the above approach of eliminating less important obstacles, which are outside of the Fresnel zones, is to reduce both computation time and make a compromise between computation time and error when the number of diffractions is large.

When the wedges outside Fresnel zone can be determined and eliminated before running slope UTD, the computation time can be substantially reduced with minimum error. Eliminating one obstacle approximately decreases the computational time by one-fifth and the lesser obstacles are in the Fresnel zone, means lesser computational time.

III. COMPARISON OF MODELS

In order to investigate the ray theoretical methods, simulation results are compared in this section. Computer configuration is as followed. Processor is Intel (R) Core (TM) 2 Quad CPU Q8300 2.5 GHz and RAM is 3GB. Within this context, to compare the UTD, S-UTD and S-UTD-CH methods, following test case is considered for GSM with hard polarization. The transmitter height is taken as 60 m, the operational frequency as 900 MHz and receiver height changes between 0 and 120 m. There is 25 km between transmitting and receiving antennas. There are 4 hills as wedges with 30º inner angle. At 6, 12, 16 and 22 km there are four wedges of 65, 70, 65 and 30 m heights, respectively. Relative permittivity of constant of the hills is taken as 15 and conductivity of the hills as 0.0012 S/m. Relative path losses of the three methods for the considered terrain profile are given in Fig. 3.

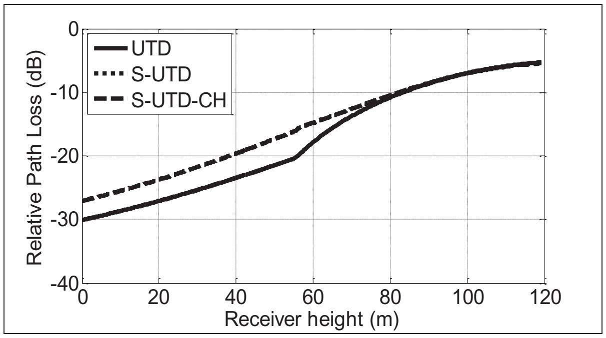

Fig. 3. Comparison of the results for hard polarization.

This figure illustrates relative path losses of the methods for given scenario. Solid line presents UTD method. Dotted and dashed lines show S-UTD and S-UTD-CH methods. As can be seen from Fig. 3, S-UTD and S-UTD-CH gives almost same results. However, UTD model gives relatively higher error, resulted from wedges that are in the transition zone of the previous wedges. As illustrated in Fig. 3, there is 5 dB errors in prediction of field strength. Table 1 shows the computation time for the ray theoretical methods. As can be seen from Table 1, UTD is the fastest method with lower accuracy (5 dB error). S-UTD-CH model is a faster method than S-UTD method, with almost the same accuracy.

Table 1: Computation time for the simulation

UTD (s)	S-UTD (s)	S-UTD-CH (s)
8.3	73.7	59.4

Material properties like conductivity and relative permittivity constant and inner angle of wedges, affect the relative path loss at the receiver. To validate this fact, a simple test case is considered. In the considered case, the inner angle of wedge is 160° with a height of 50 m, placed at 5 km of a propagation path of 10 km, at an operational frequency of 100 MHz. The transmitter height is 50 m, while the receiver height changes from -100 to 200 m. Figure 4 shows the analysis of the relative permittivity constant of the wedge with varying cases. As can be seen from this figure, relative path loss decreases with increasing of relative permittivity constant.

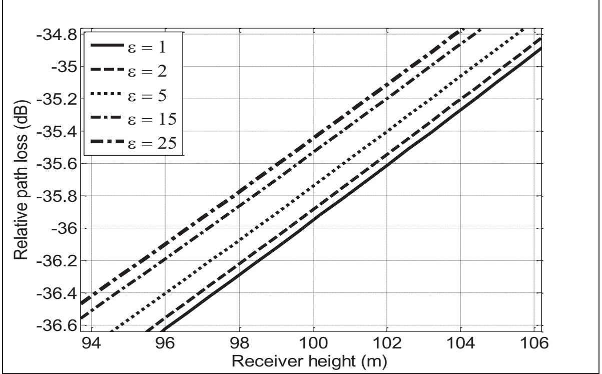

Fig. 4. Analysis of the relative permittivity constant of the wedge.

Figure 5 shows the effect of inner angle of the wedge on relative path loss. As it is illustrated in the figure, relative path loss decreases with increasing the inner angle. When the inner angle tends to zero, it gives the same results with the knife-edge case.

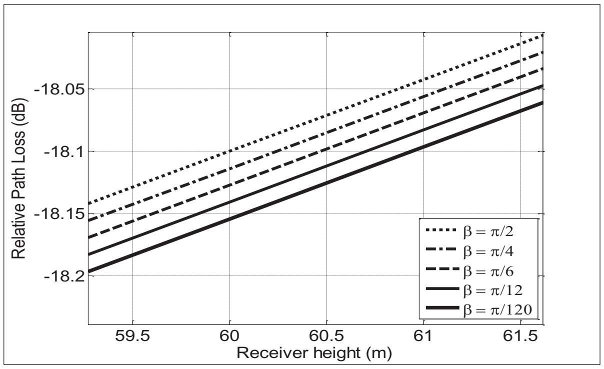

Fig. 5. Analysis of the inner angle of the wedge.

In addition, the conductivity of wedge is another parameter affecting the relative path loss at the receiver, as in Fig. 6. Relative path loss increases with decreasing of conductivity, as shown in this figure. Although, all parameters seem to have minor effect on the relative path loss, these effects tend to be important for total relative path loss in multiple diffraction case.

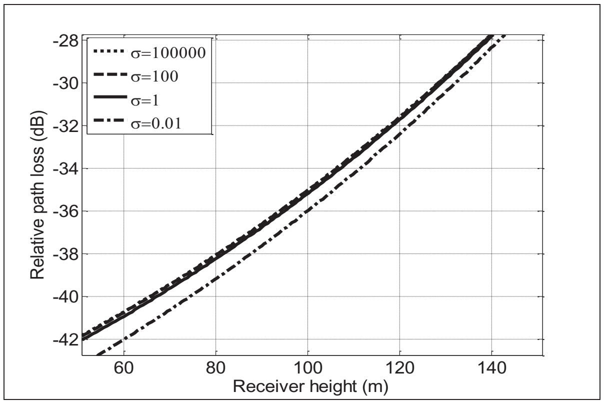

Fig. 6. Analysis of the conductivity of the wedge.

IV. CONCLUSION

In this paper, UTD based methods are reviewed. Study indicates that the Slope UTD contribution is shown in the transition zone diffraction. S-UTD has larger computation time with higher accuracy, while UTD has small computation time with lower accuracy for multiple-diffraction in transition zone. There is a tradeoff between the accuracy and the computation time, or the accuracy and the implementation complexity of methods. Moreover, an improved S-UTD method for multiple wedge diffraction is reviewed (called as S-UTD-CH). It is shown that S-UTD-CH that uses a selection algorithm of diffracting wedges based on Fresnel zone concept would be used for transition zone diffraction. S-UTD-CH provides not only very low computation time but also very accurate results for multiple transition zone diffractions, due to that after 10 diffractions S-UTD loses accuracy. Furthermore, increasing of relative permittivity constant, conductivity and inner angle of wedge, decreases the relative path loss at the receiver.

As a conclusion, S-UTD-CH model can be used for radio planning tools, due to the fact that they have relatively small computation time with high accuracy.

ACKNOWLEDGMENT

This work partially supported by Bayburt University Scientific Research Support Unit under grant 2013-1/14.

REFERENCES

[1] F. S. Adana, O. G. Blanco, I. G. Diego, J. P. Arriaga, and M. F. Cátedra, "Propagation model based on ray tracing for the design of personal communication systems in indoor environments," *IEEE Transactions on Vehicular Tech*., vol. 49, no. 6, pp. 2105-2112, 2000.

[2] F. Weinmann, "UTD shooting-and-bouncing extension to a PO/PTD ray tracing algorithm," *ACES Journal*, vol. 24, no. 3, pp. 281-293, 2009.

[3] R. G. Kouyoumjian and P. H. Pathak, "Uniform geometrical theory of diffraction for an edge in a perfectly conducting surface," *Proc. IEEE*, vol. 62, pp. 1448-1461, 1974.

[4] O. Ozgun and L. Sevgi, "Comparative study of analytical and numerical techniques in modeling electromagnetic scattering from single and double knife-edge in 2D ground wave propagation problems," *ACES Journal*, vol. 27, no. 5, pp. 376-388, 2012.

[5] K. Rizk, R. Valenzuela, D. Chizhik, and F. Gardiol, "Application of the slope diffraction method for urban microwave propagation prediction," *IEEE Vehicular Tech. Conf.*, vol. 2, pp. 1150-1155, 1998.

[6] C. Tzaras and S. R. Saunders, "An improved heuristic UTD solution for multiple-edge transition zone diffraction," *IEEE Trans. Antennas Prop.*, vol. 49, no. 12, pp. 1678-1682, 2001.

[7] L. Vogler, "An attenuation function for multiple knife-edge diffraction," *Radio Science*, vol. 17, pp. 1541-1546, 1982.

[8] A. Kara, E. Yazgan, and H. L. Bertoni, "Limit and application range of slope diffraction for wireless communication," *IEEE Trans. Antennas and Prop*., vol. 51, no. 9, 2005.

[9] M. B. Tabakcioglu and A. Kara, "Comparison of improved slope UTD method with UTD based methods and physical optic solution for multiple building diffractions," *Electromagnetics*, vol. 29, no. 4, pp. 303-320, 2009.

[10] M. B. Tabakcioglu and A. Kara, "Improvements on slope diffraction for multiple wedges," *Electromagnetics*, vol. 30, no. 3, pp. 285-296, 2010.

[11] T. K. Sarkar, "A survey of various propagation models for mobile communication," *IEEE Antennas and Propagation Magazine*, vol. 45, no. 3, pp. 51-82, 2003.

[12] H. K. Chung and H. L. Bertoni, "Application of isolated diffraction edge method for urban microwave path loss prediction," *Antennas and Propagation Symposium*, pp. 205-209, 2003.

[13] H. K. Chung and H. L. Bertoni, "Range-dependent path-loss model in residential areas for the VHF and UHF bands," *IEEE Transaction on Antennas and Propagation*, vol. 50, no. 1, pp. 1-11, 2002.

[14] J. Walfisch and H. L. Bertoni, "A theoretical model of UHF propagation in urban environments," *IEEE Transaction on Antennas and Propagation*, vol. 36, no. 12, pp. 1788-1796, 1988.

[15] H. H. Xia and H. L. Bertoni, "A theoretical model of UHF propagation in urban environments, diffraction of cylindrical and plane waves by an array of absorbing half-screens," *IEEE Transaction on Antennas and Propagation*, vol. 40, no. 2, pp. 170-177, 1992.

[16] O. M. Bucci, "The experimental validation of a technique to find the convex hull of scattering systems from field data," *IEEE Antennas and Propagation Symposium*, pp. 539-542, 2003.

[17] M. B. Tabakcioglu and A. Kara, "Discussions of various UTD and PO solutions for multiple-edge diffractions in urban radio propagation modeling," *Electromagnetic Wave Scattering Workshop*, section 11, pp. 1-6, 2008.

Mehmet Baris Tabakcioglu was born in 1981. He obtained his B.S. degree from Middle East Technical University in the department of Physics in 2005. Then he obtained his M.S. degree from Atilim University in the department of Electrical and Electronics Engineering in 2009. He then obtained his Ph.D. degree from Ataturk University in the department of Electrical and Electronics Engineering in 2013. His research area is electromagnetic wave propagation, diffraction and reflection. He is currently working at Bayburt University.

Doruk Ayberkin was born in 1981. He obtained his B.S. degree from Gazi University in the department of Physics in 2005. Then he obtained his M.S. degree from Ahmet Yesevi University in the department of Computer Engineering in 2012. His research area is electromagnetic wave propagation, diffraction and reflection and computer programming. He is currently working at Bayburt University.

Ahmet Cansiz is currently working in the Electrical Engineering Department at Istanbul Technical University, Turkey. He obtained his Ph.D. degree from the Illinois Institute of Technology, USA, in 1999. He has a wide experience in thermodynamics of the cryogenics systems regarding the superconductivity applications; superconducting levitation, superconducting bearing system and Superconducting MagLev. His research area also focuses on interdisciplinary subjects, such as heat transfer phenomena in heat exchangers and integration of renewable energy with smart grids. He has more than 30 journal publications in the subject of electromagnetics, electromechanics, thermodynamics and energy related topics.

Low Profile Dual Band-Notched Slot Antenna with Modified Ground Plane for UWB Systems

Nasser Ojaroudi [1], Noradin Ghadimi [1], and Yasser Ojaroudi [2]

[1] Young Researchers and Elite Club
Islamic Azad University, Ardabil Branch, Ardabil, Iran
noradin.ghadimi@gmail.com

[2]Young Researchers and Elite Club
Islamic Azad University, Germi Branch, Germi, Iran

Abstract **─** In this paper, a new compact microstrip-fed slot antenna with dual band-notched performance for Ultra-Wideband (UWB) communications is presented. In the proposed structure, by using an inverted U-shaped conductor-backed plane, a new resonance at 12.5 GHz is excited and hence much wider impedance bandwidth can be produced. In order to generate a single band-notched function, we use an inverted T-shaped strip protruded inside the rectangular slot, with this structure first rejection band around of 3.3-4.2 GHz can be achieved. By inserting a pair of C-shaped slots in the ground plane, dual band-notched function can be produced. The measured results reveal that the presented dual band-notched slot antenna offers a wide bandwidth from 2.62 GHz to 13.81 GHz, with two notched bands covering all the 5.2/5.8 GHz WLAN, 3.5/5.5 GHz WiMAX and 4-GHz C bands. The proposed antenna has a small size. Simulated and experimental results obtained for this antenna show that it exhibits good radiation behavior within the UWB frequency range.

Index Terms **─** C-shaped slot, dual band-notched performance, inverted U-shaped conductor-backed plane, protruded T-shaped strip and UWB slot antenna.

I. INTRODUCTION

Ultra-Wideband (UWB) systems and applications developed rapidly in recent years. It has plenty of advantages, such as simple structure, small size and low cost due to having received increased attention; especially microstrip antenna, it's extremely attractive to be used in emerging UWB applications and growing research activity is being focused on them. Consequently, a number of planar microstrip antennas with different geometries have been experimentally characterized [1-4]. The frequency range for UWB systems between 3.1 GHz to 10.6 GHz will cause interference to the existing wireless communication systems, such as, the Wireless Local Area Network (WLAN) for IEEE 802.11a operating in 5.15–5.35 GHz and 5.725–5.825 GHz bands and WiMAX (3.3-3.6 GHz and C-band 3.7-4.2 GHz); therefore, the UWB antennas with single and dual band-stop performance are required [5-9].

In the proposed structure, based on Electromagnetic Coupling Theory (ECT), by adding an inverted U-shaped conductor-backed in the substrate backside, additional coupling between the bottom edge of the radiating stub and the ground plane is introduced and the antenna impedance bandwidth is improved; which achieves a multi resonance performance. Also, single and dual band-strop properties are generated by using a T-shaped strip and a pair of C-shaped slots in the ground plane. Good VSWR and radiation pattern characteristics are obtained in the frequency band of interest.

II. MICROSTRIP ANTENNA DESIGN

The presented small slot antenna fed by a 50-Ω microstrip line is shown in Fig. 1, which is printed on an FR4 substrate of thickness of 0.8

Submitted On: December 5, 2013
Accepted On: March 21, 2014

mm, permittivity of 4.4, and loss tangent of 0.018. The basic slot antenna structure consists of a square radiating stub, a feed line and a ground plane. The proposed antenna is connected to a 50-Ω SMA connector for signal transmission. The radiating stub is connected to a feed line with the width of W_f and the length of L_f, as shown in Fig. 1. On the other side of the substrate, a conducting ground plane of width W_{sub} and length L_{gnd} is placed. The width W_f of the microstrip feed-line is fixed at 1.5 mm. The proposed antenna is connected to a 50-ohm SMA connector for signal transmission. The simulated results are obtained using the Ansoft simulation software High-Frequency Structure Simulator (HFSS) [10].

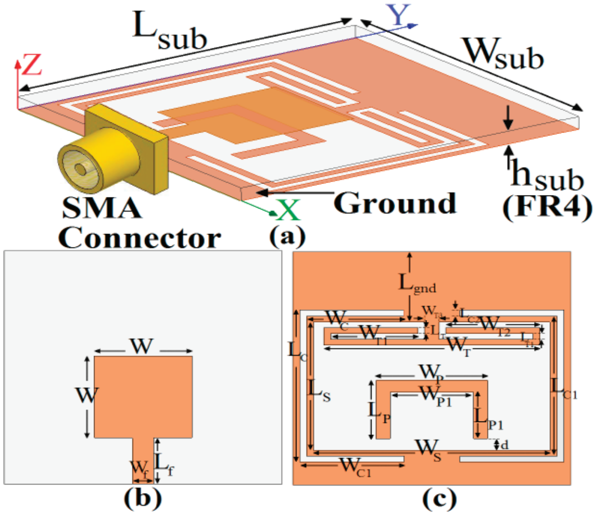

Fig. 1. Geometry of the proposed slot antenna; (a) side view, (b) top layer and (c) bottom layer.

Table 1: The final dimensions of the antenna

Param.	mm	Param.	mm	Param.	mm
W_{Sub}	20	L_{Sub}	20	W_f	1.5
L_f	4	W	7	L_{gnd}	6
W_P	8	L_P	5	W_{P1}	6
L_{P1}	4	W_T	15.5	L_T	0.5
W_{T1}	6.25	L_{T1}	0.5	W_{T2}	6.75
W_{T3}	1	L_S	11	W_S	17
L_C	13	W_C	6.5	L_{C1}	12
W_{C1}	7.5	L_{C2}	0.5	d	1

In this work, we start by choosing the aperture length L_S. We have a lot of flexibility in choosing this parameter. The length of the aperture mostly affects the antenna bandwidth. As L_S decreases, so does the antenna BW and vice versa. In the next step, we have to determine the aperture width W_S. The aperture width is approximate, whereas the slot wavelength depends on a number of parameters, such as the slot width as well as the thickness and dielectric constant of the substrate on which the slot is fabricated. Then to choose the width of the radiating patch W. This parameter is approximate, whereas the guided wavelength is the microstrip line [3]. The last and final step in the design is to choose the length of the resonator and the band-stop filter elements. In this design, the optimized length $L_{resonance}$ is set to resonate at $0.25\lambda_{resonance}$, where $L_{resonance} = 0.5\ (W_{p1}+L_{p1})$. Also the optimized length L_{notch} is set to band-stop resonate at $0.5\lambda_{notch}$, where $L_{notch1}=0.5\ (W_{T1}+W_{T2}) + L_T+L_{T1}$, and $L_{notch2}=L_{C2}+0.5\ W_{C1}+0.25\ L_C$. λ_{notch1} and λ_{notch2} corresponds to first band-notched frequency (3.9 GHz) and second band-notched frequency (5.5 GHz), respectively.

In this study, to design a novel antenna, the modified inverted U-shaped strip is placed inside rectangular slot in the ground plane. Regarding ECT, by adding a modified conductor-backed plane in the substrate backside, additional coupling is introduced between the bottom edge of the radiating stub and the ground plane and the antenna impedance bandwidth is improved without any cost of size or expense. Moreover, these structures change the inductance and capacitance of the input impedance, which in turn leads to change the bandwidth [4-6]. Therefore, by adding an inverted U-shaped parasitic structure in the ground plane, much enhanced impedance bandwidth may be achieved.

In addition, to create a desired dual frequency band-stop characteristic, a T-shaped strip with a pair of C-shaped slots are used in the ground plane. At the notched frequencies, the current flows are more dominant around the T-shaped and C-shaped structures and they are oppositely directed between the embedded structures and the radiating stub. As a result, the desired high attenuation near the notched frequency can be produced [10-12]. Final values of the presented antenna design parameters are specified in Table. 1.

III. RESULTS AND DISCUSSIONS

The presented microstrip-fed slot antenna were constructed and studied to demonstrate the effect of the proposed dual band-notched function and bandwidth enhancement technique. The simulated and experimental results of the input impedance and radiation characteristics are presented and discussed.

Figure 2 shows the structure of the various antennas used for simulation studies. VSWR characteristics for ordinary slot antenna (Fig. 2 (a)), with an inverted U-shaped conductor-backed plane in the ground plane (Fig. 2(b)), with inverted U-shaped conductor-backed plane and T-shaped strip (Fig. 2(c)) and the proposed antenna structure (Fig. 2 (d)), are compared in Fig. 3.

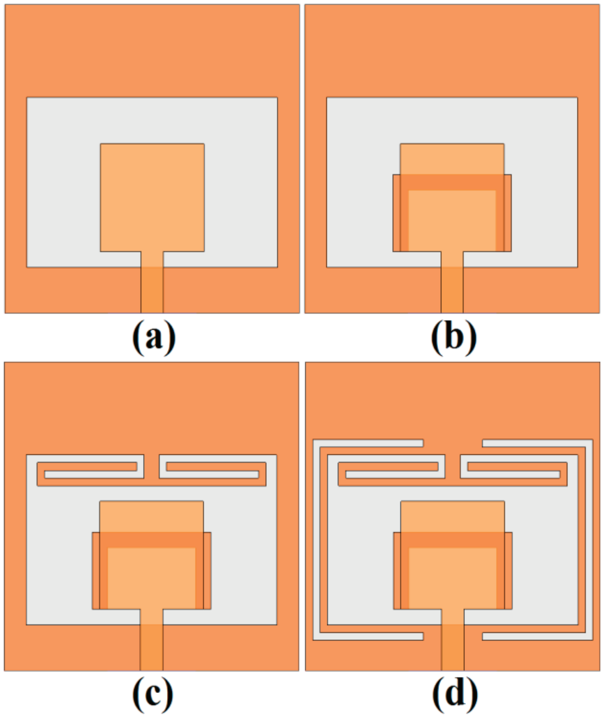

Fig. 2. (a) basic structure (ordinary slot antenna), (b) antenna with an inverted U-shaped conductor-backed plane, (c) antenna with inverted U-shaped conductor-backed plane and protruded T-shaped strip and (d) the proposed antenna.

As shown in Fig. 3, in the proposed antenna configuration, the ordinary slot antenna can provide the fundamental and next higher resonant radiation band at 4 GHz and 8 GHz, respectively. As illustrated in Fig. 3, the inverted U-shaped conductor-backed plane is playing an important role in the broadband characteristics and in determining the sensitivity of impedance matching of this antenna [4].

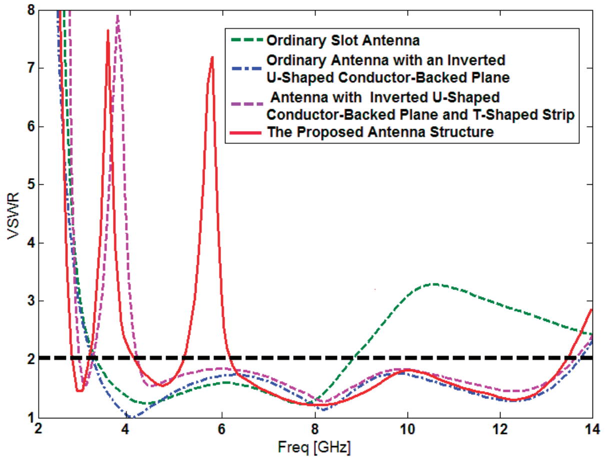

Fig. 3. Simulated VSWR characteristics for the various structures shown in Fig. 2.

It is found that by inserting the inverted U-shaped conductor-backed plane at the ground plane, additional resonance (third resonance at 12.5 GHz) is excited and hence much wider impedance bandwidth with multi resonance characteristics can be produced; especially at the higher band [11-12]. As shown in Fig. 3, in order to generate single band-notched characteristics (3.9 GHz), we use an inverted T-shaped strip protruded inside rectangular slot. By inserting a pair of C-shaped slots in the ground plane, dual band–notched function is achieved covering all the 5.2/5.8 GHz WLAN, 3.5/5.5 GHz WiMAX and 4-GHz C bands.

In order to understand the phenomenon behind this additional resonance performance, the simulated current distributions on the ground plane for the presented antenna are presented in Fig. 4. As shown in Fig. 4 (a), at the third resonance frequency, the current flows are more dominant around of the inverted U-shaped conductor-backed plane at third resonance frequency (12.5 GHz). Figure 4 (b) presents the simulated current distributions on the ground plane at the first notched frequency (3.9 GHz). As shown in Fig. 4 (b), at the first notched frequency the current flows are more dominant around of the inverted T-shaped strip. Another important design parameter of this structure is use of the pair of C-shaped slots.

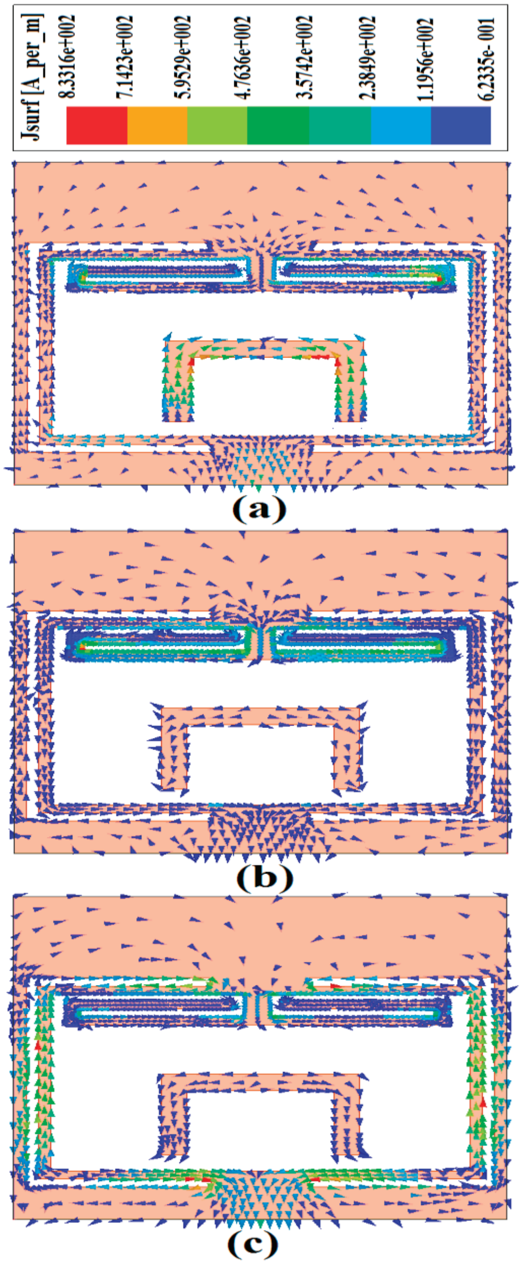

(a)

(b)

(c)

Fig. 4. Simulated current distributions for the proposed antenna on the ground plane; (a) at the new resonance frequency (12.5 GHz), (b) at first notched frequency (3.8 GHz) and (c) at second notched frequency (5.5 GHz).

Figure 4 (c) presents the simulated current distributions on the ground plane for the proposed antenna at the second notched frequency (5.5 GHz). It can be observed in Fig. 4 (c), that the current concentrated on the edges of the interior and exterior of the C-shaped slots. Therefore, the antenna impedance changes at this frequency due to the notch band properties of this slot [13].

The proposed microstrip monopole antenna with final design as shown in Fig. 5, was built and tested and the VSWR characteristic was measured using a network analyzer in an anechoic chamber. The radiation patterns have been measured inside an anechoic chamber using a double-ridged horn antenna as a reference antenna placed at a distance of 2 m. Also, a two-antenna technique using a spectrum analyzer and a double-ridged horn antenna as a reference antenna placed at a distance of 2 m, is used to measure the radiation gain in the z axis direction (x-z plane).

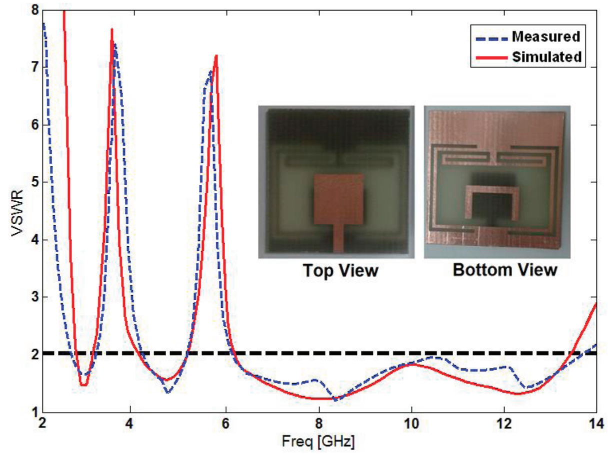

Fig. 5. Measured and simulated VSWR for the proposed antenna.

Figure 5 shows the measured and simulated VSWR characteristics of the proposed antenna. The fabricated antenna has the frequency band from 2.62 GHz to 13.81 GHz, with two rejection bands around 3.32-4.28 GHz and 5.13-6.08 GHz.

Figure 6 depicts the measured and simulated radiation patterns of the proposed antenna, including the co-polarization and cross-polarization in the H-plane (x-z plane) and E-plane (y-z plane). It can be seen that the quasi-omnidirectional radiation pattern can be observed on x-z plane over the whole UWB frequency range; especially at the low frequencies. The radiation pattern on the y-z plane displays a typical figure-of-eight, similar to that of a conventional dipole antenna. It should be noticed that the radiation patterns in E-plane become imbalanced as frequency increases, due to the increasing effects of the cross polarization. The patterns indicate at higher frequencies and more ripples can be observed in both E and H-planes, owing to the generation of higher-order modes. [14-16].

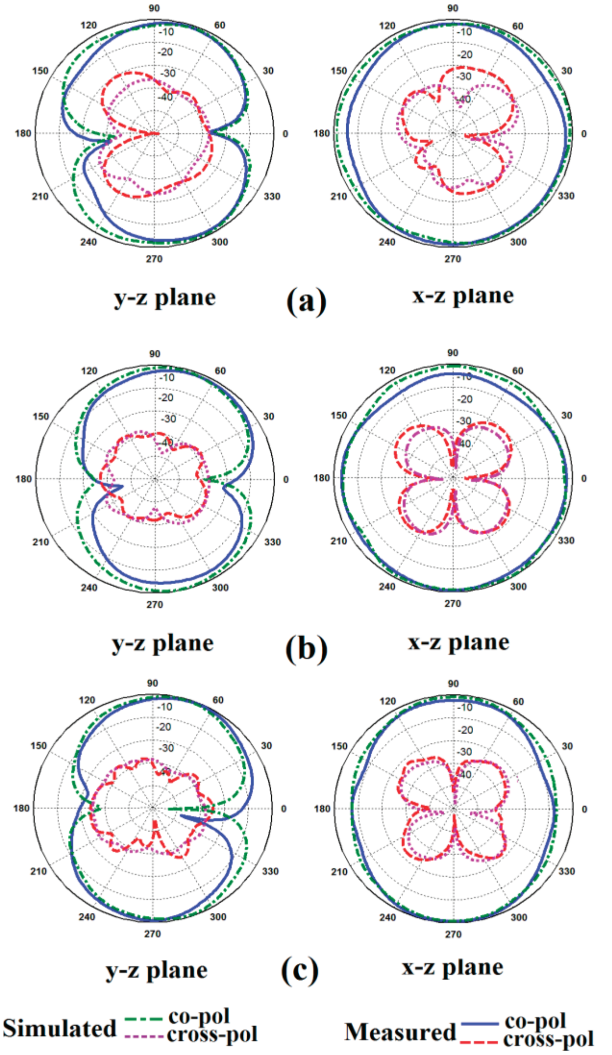

Fig. 6. Measured and simulated radiation patterns of the proposed antenna; (a) 4.5 GHz, (b) 7.5 GHz and (c) 10 GHz.

The simulated and measured input impedance characteristics of the proposed antenna are shown in Fig. 7. As seen, in the notched frequencies, the imaginary component curve shows parallel resonances and the real component presents high resistance characteristics. As a result of impedance curve of proposed antenna, it is suggested that the input impedance of the notched antenna is equivalent to the input impedance R_a of the un-notched reference ordinary antenna, connected with two parallel LC-resonant circuits in series.

Also, the conceptual circuit model of the antenna is shown in Fig. 8. When the proposed antenna is operating at the two desired notched frequencies, the two corresponding *LC* resonant circuits mentioned above will be syntonic, which leads to the input impedance to be opened. Therefore, proposed band-notched UWB antenna presents high impedance characteristics at notched frequencies.

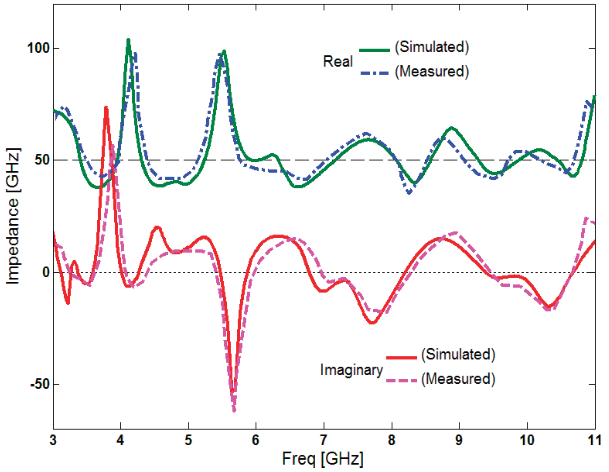

Fig. 7. Measured and simulated input impedance characteristics of the proposed antenna.

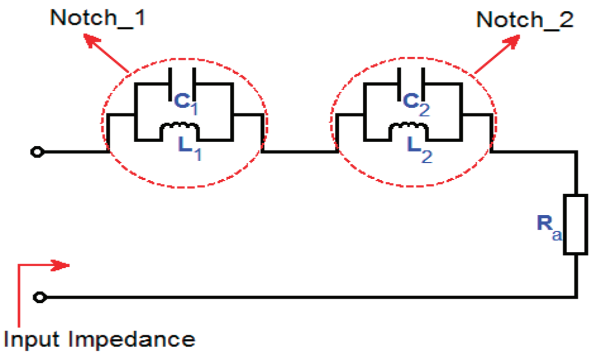

Fig. 8. Conceptual circuit model for proposed antenna.

In addition, measured and simulated input impedance characteristics of the proposed antenna on a Smith chart are shown in Fig. 9.

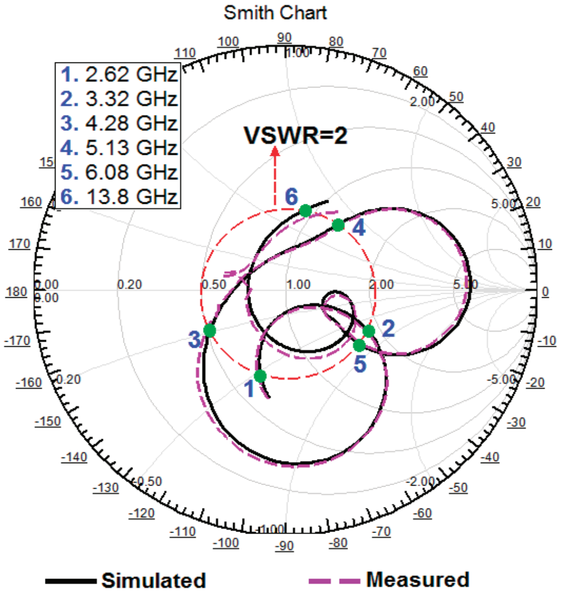

Fig. 9. Measured and simulated input impedance on a Smith chart of the proposed antenna.

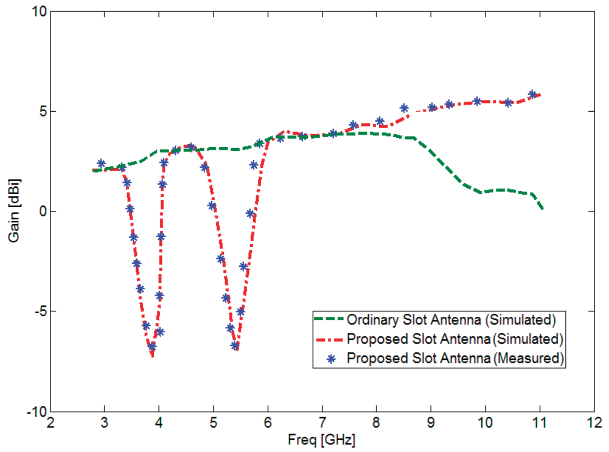

Fig. 10. Measured and simulated maximum gain for the proposed antenna in comparison with ordinary structure.

Measured maximum gain of the proposed antenna was shown in Fig. 10. As illustrated, two sharp decreases of maximum gain in the notched frequency bands at 3.9 GHz and 5.5 GHz is shown in Fig. 10. For other frequencies outside the notched frequency band, the antenna gain with the filters is improved in comparison with ordinary structure. As seen, the proposed antenna has sufficient and acceptable gain levels in the operation bands [17].

IV. CONCLUSION

In this paper, a novel planar slot antenna (PMA) with single and dual band-notched characteristics for various UWB applications has been proposed. The proposed antenna consists of a square radiating stub and a modified ground plane with an inverted U-shaped conductor-backed plane, two C-shaped sots and an inverted T-shaped strip. Fabricated antenna can operate from 2.62 GHz to 13.81 GHz with two rejection bands around 3.32-4.28 GHz and 5.12-6.07 GHz. The proposed antenna has a simple configuration and is easy to fabricate. Experimental results show that the proposed antenna could be a good candidate for UWB applications.

ACKNOWLEDGMENT

The authors are thankful to Microwave Technology (MWT) Company staff, for their beneficial and professional help (www.microwave-technology.com).

REFERENCES

[1] R. Azim, M. T. Islam and N. Misran, "Design of a planar UWB antenna with new band enhancement technique," *Applied Computational Electromagnetics Society (ACES) Journal*, vol. 26, no. 10, pp. 856-862, 2011.

[2] K. Chung, T. Yun and J. Choi, "Wideband CPW-fed monopole antenna with parasitic elements and slots," *Electronics Letters*, vol. 40, no. 17, pp. 1038-1040, 2004.

[3] J. Y. Sze and K. L. Wong, "Bandwidth enhancement of a microstrip line-fed printed wide-slot antenna," *IEEE Trans. Antennas Propag.*, vol. 49, pp. 1020-1024, 2001.

[4] Y. W. Jang, "Experimental study of large bandwidth three-offset microstrip line-fed slot antenna," *IEEE Microw. Wireless Comp. Lett.*, vol. 11, pp. 425-426, 2001.

[5] C. Y. D. Sim, W. T. Chung and C. H. Lee, "Planar UWB antenna with 5 GHz band rejection switching function at ground plane," *Progress In Electromagnetics Research*, vol. 106, pp. 321-333, 2010.

[6] N. Ojaroudi and N.Ghadimi, "UWB small slot antenna with WLAN frequency band-stop function," *Electron. Lett*, vol. 49, pp. 1317–11318, 2013.

[7] J. C. Ding, Z. L. Lin, Z. N. Ying and S. L. He, "A compact ultra-wideband slot antenna with multiplenotch frequency bands," *Microwave and*

Optical Technology Letter, vol. 49, no. 12, pp. 3056-3060, 2007.

[8] K. H. Kim and S. O. Park, "Analysis of the small band-rejected antenna with the parasitic strip for UWB," *IEEE Transactions on Antennas and Propagation*, vol. 54, no. 6, pp. 1688-1692, 2006.

[9] C. Y. Pan, K. Y. Chiu, J. H. Duan and J. Y. Jan, "Band-notched ultra-wideband planar monopole antenna using shunt open-circuited stub," *Microwave and Optical Technology Letter*, vol. 53, no. 7, pp. 1535-1537, 2011.

[10] "Ansoft High Frequency Structure Simulation (HFSS)," ver. 13, *Ansoft Corporation*, 2010.

[11] M. R. Hamid, P. S. Hall, P. Gardner and F. Ghanem, "Switched WLAN wideband tapered slot antenna," *Electronics Letters*, vol. 46, no. 1, pp. 23-24, 2010.

[12] Y. S. Li, X. D. Yang, C. Y. Liu and T. Jiang, "Analysis and investigation of a cantor set fractal UWB antenna with a notch-band characteristic," *Progress In Electromagnetics Research B*, vol. 33, pp. 99-114, 2011.

[13] A. Foudazi, H. R. Hassani and S. M. Nezhad, "Small UWB planar monopole antenna with added GPS/GSM/WLAN bands," *IEEE transactions on Antenna & Propagation*, vol. 60, no. 6, June 2012.

[14] N. Ojaroudi, "Compact UWB monopole antenna with enhanced bandwidth using rotated l-shaped slots and parasitic structures," *Microw. Opt. Technol. Lett.*, vol. 56, pp. 175-178, 2014.

[15] N. Ojaroudi, "Design of microstrip antenna for 2.4/5.8 GHz RFID applications," *German Microwave Conference, GeMic*, RWTH Aachen University, Germany, March 10-12, 2014.

[16] N. Ojaroudi, "Application of protruded strip resonators to design an UWB slot antenna with WLAN band-notched characteristic," *Progress in Electromagnetics Research C,* vol. 47, pp. 111-117, 2014.

[17] N. Ojaroudi, "Microstrip monopole antenna with dual band-stop function for UWB applications," *Microw. Opt. Technol. Lett.*, vol. 56, pp. 818-822, 2014.

Optimization-Based Matching Layer Design for Broadband Dielectric Lens Antennas

F. Tokan

Department of Electronics and Communications Engineering
Yildiz Technical University, Istanbul 34220, Turkey
ftokan@yildiz.edu.tr

Abstract ─ Dielectric lens antennas fabricated with a dense dielectric material, allow good power transfer efficiency through the lens and enable fabrication of low-cost and compact-size lens antennas. On the contrary, using dense dielectric material causes strong multiple internal reflection behavior inside the lens antenna. These multiple reflections deteriorate not only return loss but also the radiation characteristics. However, the undesirable effects of strong internal reflections can be reduced considerably using one or more dielectric Matching Layers (MLs) coated at the top of the antenna. In this paper, a novel optimization-based ML design procedure for dielectric lens antennas is proposed. In order to demonstrate effectiveness of the method, the optimization procedure is applied to two different dielectric lens antennas; a narrow band lens antenna and an Ultra-Wideband (UWB) lens antenna. The simulation results verify that MLs designed by the proposed optimization procedure prevent strong internal reflections successfully for both narrow-band and UWB applications.

Index Terms ─ Air-gap, dielectric lens antennas, matching layer, optimization, and UWB antennas.

I. INTRODUCTION

Dielectric lens antennas are widely used in millimeter-wave and sub-millimeter-wave applications, due to the fact that these antennas have high directivity, polarization purity and simple structure for fabrication [1-5]. Dielectric lens antennas are inexpensive solutions for beam steering applications with their capability of being integrated to millimeter and sub-millimeter planar feeding structures [6-7]. Mentioned characteristics make dielectric lens antennas a good candidate also for passive imaging systems and active automotive cruise control radars [8-10]. In these applications, relative permittivity of the lens material should be chosen carefully, since materials having low or high dielectric contrast with free space, have distinctive effects on the radiation characteristics of the antenna.

Low-permittivity $(\varepsilon_r < 3)$, low-loss materials are affordable solutions for dielectric lenses, which can be easily manufactured with standard tools. On the other hand, high-permittivity materials yield a more exact geometrical approximation to an elliptical lens and achieve a wider multiple-beam coverage range [11]. Typically, when the relative permittivity of the selected lens material is higher than three, considerable amounts of internal reflections occur at the dielectric-air interface [12-13]. The amount of internal reflections due to the dielectric contrast with free space, increase dramatically with the increment of dielectric contrast. For example, transmitted power ratios from dielectric-air interface are 0.96, 0.82, 0.76 and 0.54 for the materials Teflon $(\varepsilon_r = 2.25)$, Macor $(\varepsilon_r = 6)$, Alumina $(\varepsilon_r = 8.5)$ and Silicon $(\varepsilon_r = 11)$, respectively. These ratios are calculated for a flat and infinite interface, which is illuminated by a normal incident plane wave.

These internal reflections disrupt not only return loss but also the radiation characteristics of the antenna. In literature, the effects of internal reflections on radiation properties and input impedance of integrated lens antennas, are investigated in details [12-14]. If these reflections can be eliminated significantly, using high

Submitted On: August 7, 2013
Accepted On: July 14, 2014

permittivity lens material will present many benefits, such as effective power transfer through the lens and consequently low SLL and high directivity for the antenna designer.

Most common ways of reducing the internal reflections are using corrugations [15] or ML(s) made of homogeneous dielectric materials on the lens surface [16-17]. In [18], influences of dielectric matching layers on the radiation characteristics are investigated and concluded that choosing an appropriate ML improves the frequency stability of the main beam, reduces the average SLL and enhances the gain of the lens antenna.

However, when the MLs are designed using standard $\lambda_c/4$ matching rules, where λ_c is the wavelength in dielectric at the operating frequency, there are some points that are not considered:

i) Relative permittivity values of the materials calculated using standard $\lambda_c/4$ matching rules probably does not exist. Although, this is not a negation in theory, in practical applications materials having approximate relative permittivity values to calculated values has to be used and this will result in unexpected radiation characteristics.

ii) More importantly, if quarter wavelength MLs are designed, these MLs will be useful only at the corresponding operating frequency.

In this work, an optimization-based matching layer design procedure for broadband dielectric lens antennas is introduced. The lens structure and matching layers are modelled as a cascaded transmission line and maximum amount of power transfer is aimed from feed to the air. With this purpose, the relative permittivity values of the materials and the thicknesses of the MLs are optimized using Genetic Algorithms (GA). The details of the optimization process are described in section II. To demonstrate the effectiveness of the proposed design method, the method is applied to two different dielectric lens antennas from literature. The first one was designed for active or passive automotive radar applications operating at 77 GHz frequency, where the second one is a leaky-wave dielectric lens antenna operating in ultra-wide frequency band (4-12 GHz). The geometrical descriptions of both antennas are given in section III together with their feeding structure. The radiation characteristics of the lens antennas with and without MLs are demonstrated in section IV. The radiation patterns of the antennas are simulated by the CST commercial tool [19]. The key roles of using an optimization based ML design in UWB applications are also discussed.

When MLs are coated to the surface of a lens antenna, a thin parasitic air gap remains between the dielectric materials. Nevertheless, to the best of my knowledge the influence of remaining air gap between the dielectric materials has never been studied. In the fourth section, the effects of air gaps on internal reflections are also exhibited. The considerations on the results are given in the last section.

II. OPTIMIZATION METHODOLOGY

Although, using high permittivity dielectric materials for lens antennas has many advantages, it causes strong internal reflections inside the lens. These reflections have to be reduced considerably to form the expected radiation characteristics. Common way to eliminate the negative effects of internal reflections is to place one or more dielectric matching layers at the top of the antenna. Determination of the relative permittivity and physical dimensions of the coating materials is crucial to obtain expected contribution of the MLs on the radiation.

Rather than using standard $\lambda_c/4$ matching rules where MLs operate effectively only at a single frequency, in this work, a novel optimization-based ML design procedure valid for broadband applications as well is proposed. This is achieved by composing a transmission line model for dielectric lens antennas having cascaded MLs. This concept is introduced with Fig. 1. In Fig. 1 (a), an extended hemispherical lens antenna having multiple MLs is shown. In Fig. 1 (b), the corresponding transmission line model for this configuration is demonstrated.

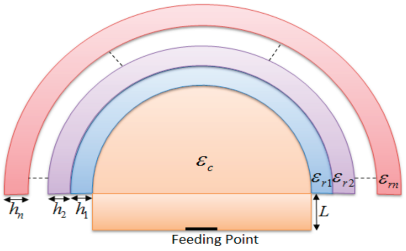

(a)

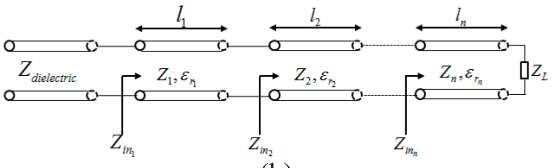

(b)

Fig. 1. The dielectric lens antenna having multiple MLs: (a) geometrical representation and (b) cascaded transmission line model.

Using the cascaded transmission line model, the general reflection coefficient from the interface of the lens antenna and MLs can be formulated as follows:

$$\Gamma = \frac{\left| Z_{in_n} - Z_{dielectric} \right|}{Z_{in_n} + Z_{dielectric}}, \text{ n=1,2,}\ldots N, \tag{1}$$

where, $Z_{dielectric} = Z_0 / \sqrt{\varepsilon_c}$. Here, N is the number of matching layers and Z_{in_n} is the input impedance of the related ML. Besides, ε_c represents the relative permittivity of the lens material, where ε_0 and μ_0 are permittivity and permeability of free space, respectively. Input impedance of each transmission line given in (1) can be formulated as follows:

$$Z_{in_n} = Z_n \frac{Z_{in_{n+1}} + jZ_n \tan \beta_n l_n}{Z_n + jZ_{in_{n+1}} \tan \beta_n l_n}, \text{ n=1,2,}\ldots N. \tag{2}$$

Here, Z_n is the characteristic impedance of the related transmission line, where, β_n and l_n are the phase constant and length of the corresponding transmission line, respectively. When equations (1) and (2) are investigated, it is clear that the design parameters which can be used to minimize the internal reflections from the interface of lens material-MLs are relative permittivity of MLs, $\varepsilon_{r_1}, \varepsilon_{r_2} .. \varepsilon_{r_n}$, (n=1,2,…N) and length of the transmission lines, $l_1, l_2 .. l_n$, (n=1,2,…N). To maximize the power transmission from lens to open air for a cascaded system as given in Fig. 1, the following fitness function is proposed:

$$Fitness = \sum_{f=f_l}^{f_h} \Gamma_f \, . \tag{3}$$

In (3), f_l and f_h are lowest and highest operating frequencies of the dielectric lens antenna, respectively. By using this fitness function, the reflection coefficient from the lens material to MLs can be minimized for both narrow and broad operating frequencies.

III. ANTENNA CONFIGURATIONS AND FEEDING DETAILS

Two extended hemispherical lens antennas are utilized to demonstrate the effectiveness of the proposed optimization procedure. The extended hemispherical lenses are most popular dielectric lens antennas, since their geometry yields a more exact geometrical approximation to an elliptical lens, resulting with a wider multiple-beam coverage range and high gain. The first antenna chosen for the implementation of optimization procedure was designed for automotive radar applications operating at 77 GHz frequency [18]. The primary source of the antenna is an aperture coupled microstrip patch printed on a RT/Duroid 5880 substrate ($\varepsilon_{r,subs} = 2.23$). The cross section view of the antenna is given in Fig. 2 (a) and the general structure of an aperture coupled microstrip patch is given in Fig. 2 (b). Here, the feed is redesigned to radiate into a dense dielectric material ($\varepsilon_c = 9$), $R_c = 6mm$ and $L = 2.34mm$ with the following dimensions: $L_{patch} = 0.6mm$ and $W_{slot} = 0.26mm$.

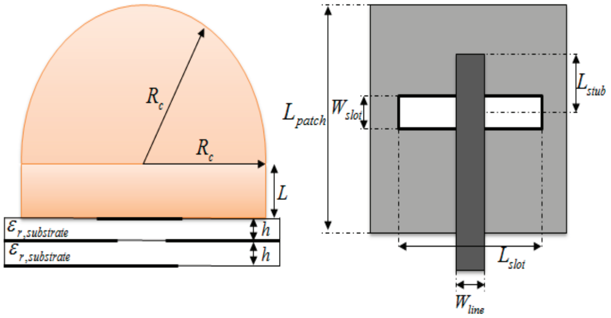

(a) (b)

Fig. 2. Geometry of the primary feed: (a) cross section view and (b) bottom view.

The second dielectric lens antenna structure selected to implement is an UWB leaky lens antenna ($R_c = 46.87mm$, $L = 14.06mm$) [20]. A dense dielectric ($\varepsilon_c = 9.8$) is chosen as the lens material to achieve high gain and high front-to-back ratio. The cross section and bottom views of the structure are given in Fig. 3 (a) and (b), respectively. The feed has been designed to operate in 4-12 GHz frequency band with the following design parameters:

$W_s = 0.5mm,\ L_s = 38mm\ , h_{gp} = 0.36\mu m,$

$h_{\mu} = 476mm, h = 937\mu m, w_{\mu} = 0.26mm, \varepsilon_{\mu,strip} = 3$.

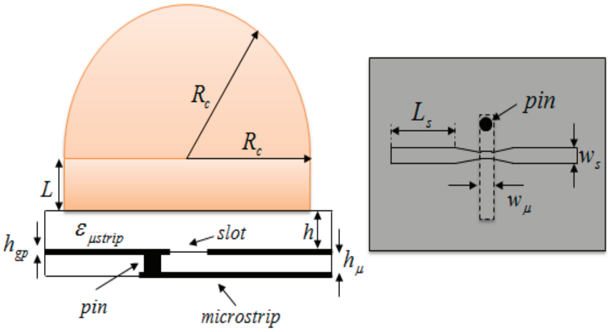

(a) (b)

Fig. 3. Geometry of the UWB lens antenna operating between 4-12 GHz: (a) cross section view and (b) bottom view.

IV. APPLICATION EXAMPLES

In this section, the optimization procedure described in section 2 is applied to the mentioned dielectric lens antennas. Dense dielectric materials $\varepsilon_{c1} = 9$ and $\varepsilon_{c2} = 9.8$ are chosen as lens core for narrow band and UWB antennas, respectively. As given before, more than 25% of the power will be reflected from the dielectric-air interface if the permittivity of the material is higher than 9 ($\varepsilon_c \geq 9$). Thus, in this section, appropriate MLs will be designed for both antennas to reduce the internal reflections significantly, to enlarge the operating frequency band and also to improve the radiation characteristics. The genetic algorithm is utilized for the optimization.

A. Narrow-band application

Although, MLs designed by $\lambda_c / 4$ matching rules will be useful for a narrow band antenna, the relative permittivity values of the materials determined will not be realistic for practical applications. Namely, if a single, double or triple MLs are aimed to be designed for a narrow band lens antenna ($\varepsilon_c = 9$) using standard $\lambda_c / 4$ matching rules, the relative permittivity and the thickness values of matching materials will be as given in Table 1.

Table 1: Relative permittivity and thicknesses of quarter wavelength MLs

Single ML	Double MLs	Triple MLs
$\varepsilon_1 = 3, h_1 = 0.59mm$	$\varepsilon_1 = 4.32, h_1 = 0.49mm$ $\varepsilon_2 = 2.08, h_2 = 0.71mm$	$\varepsilon_1 = 5.2, h_1 = 0.45mm$ $\varepsilon_2 = 3, h_2 = 0.59mm$ $\varepsilon_3 = 1.73, h_3 = 0.78mm$

These relative permittivity values correspond to some unavailable materials. For practical applications, the material with the calculated relative permittivity should be commercially available. Thus, in this work, to apply the optimization procedure, some commercial materials from Rogers Company are chosen as the ML materials. These are RO4003 ($\varepsilon_r = 3.55$) for a single layer, RT5880 ($\varepsilon_r = 2.2$) and RO3206 ($\varepsilon_r = 6.15$) for double layers and RT5880, RO4003, RO3206 for triple layers. These materials are lossy and the dissipation factors of the materials are approximately 0.002 ($\tan\delta \cong 0.002$). The thicknesses of these MLs are optimized using the given cascaded transmission line model. This is accomplished by modifying the fitness function given by (3) according to considered lens structure and then applying the definitions (1) and (2) into (3).

Optimized thickness values of each MLs are given in Table 2 together with the relative permittivity values. The optimized thickness values that minimize the internal reflections are exhibited in Table 2.

Table 2: Relative permittivity and thickness values of optimized MLs

Single ML	Double MLs	Triple MLs
$\varepsilon_1 = 3.55, h_1 = 2.59mm$	$\varepsilon_1 = 6.15, h_1 = 1.96mm$ $\varepsilon_2 = 2.2, h_2 = 0.66mm$	$\varepsilon_1 = 6.15, h_1 = 0.87mm$ $\varepsilon_2 = 3.55, h_2 = 0.28mm$ $\varepsilon_3 = 2.2, h_3 = 0.36mm$

In case of high dielectric contrast, considerable amount of power will be reflected from dielectric-air interface. This situation is demonstrated in Fig. 4. Return loss (S_{11}) is approximately around -8 dB at 77 GHz frequency. When MLs determined by optimization procedure are placed to the top of the antenna, the return loss values are suppressed to lower than -10 dB within the band of 74-80 GHz. This is also achieved by decreasing the dielectric contrast between the lens core and the outer layer; thus, consequently, minimizing the total internal reflection situations inside the lens. According to Fig. 4, adding MLs also enlarges the operating frequency band of the lens antenna.

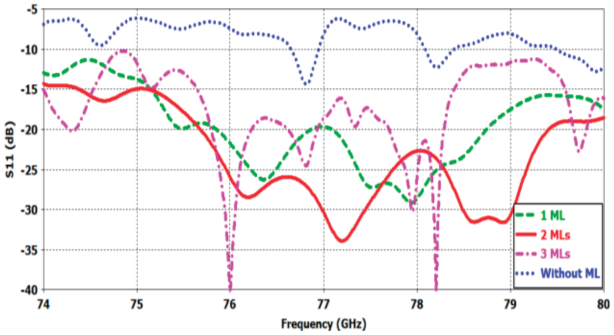

Fig. 4. Return loss variation of the narrow band lens antenna for with and without MLs cases.

The influence of the number of MLs upon the radiation characteristics of the antenna is represented in Fig. 5, in both E and H planes at 77 GHz. The co-polarization components of the antenna in E-plane are given in Fig. 5 (a), where components in H-plane are highlighted in Fig. 5 (b). For without ML case, the SLL is at least 3 dB higher than the other three cases in E-plane and Half Power Beam Width (HPBW) of the radiation pattern is quiet wider than the radiation patterns of the other cases. In Fig. 5 (b), although the SLL in two MLs case is high as without ML case, the HPBW of the pattern is considerably narrower when the antenna is coated by two MLs.

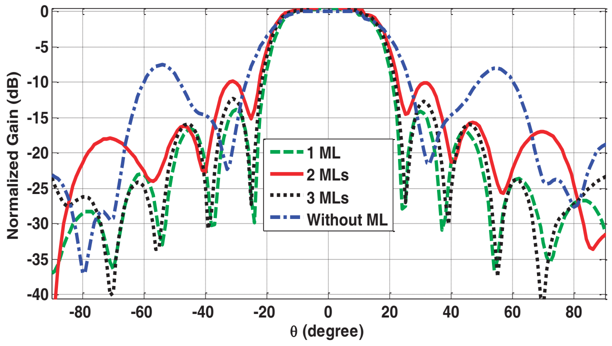

(a)

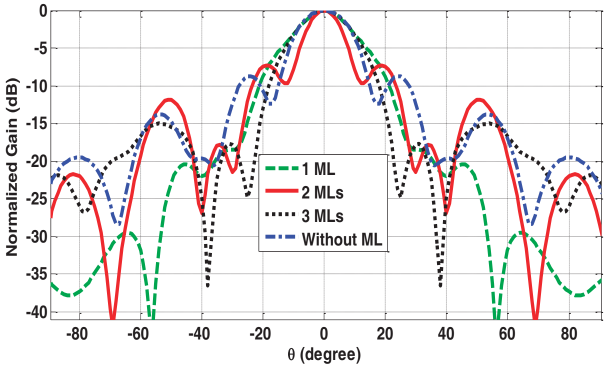

(b)

Fig. 5. Influence of MLs on the radiation patterns at 77 GHz in: (a) E-plane and (b) H-plane.

B. Ultra-wide band application

The second dielectric lens antenna type utilized to perform the proposed optimization procedure is the UWB leaky lens antenna operating between 4-12 GHz frequencies. The lens core is chosen as a high dielectric material ($\varepsilon_{c2} = 9.8$) and the same dielectric material set (RT5880, RO4003, RO3206) is utilized for MLs. When $\lambda_c/4$ matching rules are used to calculate the thickness of matching layers for a wide band antenna, λ inside the material is accepted at the center frequency. In UWB applications, the wavelengths at the lowest or highest frequencies differ significantly with the wavelength at the center frequency. Thus, MLs designed by $\lambda_c/4$ matching rules will not be applicable for UWB applications, especially for very broadband quasi-optical receivers [21].

The fitness function structure given in (3) is utilized to optimize the thickness values of each case and the results are given together with the relative permittivity values of each material in Table 3.

Table 3: Relative permittivity and thickness values of optimized MLs

Single ML	Double MLs	Triple MLs
$\varepsilon_1 = 3.55, h_1 = 3.97mm$	$\varepsilon_1 = 6.15, h_1 = 3.14mm$ $\varepsilon_2 = 2.2, h_2 = 1.53mm$	$\varepsilon_1 = 6.15, h_1 = 3mm$ $\varepsilon_2 = 3.55, h_2 = 4.11mm$ $\varepsilon_3 = 2.2, h_3 = 2.81mm$

The return loss variation of UWB feed with respect to frequency, is given in Fig. 6. When the lens core is not coated by MLs, the return loss value has some pick points higher than -8 dB between 5-6 GHz and 6-7 GHz frequencies. Although, the level of these picks is reduced by using a single ML or double MLs, the return loss is still higher than -10 dB between 5-6 GHz frequencies. When triple MLs are employed to the top of the lens core, the return loss value is reduced to lower than -10 dB levels in the operating frequency range.

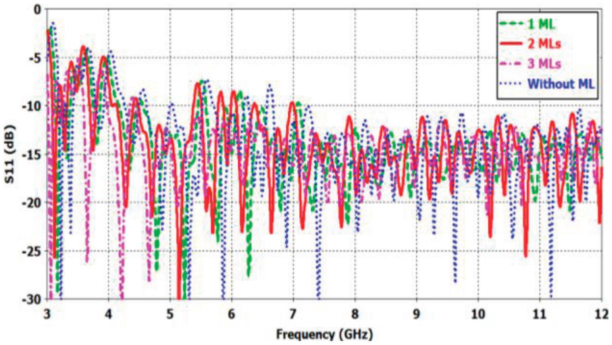

Fig. 6. The return loss variation of the UWB lens antenna for with and without MLs.

With the aim of representing the influence of the number of MLs on the radiation characteristics, far-field radiation paterns are given in both E and H-planes at the center operating frequency (8 GHz) in Fig. 7. According to Fig. 7, in both planes the HPBWs of without ML case and using three MLs case, are narrower than the other two cases. Besides, when three MLs are employed, the SLL is suppressed significantly in H-plane. As a result, covering the lens core with three MLs result in by far the best radiation characteristics among all cases for this UWB application.

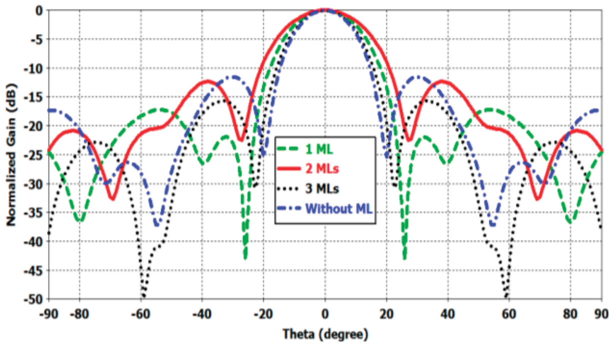

(a)

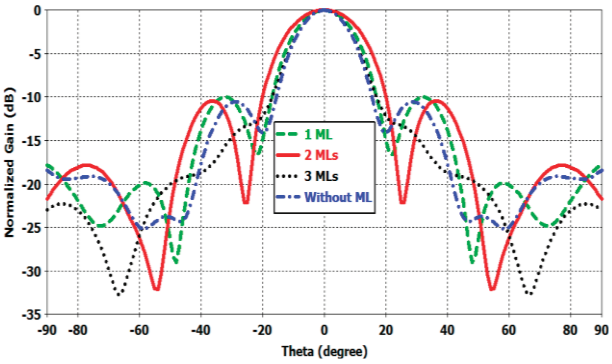

(b)

Fig. 7. Influence of MLs on the UWB dielectric lens antenna patterns at 8 GHz in: (a) E-plane and (b) H-plane.

C. Effects of air-gaps on the radiation characteristics

Adding one or more MLs made of homogeneous dielectric materials on the lens surface is a widely used technique for reducing the internal reflections inside the lens [17]. However, the parasitic air-gap that remains between dielectric materials during the fabrication process is considered as the weakness of this technique. To the best of my knowledge, the influence of parasitic air gaps between the dielectric materials on the radiation characteristics of dielectric lenses has never been studied in the perspective of UWB operation. Thus, CST simulations for UWB leaky wave antenna with three ML case are repeated by considering three different amounts of air-gaps between dielectric materials of the antenna. Three cases with 0.1, 0.2 and 0.5 mm thicknesses are considered. Although, the amounts chosen as air-gaps are quite high for today's fabrication technology, thick air-gaps are preferred to clarify all possible negative effects of air-gaps on the radiation characteristics. The return loss variation of the UWB antenna with three different thicknesses of air-gaps is given in Fig. 8. When the air-gaps between layers are chosen as 0.1 mm, the return loss of the antenna overlaps with the ideal case (no parasitic air-gap). The S_{11} variation for 0.2 mm air gaps is almost same as the S_{11} variation for 0.1 mm air-gaps case. The return loss variation is at reasonable levels for 0.5 mm thickness of air-gaps as well, except 2 dB increment at 5 GHz and 1 dB increment at 5.5 GHz frequencies.

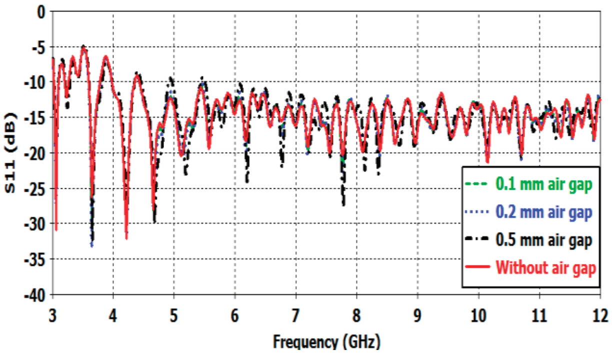

Fig. 8. The return loss variation of UWB lens antenna with three-MLs for with and without air-gaps.

The influence of air-gaps on the radiation patterns of the lens antenna having three-MLs are exhibited in both E and H-planes at 8 GHz frequency. The radiation patterns in E-plane are given in Fig. 9 (a), where H-plane are given in Fig. 9 (b).

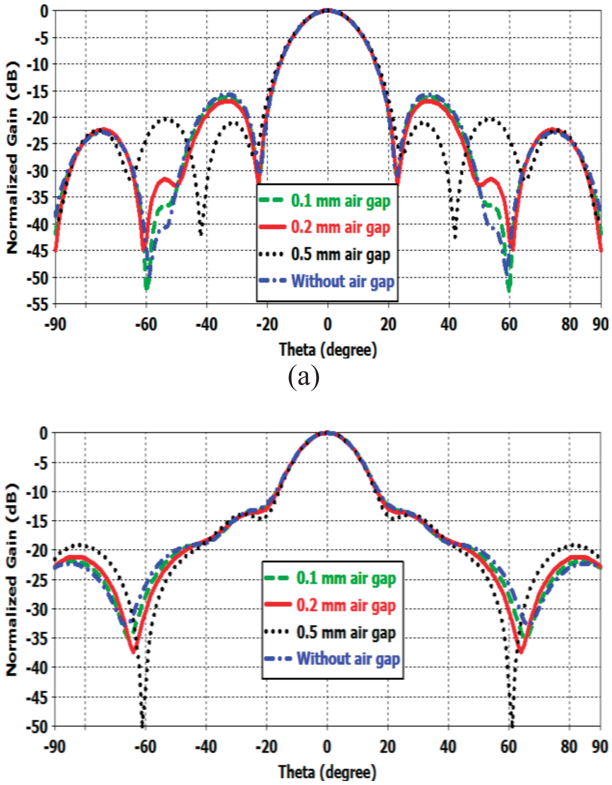

(a)

(b)

Fig. 9. Influence of air-gaps on the radiation patterns at 8 GHz frequency in: (a) E-plane and (b) H-plane.

Main and side lobes of the radiation patterns of the antenna in E-plane are not affected considerably with 0.1 mm and 0.2 mm thickness air-gaps between layers, as highlighted in Fig. 9 (a). While the HPBW of the antenna is also conserved with 0.5 mm air-gaps, only the level of second side lobe, which is still in acceptable ranges is increased about 10 dB. Similar comments can be made for the influence of 0.1 mm and 0.2 mm air gap thicknesses on the radiation characteristics in H-plane. As given in Fig. 9 (b), only the level of the outer side lobe is increased a few dB when 0.5 mm parasitic air-gaps remain between dielectric materials. It should also be added that 0.5 mm air-gap thickness is equal to $1/6$ of the lowest ML thickness (see Table 2) in the triple MLs case. For higher frequency applications, 0.5 mm air-gaps will be thick as MLs (see Table 2) and probably will have significant effects on the radiation patterns of the antenna.

V. CONCLUSION

An optimization based matching layer design procedure for broadband dielectric lens antennas is introduced. The lens structure and matching layers are modelled as a cascaded transmission line and maximum amount of power transfer is achieved from feed to the air, by considerably reducing the internal reflections from dielectric-air interface. It has been exhibited that the dielectric lens antenna coated by the MLs designed by proposed method has crucial advantages, namely:

i) For practical applications the material with the calculated relative permittivity should be commercially available. Thanks to proposed method, commercial materials can be chosen as ML materials in the optimization procedure.
ii) More importantly, when the MLs designed by the proposed method will be useful for ultra-wide band applications as well. It should be also emphasized that the radiation characteristics of the dielectric lens antenna, such as directivity, SLL and front-to-back ratio are improved with the optimized MLs in both narrow and wide frequency bands.

These MLs can be fabricated using standard computer aided manufacturing process and the extra cost due to the fabrication of the coating remains acceptable [18]. When the lens surface is coated by MLs, a thin parasitic air gap remains between the dielectric materials. The effects of parasitic air gaps on the radiation characteristics of an UWB antenna are investigated for different air-gap thicknesses. It can be concluded that return loss and radiation characteristics of the antenna are conserved even for 0.5 mm air-gaps, which is quite high for today's fabrication technology.

REFERENCES

[1] D. F. Filipovic, S. S. Gearhart, and G. M. Rebeiz, "Double-slot antennas on extended hemispherical and elliptical silicon dielectric lenses," *IEEE Transactions on Microwave Theory and Techniques*, vol. 41, no. 10, pp. 1738-1749, 1993.

[2] J. R. Costa, C. A. Fernandes, G. Godi, R. Sauleau, L. Le Coq, and H. Legay, "Compact ka-band lens antennas for LEO satellites," *IEEE Trans. Antennas Propagat*., vol. 56, no. 5, pp. 1251-1258, May 2008.

[3] D. Pasqualini and S. Maci, "High-frequency analysis of integrated dielectric lens antennas," *IEEE Trans. Antennas Propagat*., vol. 52, no. 3, pp. 840-847, 2004.

[4] S. Altunc, C. E. Baum, C. J. Buchenauer, C. G. Christodoulou, and E. Schamiloglu, "Design of a special dielectric lens for concentrating a sub-nanosecond electromagnetic pulse on a biological target," *IEEE Transactions on Dielectrics and Electrical Insulation*, vol. 16, no. 5, pp. 1364-1375, 2009.

[5] A. Mirkamali, J. Laurin, F. Siaka, and R. Deban, "A planar lens antenna with circular edge inspired by Gaussian optics," *IEEE Trans. Antennas Propag*., vol. 61, no. 9, pp. 4476-4483, September 2013.

[6] A. Karttunen, J. Saily, A. E. Lamminen, J. Ala-Laurinaho, R. Sauleau, and A. V. Raisanen, "Using optimized eccentricity rexolite lens for electrical beam steering with integrated aperture coupled patch array," *Progress In Electromagnetics Research B*, vol. 44, pp. 345-365, 2012.

[7] D. F. Filipovic, G. P. Gauthier, S. Raman, and G. M. Rebeiz, "Off-axis properties of silicon and quartz dielectric lens antennas," *IEEE Trans. Antennas Propag*., vol. 45, no. 5, pp. 760-766, May 1997.

[8] F. Sun and S. He, "Can maxwell's fish eye lens really give perfect imaging?," *Progress In Electromagnetics Research*, vol. 108, pp. 307-322, 2010.

[9] B. Schoenlinner, X. Wu, J. P. Ebling, G. V. Eleftheriades, and G. M. Rebeiz, "Wide-scan spherical-lens antennas for automotive radars," *IEEE Trans. Microwave Theory Tech*., vol. 50, no. 9, pp. 2166-2175, September 2002.

[10] M. Ettorre, R. Sauleau, L. Le Coq, and F. Bodereau, "Single-folded leaky-wave antennas for automotive radars at 77 GHz," *IEEE Antennas and Wireless Propagation Letters*, vol. 9, pp. 859-862, 2010.

[11] L. Yang, C. W. Domier, and N. C. Luhmann, "Q-band to v-band 1D and 2D elliptical lens antenna arrays," *Microwave and Optical Technology Letters*, vol. 49, no. 8, pp. 1798-1801, August 2007.

[12] M. J. M. van der Vorst, P. J. I. de Maagt, and M. H. Herben, "Effect of internal reflections on the radiation properties and input admittance of integrated lens antennas," *IEEE Trans. Microw. Theory Tech*., vol. 47, pp. 1696-1704, September 1999.

[13] M. J .M. van der Vorst, P. J. I. de Maagt, A. Neto, A. L. Reynolds, R. M. Heeres, W. Luingue, and M. H. Herben, "Effect of internal reflections on the radiation properties and input impedance of integrated lens antennas–comparison between theory and measurements," *IEEE Trans. Microw. Theory Tech*., vol. 49, pp. 1118-1125, June 2001.

[14] A. Neto, S. Maci, and P. J. I. de Maagt, "Reflections inside an elliptical dielectric lens antenna," *IEEE Proceedings on Microwaves, Antennas and Propagation*, vol. 145, no. 3, pp. 243-247, 1998.

[15] Y. Yamada, "Roles of matching layers for a shaped beam lens horn antenna," *In Proc. IEEE AP-S Int. Symp.*, Monterey, California, US, June 2004.

[16] A. Neto, S. Monni, and F. Nennie, "UWB, non-dispersive radiation from the planarly fed leaky lens antenna-part II: demonstrators and measurements," *IEEE Transactions of Antennas and Propagation*, vol. 58, no. 7, pp. 2248-2258, July 2010.

[17] J. M. Edwards, R. O'Brient, A. T. Lee, and G. M. Rebeiz, "Dual-polarized sinuous antennas on extended hemispherical silicon lenses," *IEEE Trans. Antennas Propag.*, vol. 60, no. 9, pp. 4082-4091, September 2012.

[18] N. T. Nguyen, R. Sauleau, and C. J. M. Pérez, "Very broadband extended hemispherical lenses: role of matching layers for bandwidth enlargement," *IEEE Transactions of Antennas and Propagation*, vol. 57, no. 7, pp. 1907-1913, July 2009.

[19] The homepage of CST Microwave Studio http://www.cst.com/.

[20] A. Neto, "UWB, non-dispersive radiation from the planarly fed leaky lens antenna-part I: theory and design," *IEEE Transactions of Antennas and*

Propagation, vol. 58, no. 7, pp. 2238-2247, July 2010.

[21] M. C. Gaidis, H. G. LeDuc, M. Bin, D. Miller, J. A. Stern, and J. Zmuidzinas, "Characterization of low-noise quasi-optical IS mixers for the sub-millimeter band," *IEEE Trans. Microw. Theory Tech.*, vol. 44, pp. 1130-1139, July 1996.

Fikret Tokan received his Ph.D. degree from Yildiz Technical University, Istanbul, in Comm. Engineering in 2010. From October 2011 to October 2012, he was Postdoctoral Researcher in the EEMCS Department of Delft University of Technology. From October 2012 to May 2013, he was a Postdoctoral Fellow at the Institute of Electronics and Telecomm. (IETR), University of Rennes 1, France. He has been currently working as a Researcher in the Electronics and Communications Engineering Department of YTU, Istanbul. His current research interests are UWB antenna design, dielectric lens antennas, electromagnetic waves, propagation, antenna arrays, scattering and numerical methods.

A Novel Compact Printed Slot Antenna with Triple Bands for WiMAX/WLAN Applications Using Remodeling Technology

Li Li [1,2], Zhou Zhi-Li [3], Li Ming-Fu [1], Jin Chang-Jiang [1], and Bin-Tang [1,2]

[1] Department of Electronic Engineering
[2] The Innovation Base of School-Enterprise Cooperation Aviation Electronic Technology
Chengdu Aeronautic Vocational and Technical College, Chengdu 610100, China
liliangirl@126.com

[3] Southwest Electronics Equipment Institute
China Electronics Technology Group Corporation, Chengdu 610036, China
zhouzhili003@163.com

Abstract **─** A novel compact triple-band Printed Slot Antenna (PSA) fed by CPW is presented in this paper. By attaching a crescent-shaped strip to the extremity of the CPW fed-line of a conventional CPW-fed circle slot antenna, a lower resonant mode is excited. Then, with an annular strip located between the circle slot and the crescent-shaped strip, an additional resonant mode and better impedance matching is achieved. Besides, a rectangular shorting stub is loaded at the appropriate position of the annular strip to obtain more resonant modes. By adopting such remodeling technology, the aperture utilization efficiency is greatly improved, and thus, multi-functional integration in a compact size can be realized. The designed PSA, featuring of a small size of 23×30 mm, operates over the frequency ranges 2.33-2.7 GHz, 3.3-3.8 GHz and 4.83-6.26 GHz, with good omni-directional radiation patterns and rather stable antenna gains, is suitable for both WLAN and WiMAX applications.

Index Terms **─** Compact, PSA, remodeling technology, triple-band and WLAN/WiMAX applications.

I. INTRODUCTION

With the rapid development of personal portable wireless communications, the demand for the design of an antenna with triple or multiband operation has increased; since such an antenna is vital for integrating more than one communication standards in a single compact system [1-10]. However, there are many challenges in designing a multiband antenna and the main one is how to create multi-resonating paths in a limited antenna aperture. Therefore, many efforts have been made and many multiband techniques are emerged. Generally, cutting slots on the metal radiator of antenna and loading parasitic strips are the two most typically used methods to create multi-resonating paths [11-13]. Certainly, multi-band characteristics are obtained in those works above. Nevertheless, all of them are suffering lower aperture utilization efficiency since each resonant mode requires for an unshareable slot or strip.

In addition, the PSA in merit of wider bandwidth, superior impedance matching, lower radiation loss and lower dispersion compared with the normal microstrip patch antenna, has become a rather promising candidate for kinds of multi-band applications. Particularly, the CPW-fed PSA even exhibits simpler structure and easier integration with active devices and MMIC devices [14-15].

In this paper, a novel compact CPW-fed PSA with triple bands using remodeling technology is presented. For a conventional CPW-fed circle slot antenna, there is only a single fundamental mode near 7 GHz. By attaching a crescent-shaped strip to the extremity of the CPW fed-line and adding an annular strip in the circle slot, two resonating paths (3.45/5.15 GHz) are created. Furthermore, two extra resonant modes (2.46/5.8 GHz) are obtained by simply loading a rectangular shorting

Submitted On: February 22, 2014
Accepted On: July 14, 2014

stub at the appropriate position of the annular strip. Accordingly, the size of the PSA is significantly reduced and the aperture utilization efficiency is greatly improved. Details of this antenna are presented and the measured results are given to demonstrate its performances.

II. ANTENNA DESIGN

Figure 1 shows the geometry of the proposed triple bands PSA, which is fabricated on a FR4 substrate of thickness 1.6 mm and permittivity 4.5. The proposed antenna is based on a simple circle slot antenna excited by a 50-Ω CPW fed-line with width w_f=3 mm. By connecting a crescent-shaped strip to the end of the CPW fed-line, the fundamental mode was shifted to a lower band. In order to create anther resonating paths, an annular strip is located between the circle slot and the crescent-shaped strip. Moreover, the rectangular shorting stub at the right side of the annular strip is designed to excite more resonant modes (2.46 GHz, particularly) and achieve better impedance matching across the operating frequency bands, as well as impedance bandwidth. Introducing such remodeling technology, which is an effective way to control the current resonant paths and short the resonant length of need, contributes to a smaller antenna size compared with the traditional one. The optimal antenna dimensions are as follows: L=30 mm, W=23 mm, w_1=3.6 mm, d=5.0 mm, r1=10.8 mm, r2=9 mm, r3=8.6 mm, r4=6 mm, r5=6 mm.

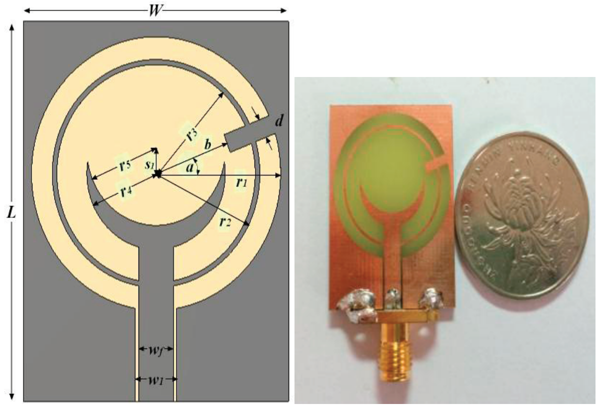

Fig. 1. Geometry of the proposed triple-band PSA.

III. RESULATS AND DISCUSSION

In order to investigate the operation mechanism of the proposed antenna, crescent-shaped strip, annular strip and rectangular shorting stub are successively employed to a conventional CPW-fed circle slot antenna (antenna *a*), while preserving the same parameters and named antenna *b*, *c* and *d*, correspondingly. The simulated reflection coefficients of these antennas are shown in Fig. 2. Obliviously, the single fundamental mode of antenna *a* is decreased from 7 GHz to 3.1 GHz when it comes to the antenna b, since the equivalent electric length is greatly lengthened by the crescent-shaped strip. An extra resonant frequency at 5.1 GHz is observed for antenna *c* because of the annular strip introduced. Moreover, it can be seen that the original operating band of antenna *b* centered at 3.1 GHz is shifted to the exactly 3.5 GHz WiMAX band, while bettering the impedance matching across the band. With the help of the rectangular shorting stub, the antenna *d* even exhibits two more resonant modes at 2.46 GHz and 5.8 GHz, compared with antenna *c*. Specially, among these resonances the highest two resonant modes (5.15 GHz/5.8 GHz) are close enough to fuse together, and thus, result in a very wide impedance bandwidth (4.83-6.16 GHz, 24.2%).

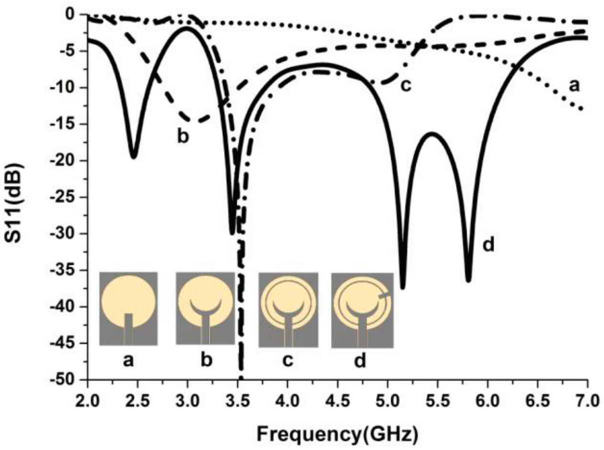

Fig. 2. The S11 curves for relevant antennas.

From the above, we can find that the rectangular shorting stub has played a rather important role in designing the proposed triple-band antenna; thus, further study is carried out base on the current distribution. For the case of the optimal design without the rectangular shorting stub, the current distributes along almost the whole annular slot corresponding to 1.5 wavelengths of the 5.1 GHz, as shown in Fig. 3 (a); which is bad to the miniaturization of antenna. Considering the fact that the design with shorting pin can reduce the antenna size effectively, the rectangular shorting stub is loaded at the right (or left) side of the annular strip, where the strongest current distribution exists and shorted to the ground plane. As a result, the original resonance path is divided into two and the left one is shorted by 1/3, while resonating at the same frequency, as shown in Fig. 3 (b). Moreover, in Fig. 4 (a), we can find that the right one also excites another half wavelength resonance at 5.8 GHz. In addition, it is worthy to see from Fig. 4 (b), that not only one wavelength resonance of 5.15 GHz is generated, but also the 1/2 wavelength resonance at 2.46 GHz is obtained by the left part of the annular slot. Accordingly, by adopting such remodeling technology, the aperture utilization efficiency is greatly improved, and thus, the overall antenna size is miniaturized. In Fig. 4 (c), current is mainly concentrated along the bottom edge of the crescent-shaped strip and the inner side of the annular strip, the total resonance length of the created path is 1/2 wavelength; which means the second working band is mostly determined by the two parts mentioned above.

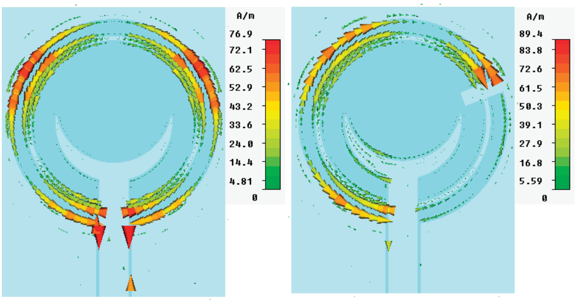

(a) At 5.1 GHz (b) At 5.15 GHz

Fig. 3. The current distribution without and with the rectangular shorting stub: (a) at 5.1 GHz and (b) at 5.15 GHz.

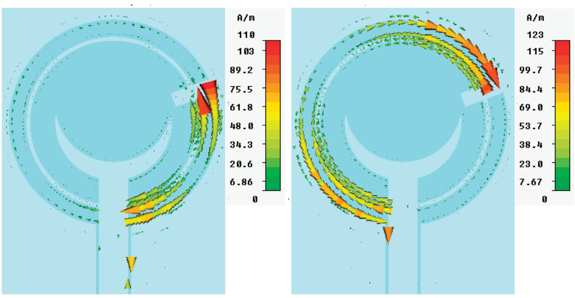

(a) At 5.8 GHz (b) At 2.46 GHz

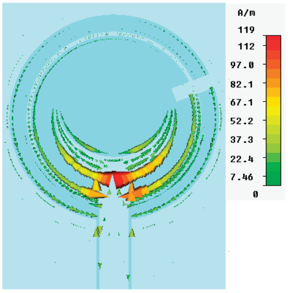

(c) At 3.45 GHz

Fig. 4. The current distribution at different frequencies: (a) at 5.8 GHz, (b) at 2.46 GHz and (c) at 3.45 GHz.

From the analysis of the current distribution at each resonant frequency, the parameter sweep is adopted to further investigate the influences of the relevant geometry to the corresponding resonant frequency bands.

Figure 5 demonstrates the effects of the rectangular shorting stub to the impedance matching condition. With the angle a (the angle between the center axis of the stub and the positive direction of the x-axis) increasing from 15 degrees, 21 degrees to 25 degrees gradually, the current path of the left (right) annular slot is shorted (lengthened); which results in the first and third resonant frequency shift right, while the fourth one shift left. At the same time, the second band almost stands still.

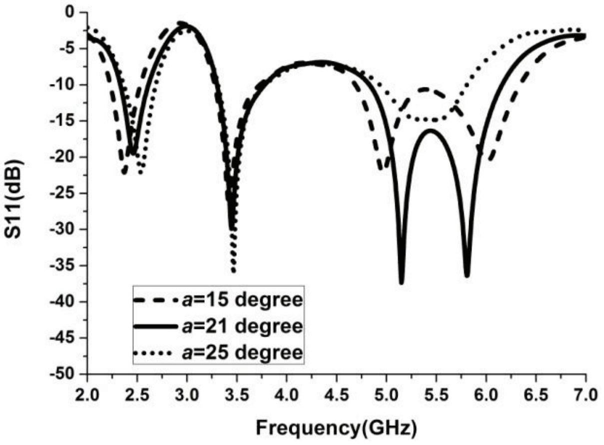

Fig. 5. Simulated S11 for various angle *a*.

Moreover, the -10 dB reflection coefficient for various outer radius of the annular strip r_2 are also plotted in Fig. 6. It can be noted that the parameter

r_2 has great impact on the first and third working bands. With r_2 decreasing from 9.2 mm to 8.8 mm, the centre frequency of the first operating band varies from 2.34 GHz to 2.6 GHz, correspondingly; since the related resonant current path is shorted. Similarly, the third operating band shifts right. Particularly, the electromagnetic coupling effect between the annular slots is sensitive to the width of the annular slot. The wider of the width, the weaker the coupling strength is, which results in the worse impedance matching. However, the annular slot width should not be too narrow, since the over coupling will deteriorate the performances of the working band as well. Finally, the optimized value for r_2 is chosen to be 9 mm considering the fabrication accuracy.

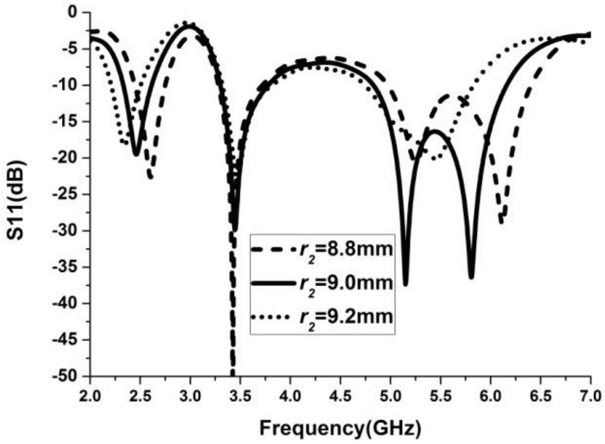

Fig. 6. Simulated S11 for various length r_2.

Figure 7 shows the reflection coefficient for different values of r4. It can be found that the second resonant mode shifts from around 3.45 GHz to 3.24 GHz, corresponding to the outer radius r4 of the crescent-shaped strip from 6 to 6.2 mm. That is due to the fact that the resonant length of the second resonant mode is lengthened with the r4 increasing gradually. Similarly, with *b* increasing from 5.9 mm to 6.1 mm, the second operating band shifts left as well, shown in Fig. 8.

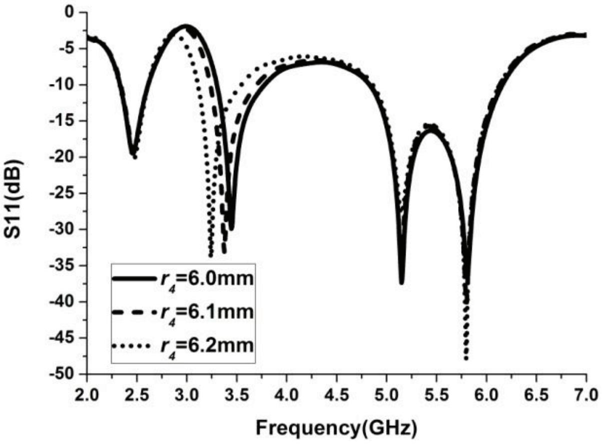

Fig. 7. Simulated S11 for different values of r4.

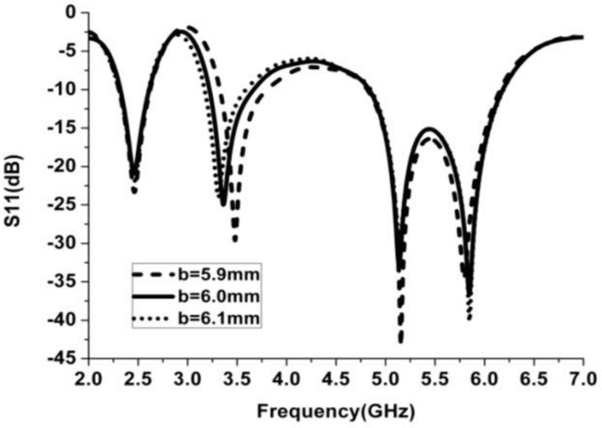

Fig. 8. Simulated S11 for different values of b.

The simulated and measured S11 of the proposed triple-band PSA is shown in Fig. 9; the results of the simulation reveals excellent agreement with that of the measurement. It can be observed that the designed antenna has triple operating bands covering the frequency ranges 2.33-2.7 GHz, 3.3-3.8 GHz and 4.83-6.26 GHz, corresponding to an impedance bandwidth of 14.7%, 14.1% and 25.8%, with respect to the appropriate resonant frequency, respectively. Apparently, the above obtained bandwidths with good impedance characteristic can simultaneously cover both the 2.4/5.2/5.8 GHz WLAN and 2.6/3.5/5.5 GHz WiMAX bands.

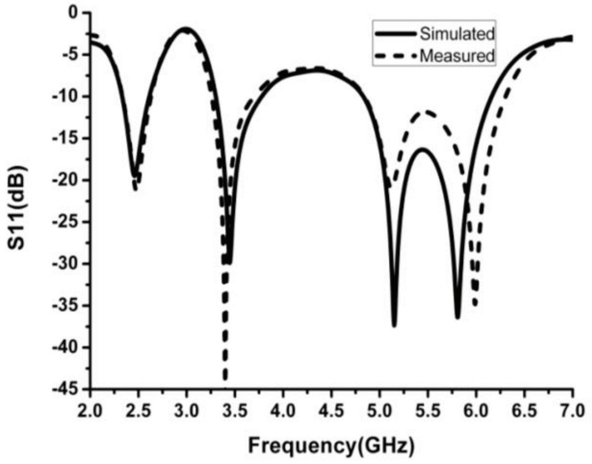

Fig. 9. The measured and simulated S11 of the proposed antenna.

Figure 10 (a) and (b) show the E-plane and H-plane radiation patterns of the proposed antenna at 2.46 GHz, 3.45 GHz and 5.15 GHz, respectively. It can be seen that the proposed antenna exhibits a fairly good omni-directional radiation pattern in the H-plane and a dipole-like radiation pattern in the E-plane. In the lower band (2.46 GHz), the resonant mode is excited by adding the rectangular shorting stub to force the current to mainly distribute along the left part of the annular slot, but considerable current is also excited in the right part of the annular slot. So a more distorted H-plane pattern is observed, compared with the higher bands.

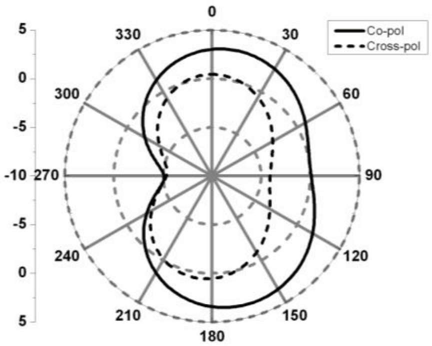

2.46 GHz

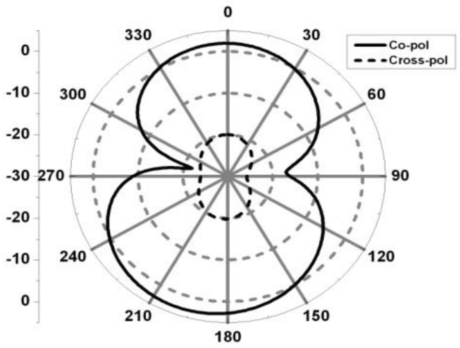

3.45 GHz

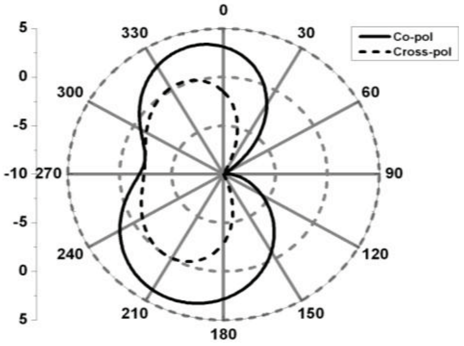

5.15 GHz

(a) E-plane

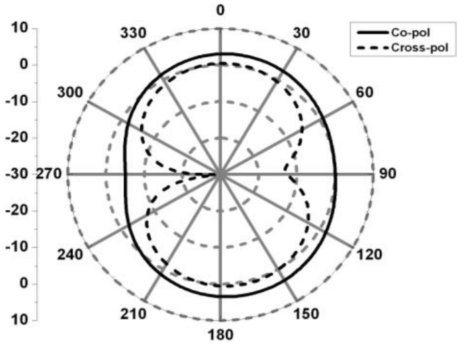

2.46 GHz

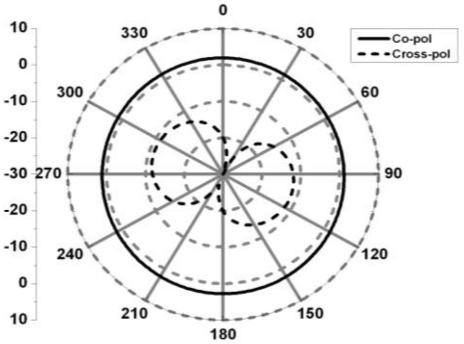

3.45 GHz

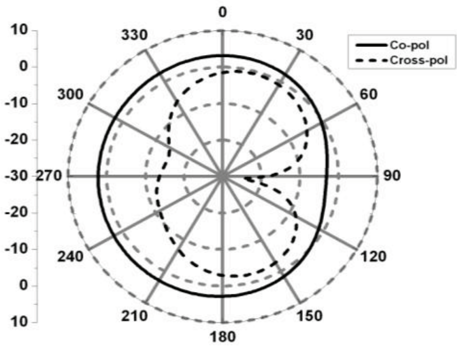

5.15GHz
(b) H-plane

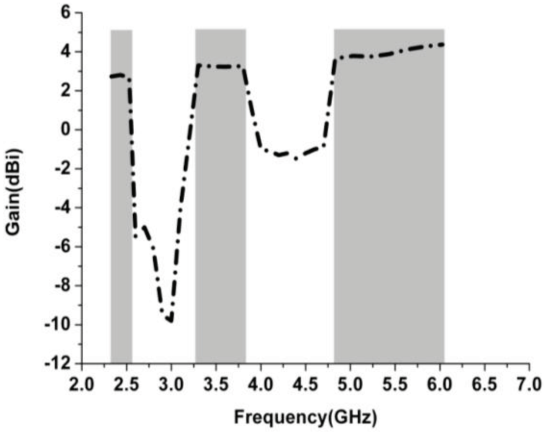

(c) Antenna gains

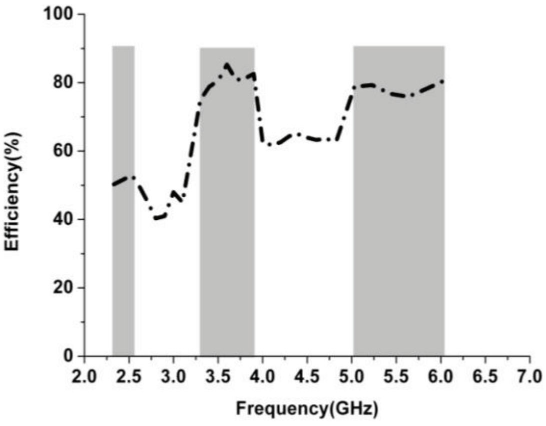

(d) Antenna efficiency

Fig. 10. The radiation patterns and antenna gains of the proposed antenna: (a) E-plane, (b) H-plane, (c) antenna gains and (d) antenna efficiency.

The average antenna gains are about 3.75 dBi, 3.28 dBi and 4 dBi for the triple operating bands, respectively. Particularly, the gains across the entire operating bands keep rather stable, which is critical to designing a well performed personal portable wireless communication system, as shown in Fig. 10 (c). Besides, the antenna efficiency is also discussed in Fig. 10 (d). It can be seen that the antenna efficiency is around 80% in the higher two operation bands. In the lower band, the antenna efficiency is decreased to about 53%, since the antenna size is rather compact for 2.4 GHz band. Finally, a comparison in size and performance with the previous reported designs is also presented, to give a better view of the proposed antenna, shown in Table 1.

Table 1: Antenna performance comparisons

Size (mm)	Bandwidth GHz	Max Gain (dBi)	Antenna
30*23	2.33-2.7, 3.3-3.8, 4.83-6.26	4.36	This paper
48*35	1.77-2.5, 4.87-6.14	4	Reference [11]
50*35	0.86-0.98, 1.7-2.5, 4.72-6.61	3.74	Reference [13]

IV. CONCLUSION

A novel compact CPW-fed PSA for a triple-frequency operation has been presented. The crescent-shaped strip, annular strip and rectangular shorting stub introduced successfully created the multi-resonating paths in a simple circle slot antenna. With the use of remodeling technology, compact antenna size, higher aperture utilization efficiency and the wider impedance bandwidth are achieved. Furthermore, well covering all the WLAN and WiMAX operating bands, the proposed triple bands antenna also shows quite suitable radiation performances and stable antenna gains, which make it a very good candidate for various kinds of personal portable wireless communications applications.

ACKNOWLEDGEMENT

This project was granted financial support from China Postdoctoral Science Foundation, under Grant No. 2012M511919. This work was supported in part by Scientific Research Fund of the Sichuan Provincial Education Department.

REFERENCES

[1] S. Chaimool and K. L. Chung, "CPW-fed mirrored-l-monopole antenna with distinct triple bands for WiFi and WiMAX applications," *Electron. Lett*., 45 (18), pp. 928-929, 2009.

[2] A. Foudazi, H. R. Hassani, and S. M. A. Nezhad, "Small UWB planar monopole antenna with added GPS/GSM/WLAN bands," *IEEE Trans. Antennas Propag*., 60 (6), pp. 2987-2992, 2012.

[3] R. K. Gupta, "Printed tri-band monopole antenna structures for wireless applications," *Microw. Opt. Technol. Lett*., 51 (7), pp. 1781-1785, 2009.

[4] P. Nepa, G. Manara, A. A. Serra, and G. Nenna, "Multiband PIFA for WLAN mobile terminals," *IEEE Antennas Wirel. Propag. Lett*., 4 (105), pp. 349-350, 2005.

[5] Y. C Lee and J. S Sun, "Compact printed slot antennas for wireless dual and multi-band operations," *Progress In Electromagnetics Research*, 88, 289-305, 2008.

[6] A. Foudazi, A. Mallahzadeh, etc., "A triple-band WLAN/WiMAX printed monopole antenna for MIMO applications," *Microwave and Optical Technology Letters*, volume 54, issue 5, pages 1321-1325, May 2012.

[7] Z. Yang, S. Xin, etc., "Design of a CPW-fed compact slot antenna for WIMAX/WLAN applications," *2011 International Conference on Computational Problem-Solving (ICCP)*, 2011.

[8] M. Jahanbakht, A. A. L. Neyestanak, etc., "Band notching ultra wideband microstrip antenna with an augmented crescent cut," *Eu CAP 2009*, 2009.

[9] O. M. Haraz, A. Elboushi, etc., "Band rejection capabilities of UWB elliptical slot antenna with half circular and crescent ring shaped radiators," *APSURSI 2010*, 2010.

[10] A. Mallahzadeh, etc., "A small-size pentaband hand-shaped coplanar waveguide-fed monopole antenna," *Microwave and Optical Technology Letters*, volume 53, issue 7, pages 1576-1579, July 2011.

[11] W. C. Liu, M. Ghavami, and W. C. Chung, "Triple-frequency meandered monopole antenna with shorted parasitic strips for wireless application," *IET Microw. Antennas Propagate*., 3 (7), pp. 1110-1117, 2009.

[12] P. Xu, Z. H. Yan, and C. Wang, "Multi-band modified fork-shaped monopole antenna with dual l-shaped parasitic plane," *Electron. Lett*., 47 (6), pp. 1051-1052, 2011.

[13] K. Seol, J. Jung, and J. Choi, "Multi-band monopole antenna with inverted u-shaped parasitic plane," *Electron. Lett*, 42 (15), pp. 844-845, 2006.

[14] J. S. Chen, "Dual-frequency annular-ring slot antennas fed by CPW feed and microstrip line feed," *IEEE Trans. Antennas Propag*., vol. 53, no. 1, pp. 569-573, January 2005.

[15] A. U. Bhobe, C. L. Holloway, M. Piket-May, and R. Hall, "Wide-band slot antennas with CPW feed lines: hybrid and log-periodic designs," *IEEE Trans. Antennas Propag*., vol. 52, no. 10, pp. 2545-2554, October 2004.

Li Li was born in Meishan, China. She received her B.S. degree in Electronics Information and Engineering from Leshan Normal University, China, in 2009 and the M.S. degrees in Radio Physics from the University of Electronic Science and Technology of China (UESTC), in 2012. She is now a Teacher at CAVTC. Her research interest includes ultra-wideband antenna, multi-band antenna and the miniaturization technology.

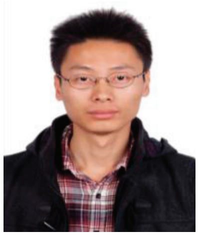

Zhou Zhi-Li was born in Chongqing, China. He received his B.S. degree in Electronics Information and Engineering from Sichuan University, China, in 2009 and the M.S. degree in Radio Physics from the University of Electronic Science and Technology of China (UESTC), in 2012. He is now an Antenna Engineer at CETC29 and his research interests include ultra-wideband antennas, phased array antenna, conformal antennas, Radar Cross-Section and micro systems.